

DEVELOPMENT OF A WATER-COOLED LDV PROBE
FOR ROCKET/GAS-TURBINE ENGINE
ENVIRONMENTS

by

JASON ALLEN DAVIS

DR. SEMIH M. ÖLÇMEN, COMMITTEE CHAIR
DR. MUHAMMAD ALI ROB SHARIF
DR. MARCUS ASHFORD

A THESIS

Submitted in partial fulfillment of the requirements
for the degree of Master of Science in the
Department of Aerospace Engineering and Mechanics
in the Graduate School of
The University of Alabama

TUSCALOOSA, ALABAMA

2011

Copyright Jason Allen Davis 2011
ALL RIGHTS RESERVED

ABSTRACT

Measurements of the flow velocity within rockets and gas-turbines prove to be a difficult problem due to the high temperature, high pressure, and high noise levels encountered. Velocity measurements in such environments are required to understand the physics of the flow field to improve the design and efficiency of these engine types. The design of a water-cooled jacket intended for use in conjunction with an existing novel, miniature fiber-optic LDV probe to make velocity measurements in these extreme engine environments is the topic of this research. The jacket design uses off-the-shelf materials and machining techniques in order to reduce cost and simplify manufacturing. The jacket was designed and drawn using the 3D parametric modeling software called SolidWorks. The SolidWorks CFD add-in, FloWorks, was used to numerically simulate the insertion of the water-cooled jacket into the afterburner or augmentor section of an air-breathing gas-turbine engine operating at 2000 K static temperature.

The augmentor diameter was chosen to be 18 inches based on the existing General Electric J-85 jet engine augmentor. Different configurations in which the combinations of jacket insertion distance, augmentor flow velocity Mach number, and alternate jacket tip designs were examined and analyzed in order to determine the operating conditions that will permit velocity measurements representative of the undisturbed freestream velocity. Computational results indicate that while a cooling water flow rate of 3 GPM allows for the successful operation of the jacket within the augmentor at Mach 0.7 and 2000 K, Mach numbers of 0.5 and below exhibit flow field disturbances that will allow for LDV measurements representative of the freestream.

DEDICATION

To all those who know:

I finally got it...

LIST OF ABBREVIATIONS AND SYMBOLS

Ω	Angular velocity
ρ	Fluid density
δ_{ij}	Kronecker delta function
τ_{ij}	Viscous shear stress tensor
τ_{ij}^R	Reynolds-stress tensor
$^{\circ}\text{C}$	Degrees Centigrade
$^{\circ}\text{F}$	Degrees Fahrenheit
$^{\circ}\text{R}$	Degrees Rankine
3D	Three-dimensional
AEDC	Arnold Engineering Development Center
atm	Atmosphere
C_B	Empirical constant
CCD	Charge-Coupled-Device
CFD	Computational Fluid Dynamics
cm	Centimeter
$C_{\epsilon 1}$	Empirical constant
$C_{\epsilon 2}$	Empirical constant
C_{μ}	Empirical constant
dc	Direct current

e	Internal energy
f_{μ}	Turbulent viscosity factor
GE	General Electric
g_i	Gravitational acceleration component along the i-th coordinate direction
GPM	Gallons per minute
h	Thermal enthalpy
IC	Internal combustion
ID	Inner diameter
in.	Inches
J	Joules
K	Kelvin
k	Turbulent kinetic energy
kg	Kilogram
Laser	Light Amplification by Stimulated Emission of Radiation
lbm	Pounds mass
LDA	Laser Diode Absorption
LDV	Laser Doppler Velocimetry
Le	Lewis number
LIBS	Laser-Induced Breakdown Spectroscopy
LIF	Laser-Induced Fluorescence
m	Meter
M	Molecular mass
mg	Milligrams

min	Minute
mm	Millimeters
OD	Outer diameter
p	Pressure
P_B	Turbulence generation due to buoyancy forces
PIV	Particle Image Velocimetry
PLIF	Planar Laser-Induced Fluorescence
Pr	Prandtl number
psi	Pounds per square inch
psia	Pounds per square inch absolute
psig	Pounds per square inch gauge
PWMA	Pressure Washer Manufacturers' Association
Q_H	Heat source or sink per unit volume
q_i	Diffusive heat flux
R	Gas constant
R_{univ}	Universal gas constant
s	Seconds
SFRJ	Solid Fuel Ramjet
S_i	Mass-distributed external force per unit mass
$S_{i,gravity}$	Mass-distributed external force per unit mass due to buoyancy
$S_{i,porous}$	Mass-distributed external force per unit mass due to porous resistance
$S_{i,rotation}$	Mass-distributed external force per unit mass due to coordinate system rotation
S_k	Turbulent kinetic energy source term

S_ε	Turbulent kinetic energy dissipation rate source term
T	Temperature
t	time
u	Fluid velocity
U	Particle velocity component perpendicular to the probe volume interference fringes
UV	Ultraviolet
W	Watts
x	Cartesian coordinate direction
Y	Concentration vector of fluid mixture components
y	Distance from wall
Y_m	Mixture component concentrations
α	Angle between intersecting laser beams
ε	Dissipation rate of turbulent kinetic energy
λ	Laser wavelength
μ	Dynamic viscosity coefficient
μm	Micrometer
μ_t	Turbulent eddy viscosity coefficient
σ_B	Empirical constant
σ_C	Empirical constant
σ_k	Empirical constant
σ_ε	Empirical constant

ACKNOWLEDGEMENTS

I would like to take this opportunity to extend my gratitude to my advisor, Dr. Semih Ölçmen, for his encouragement, patience, direction, and drive during my time as a graduate student at The University of Alabama. I would also like to thank my thesis committee members, Dr. Muhammad Ali Rob Sharif and Dr. Marcus Ashford, for providing their invaluable input, guidance, and assistance during the research process. The design, construction, and implementation of the probe used in this research could not have been possible without the extensive contributions provided by Mr. Tim Connell from the Department of Aerospace Engineering and Mechanics, along with Mr. Ken Dunn, Mr. Jim Edmonds, Mr. Sam Tingle, and Mr. James Yarbrough from the College of Engineering Machine Shop.

I would also like to thank Mr. Ben Rosow with MLC-CAD Systems for his patience, interest, and help with running the SolidWorks simulations used for this research. Without his knowledge, skills, and assistance, I would still be fumbling around trying to work out the problematic details associated with these models and computations.

I would especially like to thank my family and friends for all their support, encouragement, and perspective throughout the entirety of my academic career. I have always appreciated having these people to turn to during difficult and frustrating times. I would not be where I am today without all the jocularity they have brought into my life.

CONTENTS

ABSTRACT	ii
DEDICATION	iii
LIST OF ABBREVIATIONS AND SYMBOLS	iv
ACKNOWLEDGEMENTS	viii
LIST OF TABLES	xi
LIST OF FIGURES	xii
1. INTRODUCTION	1
1.1 Summary of Motivation	1
1.2 Organization	2
2. AUGMENTOR OVERVIEW	3
3. REVIEW OF LITERATURE	6
4. LASER DOPPLER VELOCIMETRY	27
4.1 LDV History and Background	27
4.2 LDV Probe	29
5. WATER-COOLED PROBE: DESIGN AND SIMULATION CONFIGURATIONS	32
5.1 Water-Cooled LDV Probe Design	32
5.2 Experimental Evaluation of Flow Rate through Probe	35
5.3 Numerical Simulation Setup	37
5.3.1 FloWorks Governing Equations	37
5.3.2 Mesh Settings	43

5.3.3 Probe Configurations	47
5.3.4 Initial and Boundary Conditions for Numerical Simulations	49
6. SIMULATION RESULTS AND DISCUSSION	51
6.1 Effects of Water-Cooled Probe on Flow Field	51
6.1.1 Effects of Jacket Insertion Distance on Augmentor Flow Field	52
6.1.2 Effects of Augmentor Inlet Mach number on Jacket/Flow Field Interaction	57
6.1.3 Effects of Jacket Tip Modification on Flow Field	62
6.2 Probe Tip Temperature Distributions	66
6.3 Cut Plane Temperature Distributions.....	70
7. CONCLUSIONS AND FUTURE WORK	75
7.1 Model Configurations	75
7.2 Conclusions.....	76
7.3 Future Work	76
REFERENCES	78
APPENDIX A.....	81
APPENDIX B	83
APPENDIX C	86
APPENDIX D.....	88
APPENDIX E	105
APPENDIX F.....	112

LIST OF TABLES

Table 1. FloWorks Simulation Test Matrix	49
Table 2. FloWorks Boundary Conditions	50
Table 3. Husky-HU80911A Pressure Washer Specifications.....	87

LIST OF FIGURES

Figure 1. Cutaway drawing of Pratt & Whitney F100-PW-229 afterburning turbofan engine (Ebrahimi, 2006).	4
Figure 2. Schematic of afterburning turbofan engine (Ebrahimi, 2006).....	4
Figure 3. Diagram of probe developed for subsonic arcjet exhaust analysis (Grey, 1962).	7
Figure 4. A) Asymmetric four tube cooling design. B) Symmetric annular cooling design (Lagen and Seiner, 1990).	8
Figure 5. Dual active heat flux gage probe assembly (Liebert and Kolodziej, 1995).	10
Figure 6. Schematic of optic/gas-sampling probe (Hurley, 1999).....	12
Figure 7. Schematic of air cooled probe protector shell (Bates and Pollack, 1999).....	13
Figure 8. Schematic of water-cooled LDV probe (Most, 2000).....	15
Figure 9. A) Cutaway view of probe head. B) Details of water-cooling scheme (Hiers and Hiers, June 2002)	16
Figure 10. Schematic and photograph of nickel electroformed probe (Beitel, 2004).....	17
Figure 11. Schematic drawing of high temperature direct probe for mass spectrometry (Bohátka, 2005).....	19
Figure 12. Schematic of optical probe concept (Suits, 2006).....	20
Figure 13. Design of water-cooled copper probe (Verscheure, 2006).....	21
Figure 14. Section view of water-cooled gas-sampling probe (Jiang, 2007).....	22
Figure 15. Photograph of prototype imaging probe components (Beitel, 2007).	23
Figure 16. A) Streamtraces in original pressure design. B) Streamtraces in modified probe design (Brouckaert, 2009).....	25

Figure 17. Schematic of high temperature endoscope equipped with CCD camera with details on incoming ray paths shown at top (Rottier, 2010).	26
Figure 18. Dual-beam laser Doppler anemometer arrangement (Albrecht, 2003).	28
Figure 19. Dual-beam laser Doppler arrangement with forward-scatter and backscatter detection (Albrecht, 2003).	29
Figure 20. Schematic of spark-plug LDV probe (Esirgemez and Ölçmen, 2005).	30
Figure 21. Cutaway view of jacket inserted into augmentor section.	34
Figure 22. Cutaway section view of jacket tip made with SolidWorks.	34
Figure 23. SolidWorks schematic of cooling jacket.	35
Figure 24. A) Photograph of cooling jacket. B) Photograph of cooling jacket with pressure washer wand and hose attached.	36
Figure 25. Lateral view of jacket inserted into augmentor with basic mesh applied at a mesh setting of 6.	44
Figure 26. Lateral view of jacket inserted into augmentor with refined mesh applied at a mesh setting of 6.	45
Figure 27. Magnified view of jacket tip with refined mesh applied at a mesh setting of 6.	45
Figure 28. Comparison of grid mesh setting for insertion distance equal to 50% of augmentor diameter along flow path length.	46
Figure 29. Magnification of comparison of grid mesh setting for insertion distance equal to 50% of augmentor diameter from 0.45 m to 0.55 m flow path length.	47
Figure 30. Image of probe configuration with flat tip inserted 50% of augmentor diameter.	48
Figure 31. Velocity distribution for Mach 0.7 augmentor flow with flat tip probe insertion of 50%: lateral view (left) and axial view (right).	52
Figure 32. Velocity distribution for Mach 0.7 augmentor flow with flat tip probe insertion of 75%: lateral view (left) and axial view (right).	53
Figure 33. Velocity distribution for Mach 0.7 augmentor flow with flat tip probe insertion of 88.9%: lateral view (left) and axial view (right).	53
Figure 34. Temperature distribution for Mach 0.7 augmentor flow with flat tip probe insertion of 50%: lateral view (left) and axial view (right).	54

Figure 35. Temperature distribution for Mach 0.7 augmentor flow with flat tip probe insertion of 75%: lateral view (left) and axial view (right).	55
Figure 36. Temperature distribution for Mach 0.7 augmentor flow with flat tip probe insertion of 88.9%: lateral view (left) and axial view (right).	55
Figure 37. Lateral views of velocity distribution for probe with flat tip at insertion of 50% at augmentor inlet Mach numbers of: A) Mach 0.7 B) Mach 0.5 C) Mach 0.3 D) Mach 0.1.	57
Figure 38. Axial views of velocity distribution for probe with flat tip at insertion of 50% at augmentor inlet Mach numbers of: A) Mach 0.7 B) Mach 0.5 C) Mach 0.3 D) Mach 0.1.	58
Figure 39. Lateral views of temperature distribution for probe with flat tip at insertion of 50% at augmentor inlet Mach numbers of: A) Mach 0.7 B) Mach 0.5 C) Mach 0.3 D) Mach 0.1.	60
Figure 40. Axial views of temperature distribution for probe with flat tip at insertion of 50% at augmentor inlet Mach numbers of: A) Mach 0.7 B) Mach 0.5 C) Mach 0.3 D) Mach 0.1.	61
Figure 41. Velocity distribution for Mach 0.7 augmentor flow with flat tip probe insertion of 50%.	62
Figure 42. Velocity distribution for Mach 0.7 augmentor flow with hemispherical tip probe insertion of 50%.	63
Figure 43. Velocity distribution for Mach 0.3 augmentor flow with flat tip probe insertion of 50%.	64
Figure 44. Velocity distribution for Mach 0.3 augmentor flow with hemispherical tip probe insertion of 50%.	64
Figure 45. Velocity distribution for Mach 0.1 augmentor flow with flat tip probe insertion of 50%.	65
Figure 46. Velocity distribution for Mach 0.1 augmentor flow with hemispherical tip probe insertion of 50%.	65
Figure 47. Magnified tip temperature distribution for Mach 0.7 augmentor flow with flat tip probe insertion of 50%.	66
Figure 48. Magnified tip temperature distribution for Mach 0.7 augmentor flow with flat tip probe insertion of 75%.	67

Figure 49. Magnified tip temperature distribution for Mach 0.7 augmentor flow with flat tip probe insertion of 88.9%.....	67
Figure 50. Magnified tip temperature distribution for Mach 0.5 augmentor flow with flat tip probe insertion of 50%.....	68
Figure 51. Magnified tip temperature distribution for Mach 0.5 augmentor flow with hemispherical tip probe insertion of 50%.	68
Figure 52. Magnified tip temperature distribution for Mach 0.7 augmentor flow with flat tip probe insertion of 50%—No water.....	69
Figure 53. Plane locations along jacket length (top). Temperature distribution for probe insertion of 50% at Mach 0.7 with flat tip at Plane 1 (bottom).	70
Figure 54. Temperature (left) and Fluid Temperature (right) distributions for probe insertion of 50% at Mach 0.7 with flat tip at Planes 2, 3, and 4.	72
Figure 55. Temperature (left) and Fluid Temperature (right) distributions for probe insertion of 50% at Mach 0.7 with flat tip at Planes 5, 6, and 7.	73
Figure 56. Temperature (left) and Fluid Temperature (right) distributions for probe insertion of 50% at Mach 0.7 with flat tip at Plane 8.	74
Figure 57. 3-View drawing of LDV probe casing	82
Figure 58. 3-View drawing of water-cooled probe with flat tip.....	84
Figure 59. 3-View drawing of water-cooled probe with hemispherical tip.....	85
Figure 60. Velocity distribution for Mach 0.7 augmentor flow with flat tip probe insertion of 50%.....	90
Figure 61. Velocity distribution for Mach 0.7 augmentor flow with hemispherical tip probe insertion of 50%.....	90
Figure 62. Velocity distribution for Mach 0.5 augmentor flow with flat tip probe insertion of 50%.....	91
Figure 63. Velocity distribution for Mach 0.5 augmentor flow with hemispherical tip probe insertion of 50%.....	91
Figure 64. Velocity distribution for Mach 0.3 augmentor flow with flat tip probe insertion of 50%.....	92
Figure 65. Velocity distribution for Mach 0.3 augmentor flow with hemispherical tip probe insertion of 50%.....	92

Figure 66. Velocity distribution for Mach 0.1 augmentor flow with flat tip probe insertion of 50%.....	93
Figure 67. Velocity distribution for Mach 0.1 augmentor flow with hemispherical tip probe insertion of 50%.....	93
Figure 68. Velocity distribution for Mach 0.7 augmentor flow with flat tip probe insertion of 75%.....	94
Figure 69. Velocity distribution for Mach 0.7 augmentor flow with flat tip probe insertion of 88.9%.....	94
Figure 70. Velocity distribution for Mach 0.7 augmentor flow with flat tip probe insertion of 50%—No water.....	95
Figure 71. Velocity distribution for Mach 0.7 augmentor flow with flat tip probe insertion of 75%—No water.....	95
Figure 72. Velocity distribution for Mach 0.7 augmentor flow with flat tip probe insertion of 88.9%—No water.....	96
Figure 73. Temperature distribution for Mach 0.7 augmentor flow with flat tip probe insertion of 50%.....	98
Figure 74. Temperature distribution for Mach 0.7 augmentor flow with hemispherical tip probe insertion of 50%.....	98
Figure 75. Temperature distribution for Mach 0.5 augmentor flow with flat tip probe insertion of 50%.....	99
Figure 76. Temperature distribution for Mach 0.5 augmentor flow with hemispherical tip probe insertion of 50%.....	99
Figure 77. Temperature distribution for Mach 0.3 augmentor flow with flat tip probe insertion of 50%.....	100
Figure 78. Temperature distribution for Mach 0.3 augmentor flow with hemispherical tip probe insertion of 50%.....	100
Figure 79. Temperature distribution for Mach 0.1 augmentor flow with flat tip probe insertion of 50%.....	101
Figure 80. Temperature distribution for Mach 0.1 augmentor flow with hemispherical tip probe insertion of 50%.....	101
Figure 81. Temperature distribution for Mach 0.7 augmentor flow with flat tip probe insertion of 75%.....	102

Figure 82. Temperature distribution for Mach 0.7 augmentor flow with flat tip probe insertion of 88.9%.....	102
Figure 83. Temperature distribution for Mach 0.7 augmentor flow with flat tip probe insertion of 50%—No water.	103
Figure 84. Temperature distribution for Mach 0.7 augmentor flow with flat tip probe insertion of 75%—No water.	103
Figure 85. Temperature distribution for Mach 0.7 augmentor flow with flat tip probe insertion of 88.9%—No water.	104
Figure 86. Magnified tip temperature distribution for Mach 0.7 augmentor flow with flat tip probe insertion of 50%.....	106
Figure 87. Magnified tip temperature distribution for Mach 0.7 augmentor flow with hemispherical tip probe insertion of 50%.	106
Figure 88. Magnified tip temperature distribution for Mach 0.5 augmentor flow with flat tip probe insertion of 50%.....	107
Figure 89. Magnified tip temperature distribution for Mach 0.5 augmentor flow with hemispherical tip probe insertion of 50%.	107
Figure 90. Magnified tip temperature distribution for Mach 0.3 augmentor flow with flat tip probe insertion of 50%.....	108
Figure 91. Magnified tip temperature distribution for Mach 0.3 augmentor flow with hemispherical tip probe insertion of 50%.	108
Figure 92. Magnified tip temperature distribution for Mach 0.1 augmentor flow with flat tip probe insertion of 50%.....	109
Figure 93. Magnified tip temperature distribution for Mach 0.1 augmentor flow with hemispherical tip probe insertion of 50%.	109
Figure 94. Magnified tip temperature distribution for Mach 0.7 augmentor flow with flat tip probe insertion of 75%.....	110
Figure 95. Magnified tip temperature distribution for Mach 0.7 augmentor flow with flat tip probe insertion of 88.9%.....	110
Figure 96. Magnified tip temperature distribution for Mach 0.7 augmentor flow with flat tip probe insertion of 50%—No water.....	111
Figure 97. Magnified tip temperature distribution for Mach 0.7 augmentor flow with flat tip probe insertion of 75%—No water.....	111

Figure 98. Magnified tip temperature distribution for Mach 0.7 augmentor flow with flat tip probe insertion of 88.9%—No water.....	111
Figure 99. Plane locations along jacket length (top). Temperature distribution for probe insertion of 50% at Mach 0.7 with flat tip at Plane 1 (bottom).	113
Figure 100. Temperature (left) and Fluid Temperature (right) distributions for probe insertion of 50% at Mach 0.7 with flat tip at Planes 2, 3, and 4.	114
Figure 101. Temperature (left) and Fluid Temperature (right) distributions for probe insertion of 50% at Mach 0.7 with flat tip at Planes 5, 6, and 7.	115
Figure 102. Temperature (left) and Fluid Temperature (right) distributions for probe insertion of 50% at Mach 0.7 with flat tip at Plane 8.	116
Figure 103. Plane locations along jacket length (top). Temperature distribution for probe insertion of 50% at Mach 0.7 with hemispherical tip at Plane 1 (bottom).	116
Figure 104. Temperature (left) and Fluid Temperature (right) distributions for probe insertion of 50% at Mach 0.7 with hemispherical tip at Planes 2, 3, and 4.	117
Figure 105. Temperature (left) and Fluid Temperature (right) distributions for probe insertion of 50% at Mach 0.7 with hemispherical tip at Planes 5, 6, and 7.	118
Figure 106. Temperature (left) and Fluid Temperature (right) distributions for probe insertion of 50% at Mach 0.7 with hemispherical tip at Plane 8.	119
Figure 107. Plane locations along jacket length (top). Temperature distribution for probe insertion of 50% at Mach 0.5 with flat tip at Plane 1 (bottom).	119
Figure 108. Temperature (left) and Fluid Temperature (right) distributions for probe insertion of 50% at Mach 0.5 with flat tip at Planes 2, 3, and 4.	120
Figure 109. Temperature (left) and Fluid Temperature (right) distributions for probe insertion of 50% at Mach 0.5 with flat tip at Planes 5, 6, and 7.	121
Figure 110. Temperature (left) and Fluid Temperature (right) distributions for probe insertion of 50% at Mach 0.5 with flat tip at Plane 8.	122
Figure 111. Plane locations along jacket length (top). Temperature distribution for probe insertion of 50% at Mach 0.5 with hemispherical tip at Plane 1 (bottom).	122
Figure 112. Temperature (left) and Fluid Temperature (right) distributions for probe insertion of 50% at Mach 0.5 with hemispherical tip at Planes 2, 3, and 4.	123
Figure 113. Temperature (left) and Fluid Temperature (right) distributions for probe insertion of 50% at Mach 0.5 with hemispherical tip at Planes 5, 6, and 7.	124

Figure 114. Temperature (left) and Fluid Temperature (right) distributions for probe insertion of 50% at Mach 0.5 with hemispherical tip at Plane 8.	125
Figure 115. Plane locations along jacket length (top). Temperature distribution for probe insertion of 50% at Mach 0.3 with flat tip at Plane 1 (bottom).	125
Figure 116. Temperature (left) and Fluid Temperature (right) distributions for probe insertion of 50% at Mach 0.3 with flat tip at Planes 2, 3, and 4.	126
Figure 117. Temperature (left) and Fluid Temperature (right) distributions for probe insertion of 50% at Mach 0.3 with flat tip at Planes 5, 6, and 7.	127
Figure 118. Temperature (left) and Fluid Temperature (right) distributions for probe insertion of 50% at Mach 0.3 with flat tip at Plane 8.	128
Figure 119. Plane locations along jacket length (top). Temperature distribution for probe insertion of 50% at Mach 0.3 with hemispherical tip at Plane 1 (bottom).	128
Figure 120. Temperature (left) and Fluid Temperature (right) distributions for probe insertion of 50% at Mach 0.3 with hemispherical tip at Planes 2, 3, and 4.	129
Figure 121. Temperature (left) and Fluid Temperature (right) distributions for probe insertion of 50% at Mach 0.3 with hemispherical tip at Planes 5, 6, and 7.	130
Figure 122. Temperature (left) and Fluid Temperature (right) distributions for probe insertion of 50% at Mach 0.3 with hemispherical tip at Plane 8.	131
Figure 123. Plane locations along jacket length (top). Temperature distribution for probe insertion of 50% at Mach 0.1 with flat tip at Plane 1 (bottom).	131
Figure 124. Temperature (left) and Fluid Temperature (right) distributions for probe insertion of 50% at Mach 0.1 with flat tip at Planes 2, 3, and 4.	132
Figure 125. Temperature (left) and Fluid Temperature (right) distributions for probe insertion of 50% at Mach 0.1 with flat tip at Planes 5, 6, and 7.	133
Figure 126. Temperature (left) and Fluid Temperature (right) distributions for probe insertion of 50% at Mach 0.1 with flat tip at Plane 8.	134
Figure 127. Plane locations along jacket length (top). Temperature distribution for probe insertion of 50% at Mach 0.1 with hemispherical tip at Plane 1 (bottom).	134
Figure 128. Temperature (left) and Fluid Temperature (right) distributions for probe insertion of 50% at Mach 0.1 with hemispherical tip at Planes 2, 3, and 4.	135
Figure 129. Temperature (left) and Fluid Temperature (right) distributions for probe insertion of 50% at Mach 0.1 with hemispherical tip at Planes 5, 6, and 7.	136

Figure 130. Temperature (left) and Fluid Temperature (right) distributions for probe insertion of 50% at Mach 0.1 with hemispherical tip at Plane 8.	137
Figure 131. Plane locations along jacket length (top). Temperature distribution for probe insertion of 75% at Mach 0.7 with flat tip at Plane 1 (bottom).	137
Figure 132. Temperature (left) and Fluid Temperature (right) distributions for probe insertion of 75% at Mach 0.7 with flat tip at Planes 2, 3, and 4.	138
Figure 133. Temperature (left) and Fluid Temperature (right) distributions for probe insertion of 75% at Mach 0.7 with flat tip at Planes 5, 6, and 7.	139
Figure 134. Temperature (left) and Fluid Temperature (right) distributions for probe insertion of 75% at Mach 0.7 with flat tip at Plane 8.	140
Figure 135. Plane locations along jacket length (top). Temperature distribution for probe insertion of 88.9% at Mach 0.7 with flat tip at Plane 1 (bottom).	140
Figure 136. Temperature (left) and Fluid Temperature (right) distributions for probe insertion of 88.9% at Mach 0.7 with flat tip at Planes 2, 3, and 4.	141
Figure 137. Temperature distribution for probe insertion of 88.9% at Mach 0.7 with flat tip at Planes 3 with alternate temperature scale range.	142
Figure 138. Temperature (left) and Fluid Temperature (right) distributions for probe insertion of 88.9% at Mach 0.7 with flat tip at Planes 5, 6, and 7.	143
Figure 139. Temperature (left) and Fluid Temperature (right) distributions for probe insertion of 88.9% at Mach 0.7 with flat tip at Plane 8.	144

CHAPTER 1

INTRODUCTION

The purpose of this chapter is to provide a brief overview of the motivation for the research conducted and discussed in this thesis in Section 1.1 while Section 1.2 describes the layout of the topics discussed throughout.

1.1 Summary of Motivation

Information gathered within critical zones of engines—including the combustor, afterburner/augmentor, and locations downstream of the exit nozzle—is vital for the determination of combustor efficiency, material integrity, and engine performance. This information may be gathered using flow field probes and optical measurement techniques in locations where physical and optical access allows for the placement of line-of-sight measurements for laser-based optical equipment and probe hardware (Savage, 2006). The extreme conditions experienced within the environments of the aforementioned critical zones of engines limits the ability to collect information using un-cooled probes and equipment. Adding cooling systems to the data collection hardware allows these probes to be placed directly into the harsh conditions found in the engine critical zones. The research presented here discusses the process of design, construction, numerical simulation, and analysis of a water-cooled probe used for laser Doppler velocimetry (LDV) measurements in the augmentor section of a General Electric (GE) J-85 jet engine.

1.2 Organization

The research presented in this thesis has been organized into seven chapters. A brief overview of the design and operation of augmentors is discussed in chapter two. A variety of designs, methods, and applications of water cooling probes throughout an array of research topics and areas is presented in the form of a literature review in chapter three. The fourth chapter provides a brief history of the laser Doppler velocimetry measurement technique and how a probe utilizing this method of data collection has driven the design of the water-cooling probe presented in this work. Chapter five provides details on the design and setup of the numerical simulation of the water-cooling probe. The sixth chapter presents and discusses the results of the computational analysis of the complex heat transfer and effects of the probe on the flow field within the augmentor section of a jet engine. The seventh and final chapter presents the conclusions reached through this research and provides several possible methods to further the research and analysis.

CHAPTER 2

AUGMENTOR OVERVIEW

The purpose of this chapter is to provide some information on the design and operation of gas-turbine augmentors in order to better understand why the development of a water-cooled probe is necessary. Without cooling, the probes and data collection hardware are subjected to the extreme conditions observed in these types of engine environments.

An augmentor is an auxiliary burner attached to the tailpipe of a jet engine for the purpose of injecting fuel into the hot exhaust gases and burning the injected fuel to provide extra thrust for a short duration (Ebrahimi, 2006). Increased performance levels provided by augmentors—which are both useful and necessary in the application of military aircraft for operations such as takeoff, climb, missile evasion, and a variety of combat maneuvers—can increase the total thrust by 50 to 90 percent. Augmentors may be found in both turbofan and turbojet engines. Turbofan engines, as compared to turbojet engines, accelerate a larger mass of air while consuming less fuel for the production of a given amount of useful power, which results in a higher propulsive efficiency (Ebrahimi, 2006). A cutaway drawing of a Pratt & Whitney F100-PW-229 afterburning turbofan engine is shown in Figure 1, while a general turbofan schematic is shown in Figure 2 (Ebrahimi, 2006).

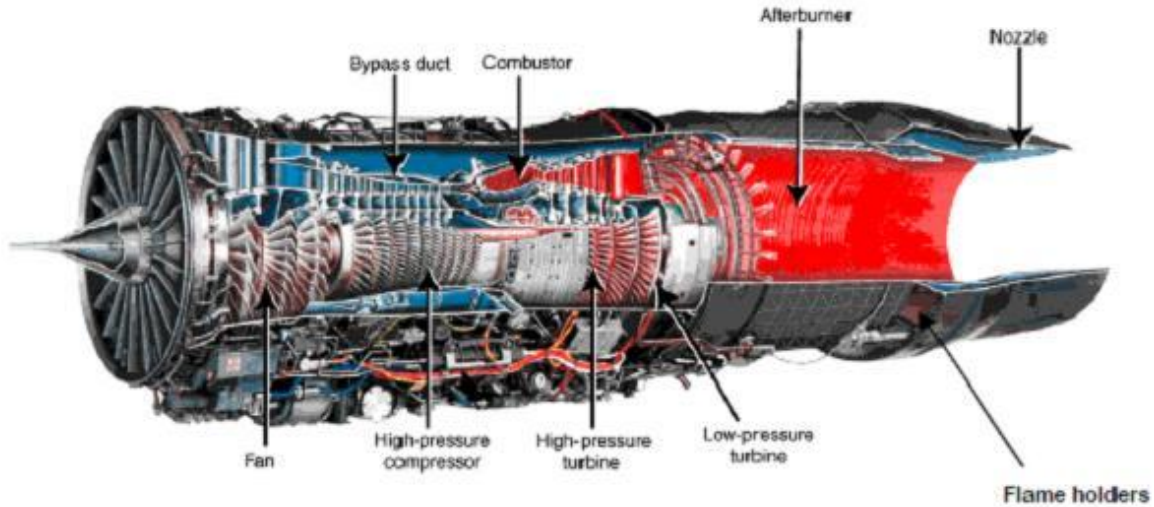


Figure 1. Cutaway drawing of Pratt & Whitney F100-PW-229 afterburning turbofan engine (Ebrahimi, 2006).

Figure 1 shows key engine components such as the fan, high-pressure compressor, combustor, high and low-pressure turbines, bypass duct, afterburner, and nozzle. The term “engine core” is given to the combination of the high-pressure compressor, combustor, and high-pressure turbine with the augmentor immediately behind the turbine section, but ahead of the convergent/divergent exhaust nozzle with variable throat size. The augmentor section includes the tail cone, with igniters and spray bars, along with chute cooling and mixing hardware (Ebrahimi, 2006).

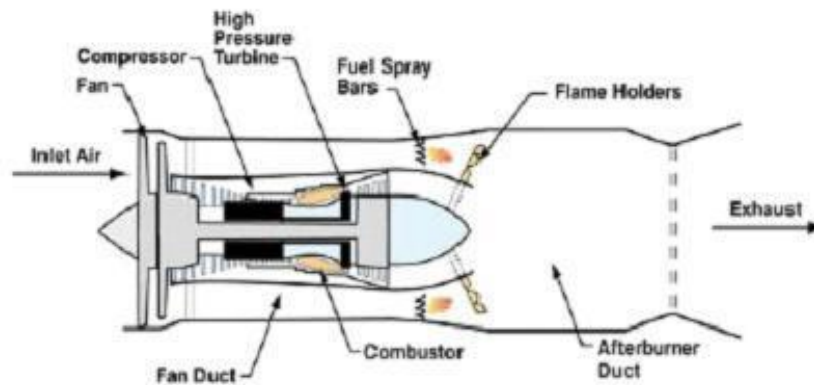


Figure 2. Schematic of afterburning turbofan engine (Ebrahimi, 2006).

Augmentors operate by first mixing injected fuel with the core engine bypass air. The additional fuel is then ignited and burned to increase both the total temperature and velocity of the flow exiting through the nozzle. The fuel is injected into the augmentor in a liquid state and atomized by the turbine exhaust flow shear forces. The atomized fuel evaporates and mixes with available oxygen for combustion (between the engine turbine exit and the exhaust nozzle) started within the flameholders (required for continuous-combustion jet engines) and thereby provides additional energy to the flow stream. The flow stream then exits through a variable-geometry nozzle, which is necessary in order to account for the variations in flow temperature, pressure, density, and velocity (properties correspondent to the mass flow rate of the augmentor flow) experienced when operating with or without the afterburner (Ebrahimi, 2006). Augmenting the flow through the engine has both benefits and penalties. Benefits come in the form of increased thrust and performance capabilities while the penalties include added weight (which is a result of the equipment necessary to alter the nozzle geometry), higher fuel consumption, and higher fuel costs.

Augmentor design, like all designs, begins with design goals and mission priorities. The goals and priorities of aircraft include performance, weight, size, cost, reliability, durability, survivability, and the range of conditions within the aircraft flight envelope. Afterburner design must account for, and consider, all performance tradeoffs in order to minimize the detriment to the performance of the propulsion system (Ebrahimi, 2006). The undisturbed flow in the augmentor section of this research is nominally expected to travel at Mach 0.7 and reach a temperature of 2000 K. These flow parameters are modeled numerically in order to simulate the interaction of an intrusive probe inserted into the augmentor section of a GE J-85 jet engine.

CHAPTER 3

REVIEW OF LITERATURE

The purpose of this chapter is to explain the methods and intentions for which water-cooling probes or jackets have been used throughout the research world. Cooling systems are required in intrusive measurement probes to gather different forms of data within extreme environment flows. While various cooling methods include gases or non-water liquids, using water as a cooling medium is widely used in cooling probes because of its abundance, neutrality, and ease of access.

The use of cooling probes for data collection dates at least as far back as the early 1960's in which Grey et al. (1962) developed a water-cooled gas-sampling probe capable of steady-state operation at 15,000 K and one atmosphere to determine temperature, velocity, and chemical composition in a subsonic arcjet exhaust. A diagram of the probe developed is shown below in Figure 3. Gas sampling is conducted through the center passage of the probe with inner and outer cooling channels surrounding this passage. The overall diameter of the probe is approximately 0.125 inches. Collected gas is carried through the probe to a gas sample tube and continues on to the data collection instruments and equipment (Grey, 1962). The majority of this probe is constructed from copper while the supports are made of stainless steel. The cooling water used reaches a pressure up to 500 psi and passes through the outer channel of the probe via the mounting block and the front stainless steel support. After traveling through the outer

channel, the water proceeds to the tip of the probe and returns through the inner channel where it exits by passing through the rear support and the mounting block.

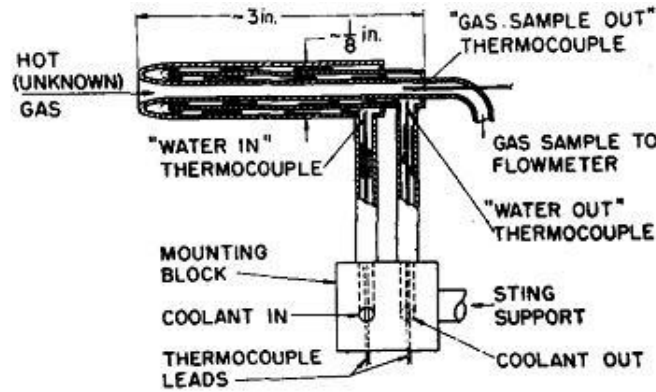


Figure 3. Diagram of probe developed for subsonic arcjet exhaust analysis (Grey, 1962).

Five years later, a similar water-cooling approach was used to evaluate the ability of an electrostatic probe to measure local electron temperature, electron density, floating potential, and saturation current ratio in dense argon plasmas (Grey and Jacobs, 1967). These subsonic argon plasmajets reached temperatures up to 20,000 °R (~11,000 K) at pressures up to one atmosphere. The cooled electrostatic probe consists of a 0.075-in.-diameter calorimetric probe coated with a zirconium oxide/boron nitride composition to provide additional insulation. The cooling method currently being discussed differs from that described in Figure 3 (Grey, 1962) by having the cooling water enter through the rear support, up the support, and along the inner channel. To exit, the water reaches the probe tip, travels along the outer cooling channel, and exits through the first support and mounting block (Grey and Jacobs, 1967).

Water-cooling has also been used in supersonic probes to study high temperature jet plumes. From the options of using total pressure, static pressure, and total temperature probes to develop and test the water-cooled probe concept, the total pressure probe was selected for its simplistic internal geometry relative to the others. Lagen and Seiner (1990) built two total

pressure probes from AISI Type-347 Stainless Steel tubing in order to test and determine whether an asymmetric four tube cooling design or a symmetric annular cooling design is a superior cooling concept. Figure 4 shows the two proposed cooling techniques used by Lagen and Seiner (1990) for use in a Mach 2 flow at 2000 °F (~1366 K) exit total temperature.

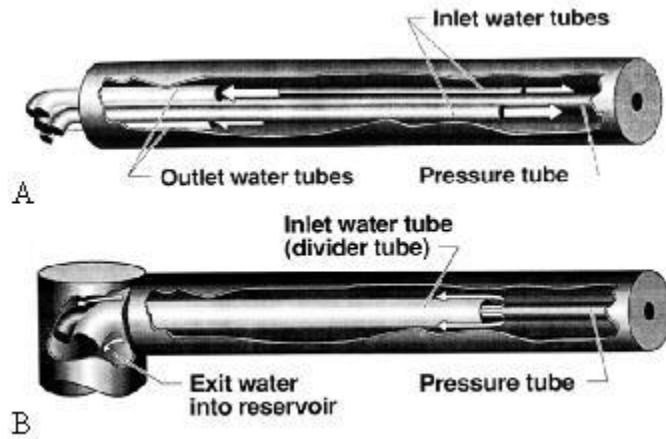


Figure 4. A) Asymmetric four tube cooling design. B) Symmetric annular cooling design (Lagen and Seiner, 1990).

The asymmetric cooling design uses two water inlet tubes which extend up to the tip of the probe with the remaining two tubes located near the rear of the probe for water exit. This asymmetric cooling technique was shown to be less effective than the symmetric cooling technique due to the increased internal tubing and decreased water volume (Lagen and Seiner, 1990). The annular cooling method uses a single internal dividing tube from which water enters the probe. Water travels toward the probe tip, floods the casing interior, and exits around the outside of the dividing tube near the rear of the probe. These annular cooling probes have water mass flow rates of 0.0128 lbm/s for the total pressure probe, 0.0185 lbm/s for the static pressure probe, and 0.0650 lbm/s for the total temperature probe (Lagen and Seiner, 1990). Prior to using water-cooling, un-cooled probes used in the environment mentioned above often failed at and above 755 K (Lagen and Seiner, 1991). However, after implementing the water-cooling, the new

probes sustained temperatures up to 1366 K for extended periods of time (Lagen and Seiner, 1991).

While the use of water as a cooling medium in probes is a common choice in various areas of research because of its ability to effectively transport heat, gas cooling eliminates the water leak hazard (Bates and Pollack, 1999) and may be required in some cases such as for the surface heat flux gage probe developed by Liebert and Kolodziej (1995). This cooling probe uses air for cooling because of the requirements of the miniature plug-type heat flux gauges previously developed and tested by Liebert (1992, 1994). The probe consists of a miniature convection cooled metal plug-type heat flux gage (Liebert, 1992) welded to the end of a hollowed out stainless steel bolt. The hole was not machined through the entire length of the bolt, which allowed for the formation of a platform at the bottom of the bolt hole. Inside the bolt, there exists a small tube which is placed a distance of 1.2 times the tube diameter from the platform bottom. Cooling air flows through the inner tube, impinges on the platform welded to the end of the bolt which contacts the rear of the thermoplug, and exits through the annulus passage formed between the tube and bolt wall (Liebert and Kolodziej, 1995). This assembled probe body may be seen below in Figure 5.

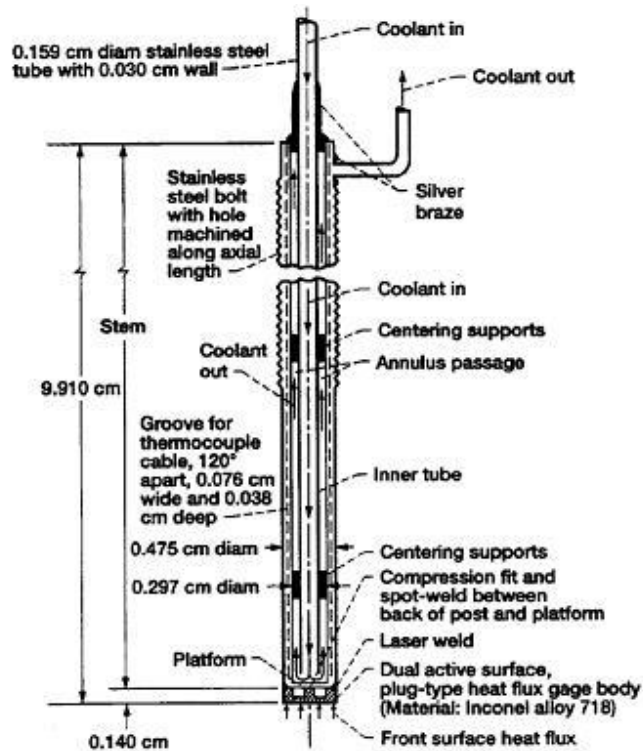


Figure 5. Dual active heat flux gage probe assembly (Liebert and Kolodziej, 1995).

Water-cooling is desired over air cooling when the experiments involve taking measurements of the products of combustion reactions because the chemical reactions that would otherwise be taking place in the sampling probe are minimized which allows products to be measured as they exist at a particular point in the flow (Hurley, 1999). A cooled sampling probe system was designed to measure both gaseous and solid reaction product distributions inside a solid fuel ramjet (SFRJ) combustion chamber (Ciezki and Schwein, 1996). The solid fuel used in the SFRJ contained added boron to provide a better energetic performance; however, the complete combustion of boron particles is inhibited by the formation of a layer of molten boronoxide (Ciezki and Schwein, 1996). The sampling probe was constructed of three concentric thin walled stainless steel tubes and an outer copper tube with a 7 mm outer diameter to provide an annular cooling channel (copper and two outer-most stainless steel tubes) and a flow collection tube (inner-most stainless steel tube with an internal diameter of 3 mm). The gap

between the two inner-most stainless steel tubes provides a channel for helium to travel to the copper probe tip to quench the reaction products by dilution with an inert gas (Ciezki and Schwein, 1996). The helium is added after the collected flow has traveled past the tip and into the inner stainless steel tube.

Enthalpy probes are diagnostic tools designed for use in high temperature fluid flows. Cooled and un-cooled enthalpy probes were used to determine the effects of rapid changes in flow density on the measured stagnation pressure (Jankovic and Mostaghimi, 1998). The effects of density on the flow field are determined by comparing the stagnation pressures measured by each probe along the symmetry axis of an atmospheric argon dc plasma jet. The plasma jet freestream temperature around the probe tips was calculated from the measured enthalpy to be in the range of 1500-5500 K. The cooled and un-cooled enthalpy probes used were custom built for the experiments and utilized an annular cooling technique. A set of concentric tubes were used to create flow channels with a divider. The water travels down the probe between the divider and inner tube with ID = 1.2 mm then exits the probe through the channel between the divider and the outer tube with OD = 4.8 mm (Jankovic and Mostaghimi, 1998). Few other details were provided on the cooling scheme of these experiments.

One reason experimental measurements are important is that they aid in the development of new, or improvement of current, gas-turbine combustion systems because they provide a method of verification for computational models (Hurley, 1999). An intrusive optic/gas-sampling water-cooled probe was developed to help understand the combustion processes fully, which then aided in the development of these computational fluid dynamics (CFD) models. The combination of these flow analysis methods provides time averaged data collection (gas

sampling) as well as real time measurements (optical). A schematic of this optical/gas-sampling probe is shown below in Figure 6.

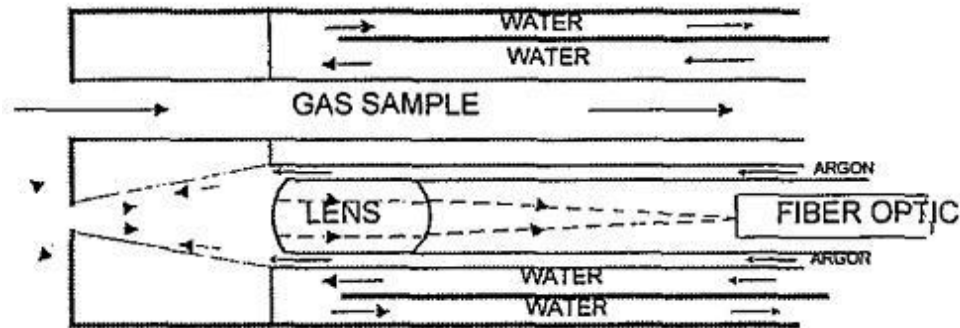


Figure 6. Schematic of optic/gas-sampling probe (Hurley, 1999).

Two separate tubes are used for the data collection; one tube for gas sampling to analyze the concentration of species common in combustion reactions and the second contains a lens and optical fiber to form parts of an optical pyrometer. These two tubes are encased by a water-cooled jacket measuring 1300 mm long and 9.5 mm in diameter. The water-cooling allows the probe to survive in a working combustor, provides a cool environment for the optics to reliably perform, and minimizes chemical reactions taking place within the gas-sampling probe (Hurley, 1999). The cooling water is pumped through the probe in a closed loop at high pressure in order to prevent boiling. Along with the cooling water, an argon purge flow passes around the optics and out of the probe tip to eliminate soot laden gases from collecting on the lens. The cooled probe was inserted into a combustion chamber with a temperature between 1300 K and 2600 K.

Bates and Pollack (1999) developed gas-cooled protector shells to extend the operating limits of a variety of optical probes enclosed by the shells. These protector shells were designed to withstand the environments found in industrial processes including temperatures ranging from the boiling point of liquid nitrogen to combustion reactions; pressure ranges from high vacuums

to thousands of atmospheres; and reactivity extremes including acids and bases (Bates and Pollack, 1999). A schematic of the probe protector shell may be seen below in Figure 7.

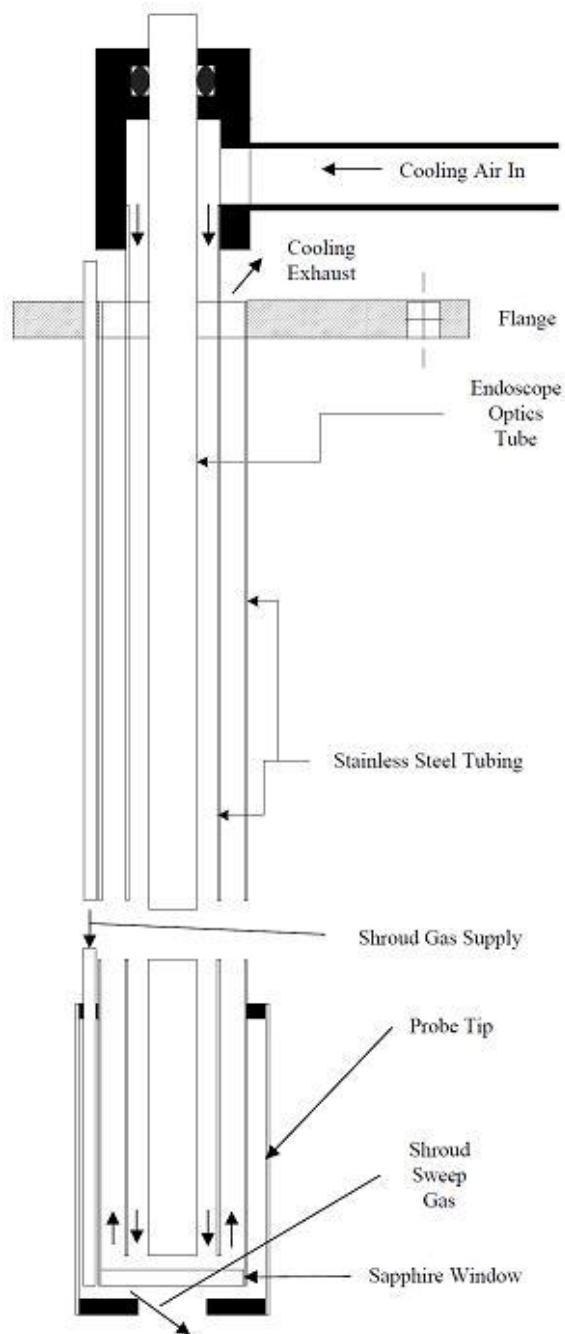


Figure 7. Schematic of air cooled probe protector shell (Bates and Pollack, 1999).

The protector shell consists of three concentric stainless steel tubes. The outer-most tube of the shell is used to supply and contain the tip purge flow. The middle tube is used to hold the

sapphire window and the inner-most tube is used as an internal flow separator. The optical probe being used lies concentrically within the flow separating tube. The cooling fluid enters the shell between the optical probe and the flow separator tube, and exits between the separator and the outer tubing that holds the sapphire window. To test the protector shell design, a 2.5 cm OD probe (without the outer-most stainless steel tube, leaving only the window-holding tube) was constructed. The optical probe used had a 9.5 mm diameter. Using air as a cooling fluid at a flow rate of 23 standard liters/min, the optical probe reached 100 °C after the assembly was inserted into a furnace with an operating temperature of 500 °C. While possible, it would be more difficult to cool with air at higher temperatures (Bates and Pollack, 1999).

While the probe protector shells developed by Bates and Pollack (1999) were created for a variety of uses, many other studies had specific goals. One such goal was to scientifically design, develop, optimize, and use a new specific probe for velocity and turbulence measurements in the burner zone of a full scale pulverized coal power plant (Most, 2000). In this study, the authors sought to map the flow field near the exit of a pulverized coal burner using a 3D LDV system. The water-cooled probe developed for these measurements, shown in Figure 8, was designed to operate in an environment at a mean temperature of approximately 1500 °C. This probe, meant to maintain the optical system at a maximum temperature of 50 °C, was constructed of stainless steel with a total length of 6.5 m, 114 mm OD, and a 64 mm ID in order to accept a 60 mm diameter beam expander and side looking section. The side looking section is used to focus the laser beams laterally after reflection on a mirror (Most, 2000). Nitrogen and Argon are used inside the probe to help prevent water condensation and particle collection, respectively, on the optical elements. The probe design utilized an annular cooling technique

with the water traveling towards the probe tip around the LDV head and exiting through the outer-most channel.

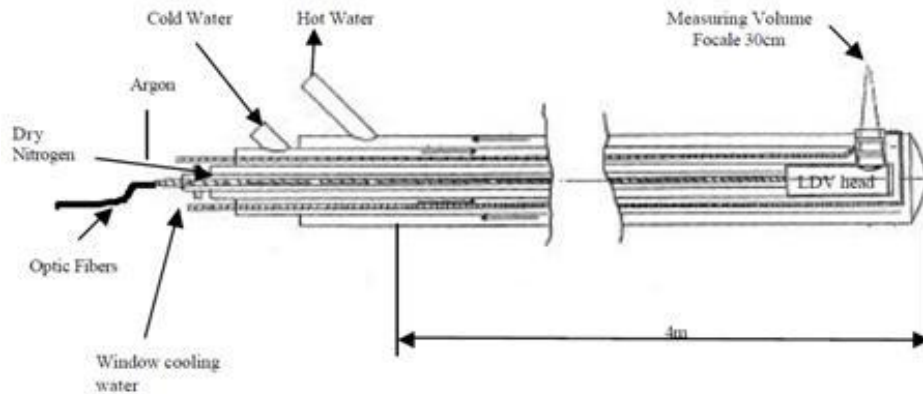


Figure 8. Schematic of water-cooled LDV probe (Most, 2000).

Use of a side looking, or periscope, design is not unique to LDV measurement techniques. Other probes have been developed for the measurement of total temperature, static and total pressure, enthalpy, and composition in a wide range of flow conditions (Hiers and Hiers, June 2002). Probes have also been developed to allow viewing within the augmentor of aircraft turbine engines during operation (Hiers and Hiers, July 2002). The probes were fabricated using 304 stainless steel with diameters ranging from 0.125 to 1.0 in. and do not include any type of window. Instead of a window, the probes use an objective aperture with a diameter of 0.0625 in. purged with dry nitrogen at a minimum pressure of 300 psia to prevent high temperature gas from flowing into the probe body (Hiers and Hiers, June 2002). Figure 9, below, shows the view port, reflective mirror, and the complex design of the water-cooling scheme.

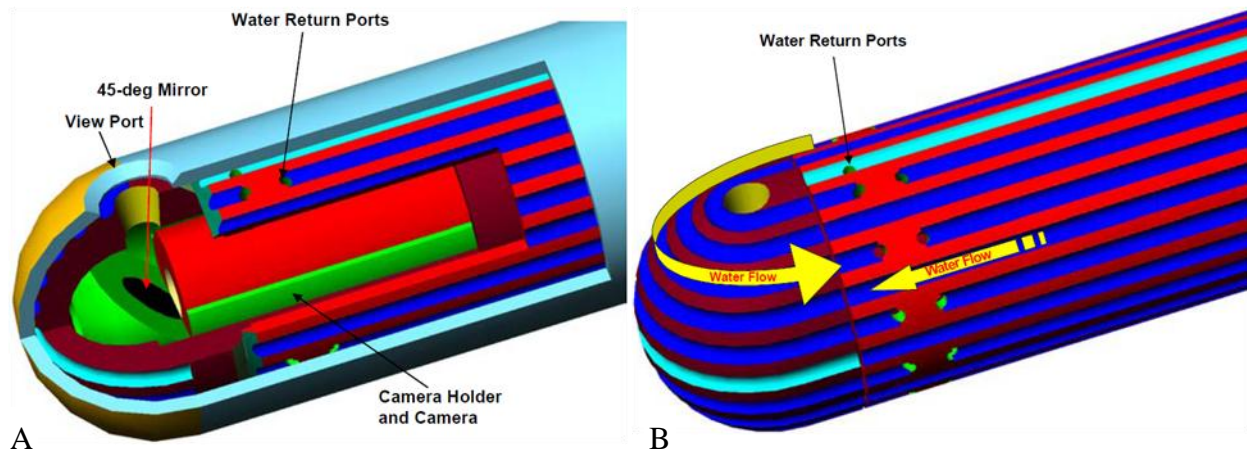


Figure 9. A) Cutaway view of probe head. B) Details of water-cooling scheme (Hiers and Hiers, June 2002)

Water flows through the probe channels at a rate of 4 to 5 GPM with an optimal pressure of 1700 psig. These flow conditions within the probe are required to increase the boiling point of the coolant (Hiers and Hiers, June 2002). Rake bodies have also been developed for use with interchangeable probes using this cooling method to measure Pitot pressure, Mach/flow angularity, gas sampling, particulate emissions sampling, stagnation temperature, or imaging in the exit plane of aircraft turbine engines operating at maximum afterburner conditions (Hiers and Hiers, July 2002). Years later, this viewing probe was used as a system platform to image engine and afterburner exhaust in ultraviolet (UV) wavelengths (Savage, 2006). The imaging system is comprised of an afterburner-capable imaging probe, UV-grade quartz coherent fiber bundle, and a hyperspectral imager. The internals of the original viewing probe were altered and adapted for use with this UV system, which has an adjustable field of view range from a pinpoint to the entire exhaust plume of the turbine engine flow (Savage, 2006).

Electroforming is a fabrication technique being used for the development of high temperature flow field probes and supporting rake structures to alleviate the limitations of conventional fabrication techniques such as degraded cooling effectiveness, cooling path geometry restrictions, and probe size limitations (Beitel, 2004). Beitel et al. (2004) selected a

Mach number/flow angularity probe with an outer diameter of 6.36 mm as their first diagnostic hardware to incorporate electroforming into construction because conventional machine shop processes would require complex machining and welding. The probe consists of a Pitot tube and four static pressure tubes along with the channelized water-cooling loop. Cooling channels were machined into the outer surface of a stainless steel tube with an aluminum body assembled around the data collection tubes and the forward end of the stainless steel tube. After machining, the cooling channels were filled with a soluble material to maintain the channels and approximately 0.8-mm-thick nickel electroform was applied to the probe assembly (Beitel, 2004). The probe was machined down to achieve the desired configuration and the aluminum and soluble material filling were then removed. A schematic and photograph of this electroformed probe may be seen in Figure 10. This probe was successfully tested and used in the exit plane of a gas-turbine engine operating under afterburner conditions. Beitel et al. (2004) also developed an electroformed rake and probe holder assembly, a miniature gas-extraction probe, and a miniature Mach number/flow angularity probe. Additional information on electroforming and the re-designing of several probes previously discussed are also described in this reference (Beitel, 2004).

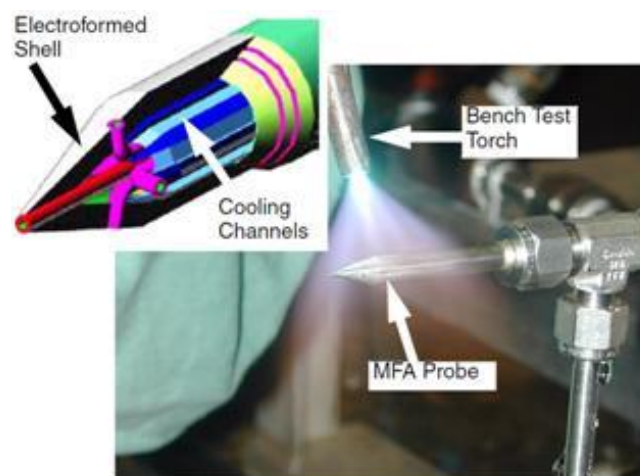


Figure 10. Schematic and photograph of nickel electroformed probe (Beitel, 2004).

MacKinnon et al. (2004) also utilized the electroforming technique to fabricate a series of probes including: stream thrust probe, turbine engine emissions probe, Mach flow angularity probe, and a total temperature probe. A set of future probe designs and applications which were being researched at the time included: a high-speed fiber-optic imaging probe, a miniaturized gas extraction probe, a miniaturized Mach flow angularity/swirl probe, a microelectromechanical systems based gaseous extraction probe, and an optical embedded instrumentation probe. Each of these probes incorporated the use of electroforming to create water-cooling passages similar to those discussed by Beitel et al. (2004) for use within harsh environments such as gas-turbine engines. These designs and efforts led to a focus on the miniaturization of the probes (probes with diameters ranging from 0.05 to 0.10 in.) in order to minimize flow distortion (MacKinnon, 2004). Details on each probe mentioned in the lists above—including the specifics of the water-cooling, electroforming fabrication, and areas of use—may be found in the reference (MacKinnon, 2004).

High temperature augmentor flow streams are of increasing interest to the research community, along with the need for more robust flow field diagnostics (Beitel, 2005). The use and miniaturization of intrusive probes is necessary in order to embed the diagnostic systems in gas-turbine engine environments and minimize flow distortion (Beitel, 2005). A miniature embedded gas-extraction probe with an outer diameter of 2.5 mm and an inner gas extraction channel diameter of 1.25 mm was created using tubular components and electroforming. This probe was installed into the combustor of a J85-GE-5 turbojet engine operating at engine power settings up to maximum afterburner where temperatures were estimated to be around 1925 °C. A miniature embedded flow angularity or swirl probe with an outer diameter of 6.35 mm was also fabricated which included multiple static pressure ports used to resolve flow angle (Beitel, 2005).

These probes use the same water-cooling and electroforming schemes as previously discussed by Beitel et al. (2004) and McKinnon et al. (2004).

Water-cooling is not limited to intrusive measurement probes. It has also been used for mass spectrometry systems such as the one described and developed by Bohátka et al. (2005).

The mass spectrometry probe developed is shown in Figure 11, below.

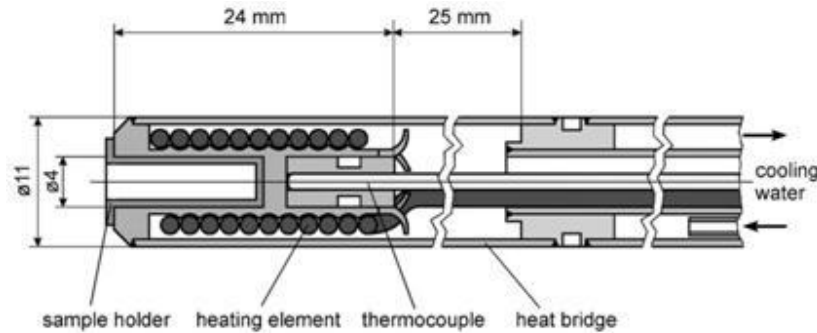


Figure 11. Schematic drawing of high temperature direct probe for mass spectrometry (Bohátka, 2005).

The upper portion or probe tip is where heating occurs and is constructed of heat resistant stainless steel and nickel. A heating element is wound around a threaded body which includes the mass spectrometry sample holder (holds 0.1-30 mg of sample material) and a thermocouple. The threaded body is welded into the covering tube after probe assembly. A thin-walled heat bridge exists between the heating element and the water-cooled probe handle which is sealed with an o-ring (Bohátka, 2005). Few details are provided on the specifics of the water-cooling scheme, but the maximum operating temperature of the probe is 800 °C.

While taking measurements within the flows of gas-turbine combustors using the gas extraction technique as discussed by Beitel et al. (2005) has proven to be useful, an inherent limitation with this technique is the time lag required to transport the gas sample to the detector and/or the time response of the sensor itself (Suits, 2006). This time lag may be eliminated by using in-situ optical measurement techniques to evaluate the gas composition directly in the flow

stream. These optical techniques, including laser-induced fluorescence (LIF); planar laser-induced fluorescence (PLIF) imaging; laser diode absorption (LDA) spectroscopy; and laser-induced breakdown spectroscopy (LIBS), are typically non-intrusive and may be integrated into water-cooled probes to take measurements where specially designed optical access ports are either impractical or impossible (Suits, 2006). An optical probe was developed by Suits et al. (2006) to incorporate non-intrusive optical measurement techniques such as LDA and LIF for use in combustor and augmentor flameholder zones. A concept schematic drawing of this optical probe may be seen in Figure 12.

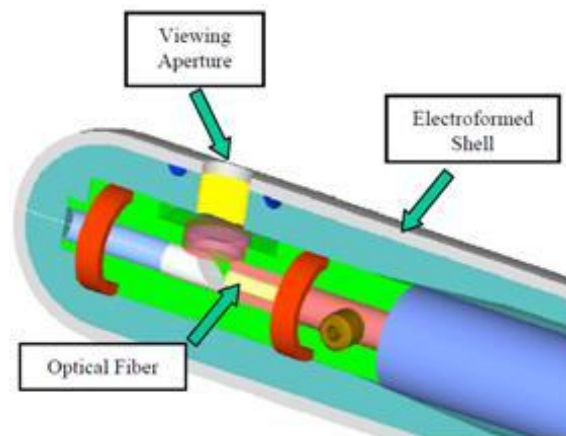


Figure 12. Schematic of optical probe concept (Suits, 2006).

Along with the probes designed for optical measurement techniques, the authors explored diagnostics and measurement methodology of turbine exhaust particulate matter and the measurement of thermodynamic properties (e.g. total pressure, static pressure, temperature). The total temperature probes consist of an inner-sheathed thermocouple with an outer radiation shield with flow discharge vents distributed around the circumference and have been successfully used in temperatures up to 2000 °C (Suits, 2006).

Water-cooled probes have also been used in areas not involving flow measurements or imaging. One such use for water-cooled probes is to simulate the formation of freeze linings on

furnace walls. In today's high temperature metallurgical processes, furnaces are water-cooled in order to protect the furnace wall from thermal, chemical, and mechanical wear. This water-cooling leads to the formation of freeze lining: a relatively stationary crust of solidified slag formed against the refractory (i.e. a furnace lining with the ability to retain its physical shape and chemical identity when subjected to high temperatures) or directly against the inside of the cooled furnace shell (Verscheure, 2006). To study freeze lining formation, a rotating crucible filled with 1.5 liters of slag was heated up to temperatures as high as 1500 °C. The water-cooled probe, shown in Figure 13, was submerged vertically into the molten slag to form a solidified layer or freeze lining.

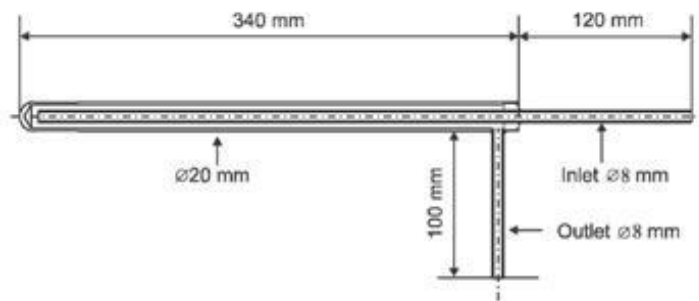


Figure 13. Design of water-cooled copper probe (Verscheure, 2006).

The probe is constructed of two coaxial copper tubes to create an annular cooling scheme. The probe measures 340 mm in length and 20 mm in outer diameter. Water enters the probe through the inner tube and exits through the outer tube (Verscheure, 2006). The furnace temperature was maintained at 1400 °C with the probe staying in the slag bath for a pre-designated period of time. After the time of submergence had been reached, the probe was removed and allowed to cool with the water running throughout the process. This cooling time allows the probe to be re-used after cleaning and the freeze lining to be analyzed and evaluated.

Conducting physical experiments allows for the development and validation of flow modeling and numerical simulation. Numerical simulations are used in order to perform

experiments with a large variety of scenarios without having to construct expensive physical models. One such numerical investigation was conducted on the flow fields inside and around a water-cooled gas-sampling probe located downstream of a gas-turbine combustor (Jiang, 2007).

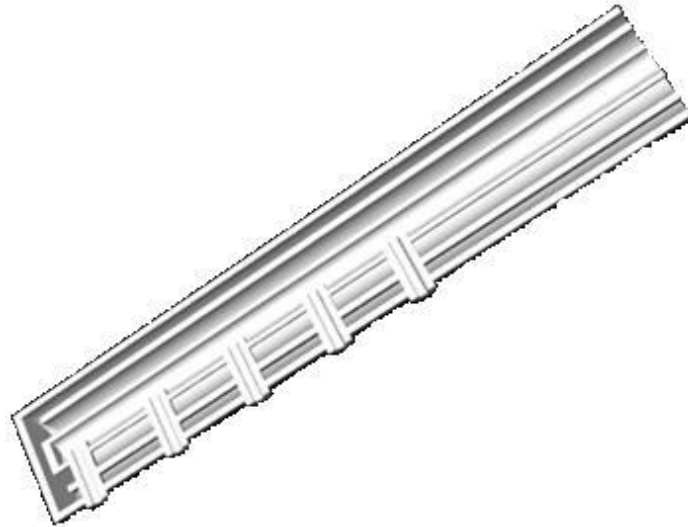


Figure 14. Section view of water-cooled gas-sampling probe (Jiang, 2007).

The gas-sampling probe, shown in Figure 14, is constructed of concentric stainless steel tubes. This configuration provides an annular cooling scheme, which has been widely used in the design and development of water-cooled probes. The probe, placed downstream of the combustor, has five sampling ports that face towards the combustor to collect flow samples. After collection, the gas sample is transported through the center tube. Water enters the probe through the inner annulus to cool the gas sample and exits through the outer annulus in order to cool the outer-most tube (Jiang, 2007). The water travels through the cooling probe at a flow rate of 4.5 kg/min and an inlet temperature of 448.15 K. At the flow outlet, a pressure of 18.83 bar was defined. Using these parameters, the complex heat transfer occurring between the flow field and probe was numerically simulated. The simulations showed that the exhaust gas flow field gradually decreased in velocity as it approached the probe, but reached a maximum velocity of 125 m/s below the upstream region of the tip, along with a relatively high velocity observed

near the top sampling port, and two counter-rotating vortices established behind the probe (Jiang, 2007). These high velocities indicate expected areas of strong convective heat transfer with the probe wall reaching a maximum temperature of 900 K. The exhaust flow transfers heat to the probe wall, which in turn transfers the same amount of heat to the cooling water, demonstrating that the temperature increase of cooling water is a key parameter for probe design and safe operation (Jiang, 2007).

Following the development and use of periscope style viewing probes, along with the successful application of electroforming, the viewing probe developed for exit-plane measurements (Hiers and Hiers, June 2002; Hiers and Hiers, July 2002; Savage, 2006) was further modified to eliminate the need for a gaseous purge flow. The purge flow was eliminated from the design by incorporating a rotating sapphire window (Beitel, 2007). The new imaging probe uses a stainless steel substructure with an electroformed nickel outer shell with an outer diameter of 13 mm. By using a rotating window, a clear surface is aligned with the aperture area during data collection for clean imaging.

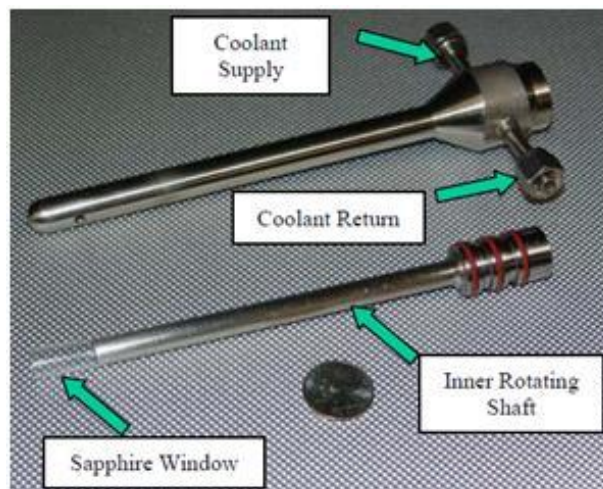


Figure 15. Photograph of prototype imaging probe components (Beitel, 2007).

Figure 15 shows a photograph with the components of the physical model which is capable of operating in conditions exceeding 2000 °C. Cooling water enters and exits the from the outer

shell at the assembly base, as well as transitioning through the inner rotating shaft via ports isolated by the o-rings (Beitel, 2007).

The methods, approaches, and information gained in the study of aircraft engines can also be applied to industrial gas-turbines, and vice versa. A concept for a water-cooled high temperature unsteady total pressure probe intended for measurements in the hot sections of gas-turbine engines (industrial and aircraft) has been presented by Brouckaert et al. (2009). The goal of this probe concept is to be able to obtain pressure measurements in a flow field reaching temperatures up to 2000 K. The probe is constructed of an Inconel 600 concentric tube assembly with an outer diameter of 8 mm and a stem length of 300 mm. The concentric tube assembly creates an annular cooling scheme for fluid entry and exit both to and from the sensor region. The sensor is cooled by creating a narrow return channel around the sensor by using a transversal concentric tube assembly with water flowing through the system at a rate of 2 liters/min (Brouckaert, 2009). This original design caused the probe tip to overheat due to a reduction in cooling caused by fluid re-circulation. This problem was fixed by modifying the probe to include a hole in the inner tube of the probe assembly to provide an increased fluid flow around the probe tip (Brouckaert, 2009). Flow trajectories of the cooling fluid may be seen and compared in Figure 16.

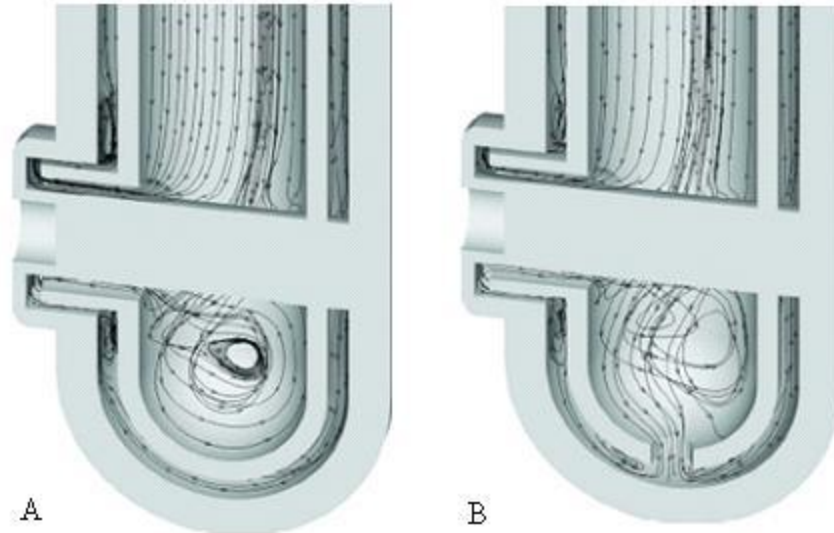


Figure 16. A) Streamtraces in original pressure design. B) Streamtraces in modified probe design (Brouckaert, 2009).

Non-intrusive optical diagnostic techniques are continually being adapted to be used in conjunction with intrusive cooled probes. One of these adaptations is the development of an endoscopic particle image velocimetry (PIV) system for use in high temperature furnaces (Rottier, 2010). The endoscope is used as an optical relay between the combustion chamber and the charged-coupled-device (CCD) camera through the refractory walls of the furnace (Rottier, 2010). The endoscope, shown in Figure 17, is 700 mm in length and 78 mm in diameter with a nitrogen flow exiting the tip to ensure thermal protection and the avoidance of particle deposit during furnace operation.

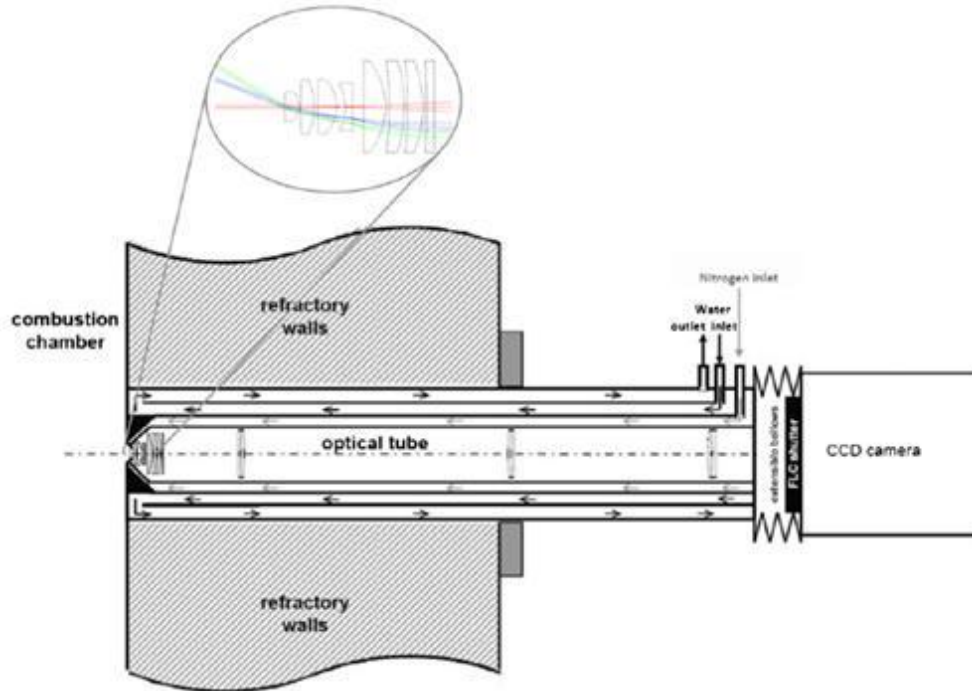


Figure 17. Schematic of high temperature endoscope equipped with CCD camera with details on incoming ray paths shown at top (Rottier, 2010).

The endoscope shown above may be used in furnace temperatures up to 1600 K and is cooled using an annular cooling scheme. Water enters the probe through the rear, travels toward the tip in the inner annulus, and travels toward the exit through the outer annulus. At the top of Figure 17, details on the incoming ray paths at a 30° collection half-angle are shown. No details were provided regarding the flow rate of the cooling fluid.

The knowledge gained on water-cooling schemes through this literature has been applied to the design, development, construction, and numerical analysis of a water-cooled probe driven by an existing sub-miniature fiber-optic LDV probe (Esirgemez and Ölçmen, 2005; Ölçmen and Daly, 2008). Details on the LDV probe and how it has driven the water-cooled probe design are provided in the next chapter.

CHAPTER 4

LASER DOPPLER VELOCIMETRY

The purpose of this chapter is to provide a brief introduction to the working principles of the LDV measurement technique so that the drive behind the creation of the water-cooling jacket may be understood. Section 4.1 provides a history and background of LDV while Section 4.2 provides a description of the LDV probe designed by Esirgemez and Ölçmen (2005).

4.1 LDV History and Background

The first presentation of laser Doppler instrumentation occurred in 1964 in which an optical configuration known as the reference-beam mode was introduced (Albrecht, 2003). The present day laser Doppler instrument currently uses a dual-beam mode which involves two incoming laser beams crossing at an intersection angle to form a measurement volume and the scattered light from both beams is collected on a single detector (Albrecht, 2003). Improvements in laser sources, optical devices, computing power, etc. have contributed to the continuous development and improvement of the laser Doppler technique. This technique uses the fringe pattern created by the interference of two crossing beams of monochromatic laser light (each with a different frequency) in the measurement volume to measure velocity of small tracer particles within the flow (Albrecht, 2003). Bragg cells are used to shift the wavelengths of laser beams in order to determine directional information of the tracer particles. Directional sensitivity is determined by the particles traveling with or against the fringes created by the laser

beams; particles traveling with the fringes result in lower frequencies while particles traveling against the fringes result in higher frequencies. The frequencies of the particles are thereby used to determine the velocity of the flow field. As these tracer particles pass through the measurement volume, light waves are scattered and subsequently collected by a receiver probe which contains a photodetector. The light collected by the photodetector is transferred to signal processing and data analysis hardware where the aforementioned frequencies are determined. Figure 18 shows a conventional laser Doppler optical arrangement.

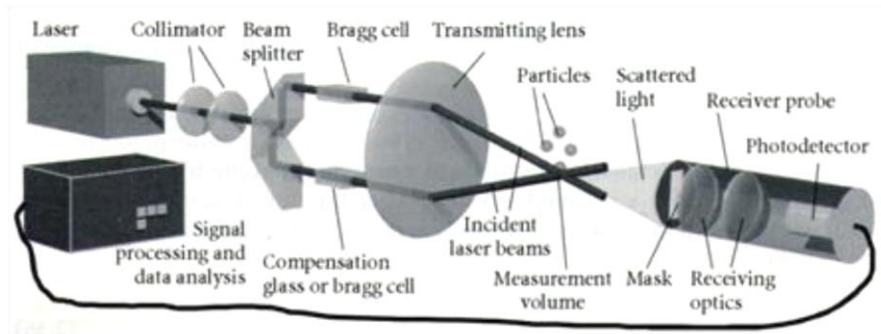


Figure 18. Dual-beam laser Doppler anemometer arrangement (Albrecht, 2003).

The frequencies obtained using the Doppler Effect may then be used to calculate the velocity of the particles in the flow. The spacing between the fringes is defined by the laser wavelength (λ) and the angle between the intersecting beams (α) in Equation 4.1 below:

$$Fringe\ spacing = \frac{\lambda/2}{\sin(\alpha/2)} \quad (4.1)$$

By measuring the passage frequency of a particle through these fringes, the particle velocity component perpendicular to the probe volume interference fringes (U) may then be expressed as:

$$U = (Fringe\ spacing) * (Frequency) \quad (4.2)$$

In a dual-beam laser Doppler arrangement, the scattered light containing the Doppler signal may be collected with the receiver in either a forward or a backward scatter mode. Figure 19 shows the difference between the light wave receiver placed in forward and backward scatter directions. The dual-beam arrangement is advantageous in that the measurement volume is uniquely defined by the intersection of the laser beams (Albrecht, 2003).

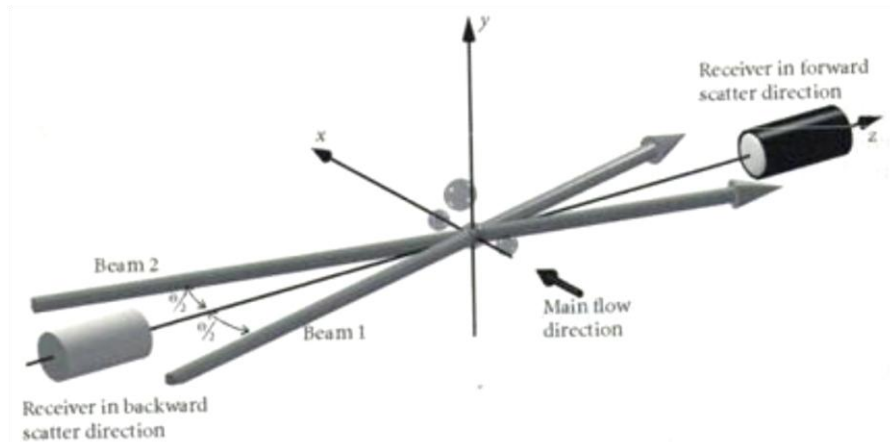


Figure 19. Dual-beam laser Doppler arrangement with forward-scatter and backscatter detection (Albrecht, 2003).

While the laser Doppler technique is vastly used in research applications throughout the world, the full use of the technique is beyond the scope of this project. Therefore, the use of the laser Doppler technique is only presented here as it applies to the design and development of a water-cooled jacket. Further explanation of the specific methods and LDV probe used is described in Section 4.2.

4.2 LDV Probe

Martin et al. (1985) made use of LDV in order to make measurements of the mean velocity and turbulence intensity during combustion in a spark ignition research engine. A modified single-cylinder research engine allowed the use of a large window in the head to permit optical access to the cylinder. A single-component non-intrusive LDV system operating in the

dual-beam mode was used. The collection optics were placed orthogonal to the incident optical axis (Martin, 1985). The data collected through these experiments have helped with the development and verification of computer simulations for optimization of engine design parameters ultimately focused toward future engine development. While these data and results are useful in assisting with the development and optimization of future engines, a more beneficial method of data collection does not include the modification of existing engines.

Instead, the data and measurement collection systems should be modified in order to minimize the need for alterations of the engine. A compact system designed to make measurements in a production-car internal combustion (IC) engine has been developed by Esirgemez and Ölçmen (2005). This two-simultaneous velocity component fiber-optic LDV probe was manufactured such that it fit into an M14 spark-plug hole (Esirgemez and Ölçmen, 2005). The LDV probe head unit houses transmitting/receiving fiber terminators and lenses to utilize the dual-beam mode in the backward scatter arrangement as shown in Figure 20, below.

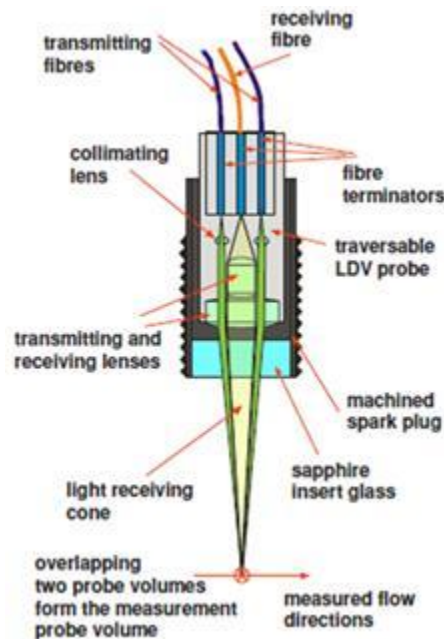


Figure 20. Schematic of spark-plug LDV probe (Esirgemez and Ölçmen, 2005).

Laser beams are emitted from the fiber terminators and through the lenses within the LDV probe which measures 30 mm in length and 13 mm in diameter at its largest point to create a measurement volume measuring $70\ \mu\text{m} \times 70\ \mu\text{m} \times 1337\ \mu\text{m}$. The light reflected by the traveling particles is focused onto the receiving fiber terminator after passing through two lenses (Esirgemez and Ölçmen, 2005) and then travels through fiber-optic cables into a photo-multiplier tube. The photo-multiplier tube converts the light information into an electrical signal where it proceeds to the signal processing and data analysis hardware. This LDV probe was used to make velocity measurements in a 1997 Honda Civic LX car engine under idling conditions after undergoing tests in a free round-jet flow generated by a gas probe calibrator (Esirgemez and Ölçmen, 2005). The engine cylinder in which the probe was taking measurements did not have any combustion taking place because the spark plug hole was needed for the modified M14 spark plug to gain optical access with the LDV system. Three-view schematic drawings of the LDV probe may be found in Appendix A.

The methods and information gained in the development of the two-component LDV probe helped lead to the development of a three-component LDV probe used by Ivanchenko et al. (2007). The three-component LDV probe uses a combination of the conventional dual-beam laser Doppler technique for two of the directional components and a heterodyne technique for the third component. The heterodyne technique uses one laser beam as a reference beam which can be mixed with a scattered wave. The two waves are mixed on the detector surface which yields the difference frequency (Albrecht, 2003). The water-cooling jacket designed and discussed in this thesis is driven by the dimensions and functionality of the two-component LDV probe used by Esirgemez and Ölçmen (2005). The details of the design of the water-cooled probe are provided in the following chapter.

CHAPTER 5

WATER-COOLED PROBE: DESIGN AND SIMULATION CONFIGURATIONS

The purpose of this chapter is to provide a description of the design process and functionality of the water-cooled LDV probe. Section 5.1 provides details on the LDV probe design and layout. The method of determining the flow rate of water through the cooling probe is discussed in Section 5.2. Section 5.3 describes the governing equations of FloWorks and the setup of the numerical simulation used to evaluate the complex heat transfer occurring between the water-cooled probe and the extreme environment of the flow within a jet engine augmentor.

5.1 Water-Cooled LDV Probe Design

A three-dimensional parametric modeling program, SolidWorks, was used to design the water-cooled LDV probe (jacket). Based on the designs of previous water-cooled probes, an annular cooling method was sought after in order to obtain efficient cooling. Due to size restrictions and the desire to reduce the maximum overall diameter of the probe, however, the cooling method had to be modified to be pseudo-annular. The primary portion of the jacket design consists of two stainless steel concentric tubes (inner tube and outer tube) with fins between them to divide the flow. The inner tube, with an ID of 13.39 mm and an OD of 15.88 mm, is used to house the LDV probe discussed in Section 4.2. Flow dividing fins are mounted to the exterior of this inner tube to allow the separation of the incoming cool water traveling toward the probe tip and the outgoing heated water traveling away from the probe tip. The dividing fins

continue along the length of the inner tube and stop 19.05 mm away from the inside surface of the jacket tip. An outer tube, with an ID of 18.92 mm and an OD of 22.23 mm, is placed and mounted around the inner tube and flow dividing fins to create a fluid flow channel with a width of 1.52 mm. The probe tip is capped using a stainless steel disc welded to both the inner tube and the outer tube. A counter bored hole was drilled into the disc to allow optical access. A sapphire window may be placed into this optical access hole and held in place using a retaining ring. A reservoir tank is located at the rear end of the jacket to provide entry and exit ports for the cooling water. This reservoir tank contains flow dividing fins which are aligned with the dividing fins between the inner and outer tubes in order to separate the incoming cool water and the outgoing heated water traveling through the probe channel. Water is supplied into the reservoir tank through a pressure washer attached using a high pressure stainless steel quarter-inch male plug. A second high pressure male plug is attached to the lid of the reservoir tank for the water to exit through. The plugs are placed in the tank lid symmetrically so as to not limit the cooling jacket water supply and exit arrangement. The model of the jacket was simplified from the physical design for the numerical simulations. A cutaway view showing the jacket inserted into the augmentor section may be seen below in Figure 21. Figure 22 shows a magnified view of the jacket tip to provide added detail.

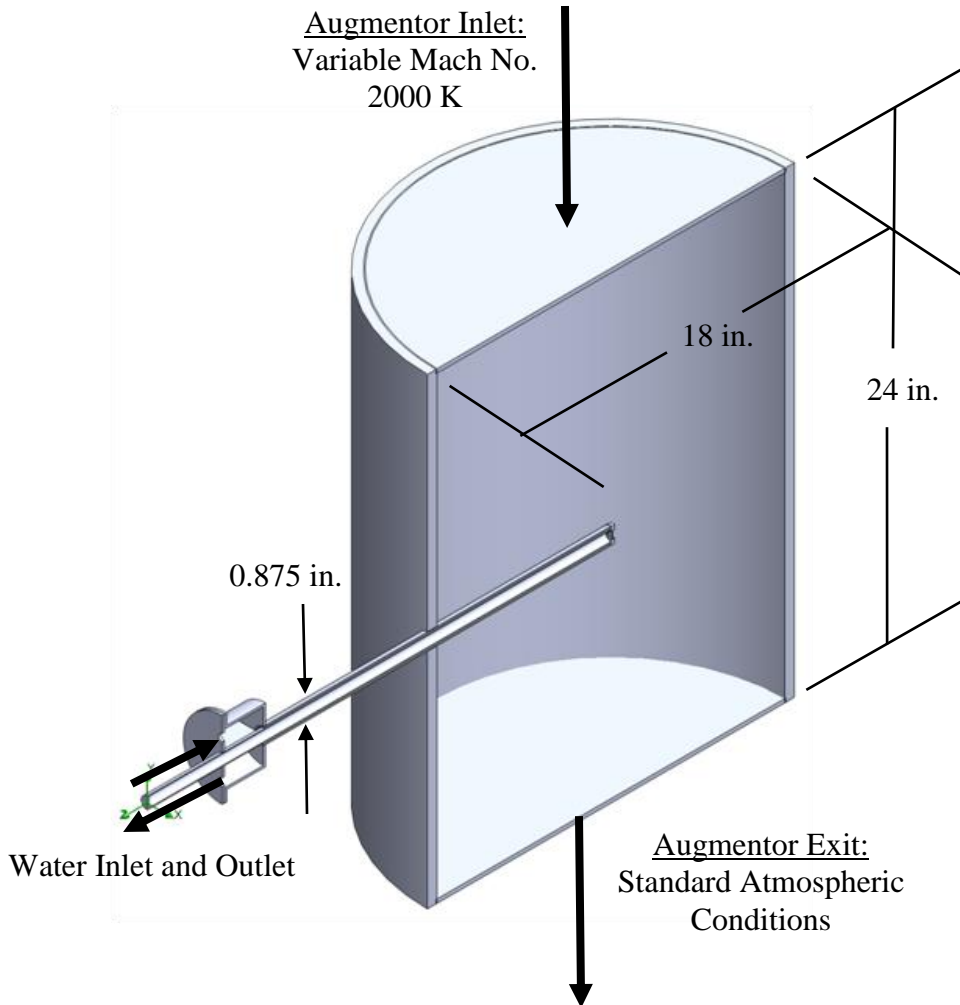


Figure 21. Cutaway view of jacket inserted into augmentor section.

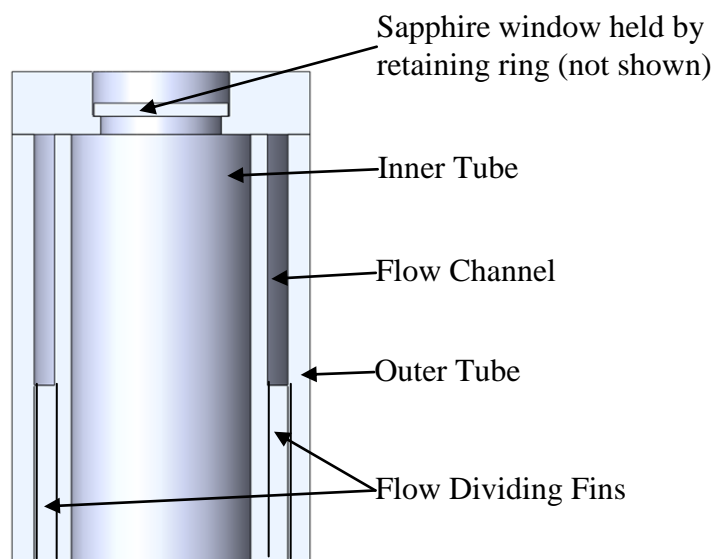


Figure 22. Cutaway section view of jacket tip made with SolidWorks.

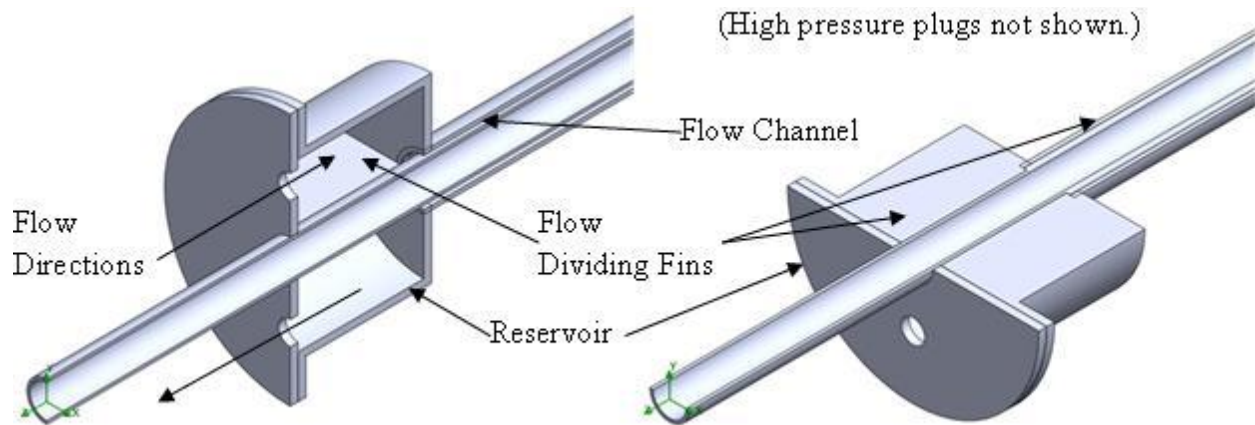


Figure 23. SolidWorks schematic of cooling jacket.

Figure 23 contains cutaway sections of the model reservoir tank to show the previously discussed features of the water-cooling jacket. Some features not shown in Figure 23 include the high pressure quarter-inch stainless steel male plugs and a hollowed out stainless steel compression fitting used to seal the hole in the lid through which the inner tube passes. The high pressure plugs and compression fitting not shown in the simplified model may be seen in the photograph of the physical model in Figure 24 in Section 5.2. Additional information regarding the dimensions of the physical model of the water-cooled jacket is shown in the three-view schematic drawings in Appendix B.

5.2 Experimental Evaluation of Flow Rate through Probe

Before the numerical simulations could be conducted, the volumetric flow rate of the cooling water through the jacket needed to be known. In order to determine the flow rate, a physical model of the cooling jacket was fabricated in The University of Alabama's College of Engineering Machine Shop. The jacket may be seen in Figure 24, below, both by itself and connected to an off-the-shelf pressure washer (Husky-HU80911A) designed to operate at a pressure of 2600 psi with a flow rate of 2.4 GPM using one of the included nozzles. Pressure washer specifications may be found in Appendix C.



Figure 24. A) Photograph of cooling jacket. B) Photograph of cooling jacket with pressure washer wand and hose attached.

Figure 24 B shows the cooling jacket mounted to an elevated brace. The pressure washer wand is connected to one of the high pressure male plugs for water supply while a hose is attached with a worm clamp to the second plug in order to direct the exiting water away from the experimental setup. In determining the flow rate through the jacket, the end of the hose was inserted into a five-gallon bucket with an intermediate four gallon marking on the exterior. This four gallon mark and the five gallon capacity (full to the brim) were used to determine the flow rate of the water through the jacket. The pressure washer was run for several seconds prior to inserting the hose into the bucket to allow the internal water pump to clear any air that may have been in the line. Upon inserting the hose into the bucket, a stopwatch—accurate to 1/100 of a second—was simultaneously started. The stopwatch was stopped when the water in the bucket reached both the four and five gallon marks. The times to reach each volume mark were recorded ten times. These times were then used to determine a volumetric flow rate for each test. The flow rates for each mark (four and five gallons) were calculated and averaged separately. Once the averages of the flow rates were calculated, an overall average of the volumetric flow rate was calculated and determined to be approximately 3 GPM. Based on these tests, a flow

rate of 3 GPM was then used in the numerical simulation of the probe inserted into the extreme environment of the jet engine augmentor flow field. The details of the numerical simulations are discussed in the next section.

5.3 Numerical Simulation Setup

The simplified model, drawn in SolidWorks, was used to compute the complex heat transfer occurring throughout the system along with the effects of the probe on the flow field in an afterburner/augmentor section with a diameter of 18 inches. The augmentor diameter was chosen to be 18 inches for the present research simulations because a modified GE J-85 jet engine with an 18 in. augmentor diameter used for experimental research purposes is held and used at the Arnold Engineering Development Center (AEDC). The numerical simulations were completed using the SolidWorks CFD software package add-in, FloWorks.

5.3.1 FloWorks Governing Equations

FloWorks is capable of solving both laminar and turbulent flows using the Navier-Stokes equations supplemented by fluid state equations to define the nature of the fluid and empirical dependencies of fluid density, viscosity, and thermal conductivity on temperature (COSMOS, 2008). The primary reason for the development of FloWorks was for the simulation and study of turbulent flows. The prediction of these turbulent flows is possible using the Favre-averaged Navier-Stokes equations, where time-averaged effects of flow turbulence on the flow parameters are considered and other large-scale, time-dependent phenomena are taken into account directly. This procedure introduces new terms in the equations known as Reynolds stresses which require additional information. FloWorks employs transport equations for the turbulent kinetic energy and its dissipation rate in the form of the k - ϵ model to close the system of equations. This

system of equations is used to describe both laminar and turbulent flow and allows for the possibility of transition from a laminar to turbulent state and/or vice versa (COSMOS, 2008).

The conservation laws for mass, angular momentum and energy in the Cartesian coordinate system rotating with angular velocity Ω about an axis passing through the origin of the coordinate system may be written in the following form:

$$\frac{\partial \rho}{\partial t} + \frac{\partial}{\partial x_i} (\rho u_i) = 0 \quad (5.1)$$

$$\frac{\partial \rho u_i}{\partial t} + \frac{\partial}{\partial x_j} (\rho u_i u_j) + \frac{\partial p}{\partial x_i} = \frac{\partial}{\partial x_j} (\tau_{ij} + \tau_{ij}^R) + S_i \quad i = 1,2,3 \quad (5.2)$$

$$\frac{\partial \rho H}{\partial t} + \frac{\partial \rho u_i}{\partial x_i} = \frac{\partial}{\partial x_i} (u_j (\tau_{ij} + \tau_{ij}^R) + q_i) + \frac{\partial p}{\partial t} - \tau_{ij}^R \frac{\partial u_i}{\partial x_j} + \rho \varepsilon + S_i u_i + Q_H, \quad (5.3)$$

$$H = h + \frac{u^2}{2},$$

where u is the fluid velocity, ρ is the fluid density, S_i is a mass-distributed external force per unit mass due to a porous media resistance ($S_{i,porous}$), a buoyancy ($S_{i,gravity} = -\rho g_i$, where g_i is the gravitational acceleration component along the i -th coordinate direction), and the rotation of the coordinate system ($S_{i,rotation}$), i.e., $S_i = S_{i,porous} + S_{i,gravity} + S_{i,rotation}$, h is thermal enthalpy, Q_H is a heat source or sink per unit volume, τ_{ij} is the viscous shear stress tensor, and q_i is the diffusive heat flux. The subscripts are used to denote summation over the three coordinate directions.

When conducting a CFD analysis in which the ‘‘High Mach number flow’’ option is enabled, the energy equation may be re-written as follows:

$$\frac{\partial \rho E}{\partial t} + \frac{\partial \rho u_i \left(E + \frac{p}{\rho} \right)}{\partial x_i} = \frac{\partial}{\partial x_i} \left(u_j (\tau_{ij} + \tau_{ij}^R) + q_i \right) - \tau_{ij}^R \frac{\partial u_i}{\partial x_j} + \rho \varepsilon + S_i u_i + Q_H, \quad (5.4)$$

$$E = e + \frac{u^2}{2},$$

where e is the internal energy. The viscous shear stress tensor may be defined as follows for Newtonian fluids:

$$\tau_{ij} = \mu \left(\frac{\partial u_i}{\partial x_j} + \frac{\partial u_j}{\partial x_i} - \frac{2}{3} \delta_{ij} \frac{\partial u_k}{\partial x_k} \right) \quad (5.5)$$

The Reynolds-stress tensor takes on the following form after the Boussinesq assumption:

$$\tau_{ij}^R = \mu_t \left(\frac{\partial u_i}{\partial x_j} + \frac{\partial u_j}{\partial x_i} - \frac{2}{3} \delta_{ij} \frac{\partial u_k}{\partial x_k} \right) - \frac{2}{3} \rho k \delta_{ij} \quad (5.6)$$

Here, δ_{ij} is the Kronecker delta function (equal to unity when $i=j$, and zero otherwise), μ is the dynamic viscosity coefficient, μ_t is the turbulent eddy viscosity coefficient, and k is the turbulent kinetic energy. Both the turbulent eddy viscosity and the turbulent kinetic energy are zero for laminar flows. The turbulent kinetic energy (k) and the turbulent dissipation rate (ε) are two turbulence properties used to define μ_t in the frame of the k - ε turbulence model.

$$\mu_t = f_\mu \frac{C_\mu \rho k^2}{\varepsilon} \quad (5.7)$$

where f_μ is a turbulent viscosity factor defined by the following expression:

$$f_\mu = [1 - \exp(-0.025R_y)]^2 \cdot \left(1 + \frac{20.5}{R_T}\right), \quad (5.8)$$

$$\text{where } R_T = \frac{\rho k^2}{\mu \varepsilon}, \quad R_y = \frac{\rho \sqrt{k} y}{\mu}$$

and y is the distance from the wall. This function allows for the laminar-turbulent transitions to be taken into account. The turbulent kinetic energy and dissipation rate are described using two additional transport equations,

$$\frac{\partial \rho k}{\partial t} + \frac{\partial}{\partial x_i} (\rho u_i k) = \frac{\partial}{\partial x_i} \left(\left(\mu + \frac{\mu_t}{\sigma_k} \right) \frac{\partial k}{\partial x_i} \right) + S_k, \quad (5.9)$$

$$\frac{\partial \rho \varepsilon}{\partial t} + \frac{\partial}{\partial x_i} (\rho u_i \varepsilon) = \frac{\partial}{\partial x_i} \left(\left(\mu + \frac{\mu_t}{\sigma_\varepsilon} \right) \frac{\partial \varepsilon}{\partial x_i} \right) + S_\varepsilon, \quad (5.10)$$

in which the source terms S_k and S_ε are defined below.

$$S_k = \tau_{ij}^R \frac{\partial u_i}{\partial x_j} - \rho \varepsilon + \mu_t P_B \quad (5.11)$$

$$S_\varepsilon = C_{\varepsilon 1} \frac{\varepsilon}{k} \left(f_1 \tau_{ij}^R \frac{\partial u_i}{\partial x_j} + \mu_t C_B P_B \right) - C_{\varepsilon 2} f_2 \frac{\rho \varepsilon^2}{k} \quad (5.12)$$

Here, P_B represents the turbulence generation due to buoyancy forces and can be written as

$$P_B = - \frac{g_i}{\sigma_B} \frac{1}{\rho} \frac{\partial \rho}{\partial x_i} \quad (5.13)$$

where the constant $\sigma_B = 0.9$, C_B is a constant defined as: $C_B = 1$ when $P_B > 0$, and 0 otherwise;

$$f_1 = 1 + \left(\frac{0.05}{f_\mu}\right)^3, \quad f_2 = 1 - \exp(-R_T^2) \quad (5.14)$$

The constants C_μ , $C_{\varepsilon 1}$, $C_{\varepsilon 2}$, σ_k , and σ_ε are defined empirically with the following values:

$$C_\mu = 0.09, \quad C_{\varepsilon 1} = 1.44, \quad C_{\varepsilon 2} = 1.92, \quad \sigma_k = 1, \quad \sigma_\varepsilon = 1.3 \quad (5.15)$$

When the Lewis number (Le) is equal to one, the diffusive heat flux is defined in the following form:

$$q_i = \left(\frac{\mu}{Pr} + \frac{\mu_t}{\sigma_c}\right) \frac{\partial h}{\partial x_i}, \quad i = 1, 2, 3 \quad (5.16)$$

Here, the constant $\sigma_c = 0.9$ and Pr is the Prandtl number. The equations just discussed are used to describe laminar flows, turbulent flows, and the transitions between these flow types within the CFD add-in FloWorks.

The Modified Wall Functions approach model is used to characterize both laminar and turbulent flows in regions near walls as well as to describe the laminar/turbulent flow transitions. If the size of a mesh cell near a wall is greater than the boundary layer thickness, the integral boundary layer method is used. This model is used to provide accurate velocity and temperature boundary conditions for the aforementioned conservation equations (COSMOS, 2008).

The system of Navier-Stokes equations is supplemented by definitions of thermophysical properties and state equations for the fluids. FloWorks provides simulations of gas and liquid flows with density, viscosity, thermal conductivity, specific heats, and species diffusivities as functions of pressure, temperature and species concentrations in fluid mixtures. Along with these simulations, equilibrium volume condensation of water from steam can be taken into

account when simulating steam flows (COSMOS, 2008). Generally, the state equation of a fluid has the following form:

$$\rho = f(p, T, Y) \quad (5.17)$$

where $Y = (Y_1, \dots, Y_M)$ is the concentration vector of the fluid mixture components. With the exception of some special cases, gases are considered to be ideal and have the state equation with the following form:

$$\rho = \frac{P}{RT} \quad (5.18)$$

where R is the gas constant which is equal to the universal gas constant (R_{univ}) divided by the fluid molecular mass (M), or, for the mixtures of ideal gases,

$$R = R_{univ} \sum_m \frac{Y_m}{M_m} \quad (5.19)$$

where Y_m , $m = 1, 2, \dots, M$, are the mixture component concentrations, and M_m is the molecular mass of the m -th component.

With the exception of special cases (i.e. compressible liquids and non-Newtonian liquids), liquids are considered to be incompressible where the density of an individual liquid is determined solely on temperature:

$$\rho = f(T) \quad (5.20)$$

and the state equation for a mixture of liquids is defined as

$$\rho = \left(\sum_m \frac{Y_m}{\rho_m} \right)^{-1} \quad (5.21)$$

The specific heat and thermophysical properties of the liquid (i.e. viscosity and thermal conductivity) are specified as functions of temperature. Additional information regarding the special cases such as real gases and compressible liquids may be found within the reference (COSMOS, 2008).

5.3.2 Mesh Settings

In order to solve the governing equations previously discussed, the model designed in SolidWorks must have a mesh applied to it. FloWorks automatically generates a rectangular computational mesh to distinguish fluid and solid domains or regions. The computational domain generated encloses the model and is divided into uniform rectangular parallelepiped-shaped cells to form the basic mesh. From here, the mesh may be refined (i.e. split into smaller parallelepiped-shaped cells) using the model geometry to better represent the model and fluid regions (COSMOS, 2008). More information on the refinement process may be found within the reference (COSMOS, 2008).

The mesh grid may be generated with a varying number of cells based on a mesh refinement level slider ranging from one to eight. Level eight represents the highest mesh refinement level created by the automatic mesh generation system. The accuracy of the results and the computation run time increase with the increased mesh refinement level. A lateral view of the jacket inserted into the augmentor with the basic mesh applied at a mesh setting of 6 may be seen in Figure 25.

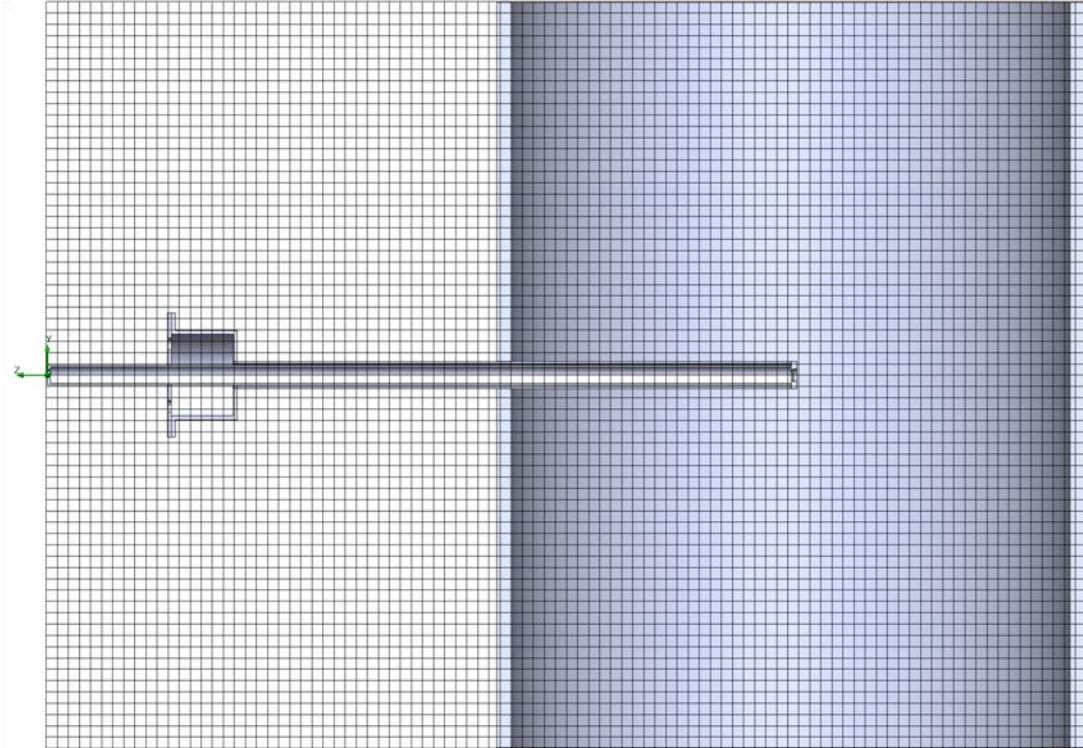


Figure 25. Lateral view of jacket inserted into augmentor with basic mesh applied at a mesh setting of 6.

In order to determine which mesh level would be needed to obtain accurate results and minimal computation time, different mesh settings were employed on a single probe configuration. In this configuration, the probe is inserted a distance equal to 50% of the augmentor diameter. More information on the other probe configurations and insertion distances may be found in Section 5.3.3. A lateral view of the jacket inserted into the augmentor with the refined mesh applied at a mesh setting of 6 may be seen in Figure 26. A magnified view of the jacket tip with the refined mesh applied may be seen in Figure 27.

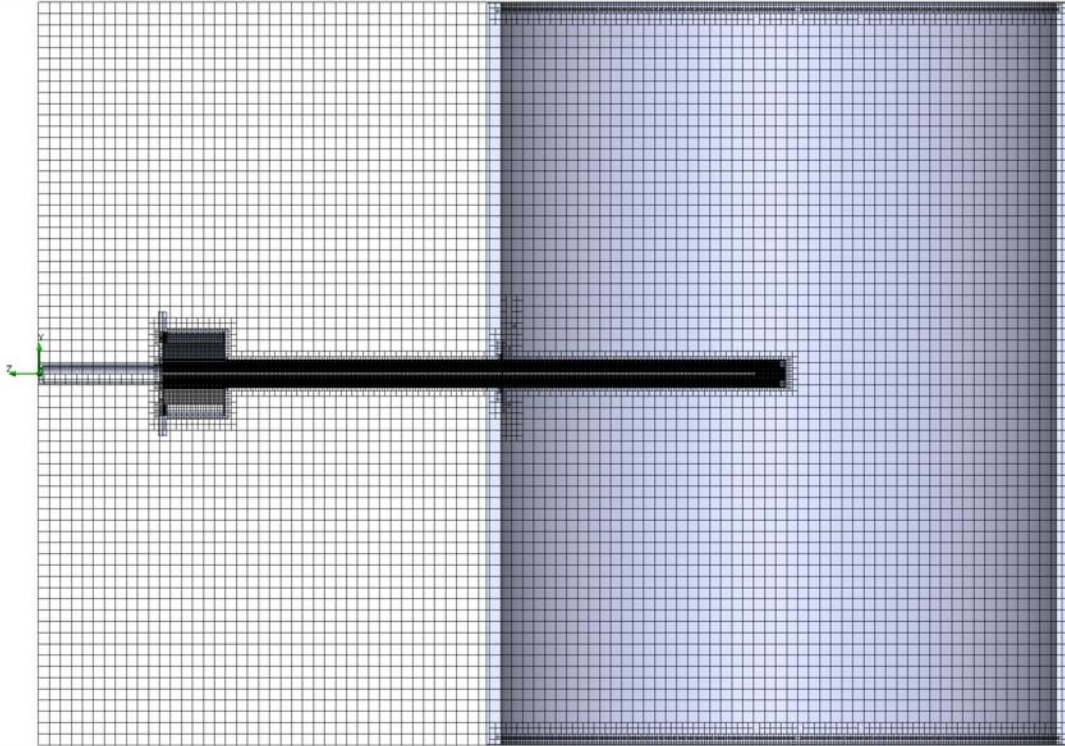


Figure 26. Lateral view of jacket inserted into augmentor with refined mesh applied at a mesh setting of 6.

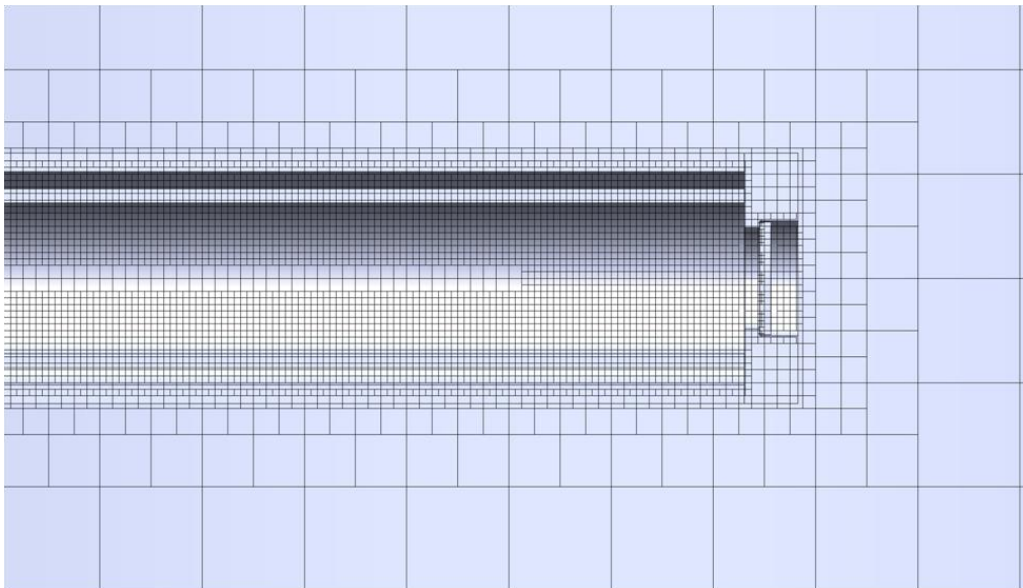


Figure 27. Magnified view of jacket tip with refined mesh applied at a mesh setting of 6.

Mesh settings of 4, 5, 6, and 7 were used in the comparison along a selected water flow path.

This comparison may be seen in Figure 28, below, where the water temperature is plotted against the distance traveled through the probe from channel inlet to channel outlet. The areas of flow

are marked as incoming, outgoing, and flow through pathway (where the water reaches the probe tip and begins to exit). A magnification of the length range from 0.45 m to 0.55 m is shown in Figure 29.

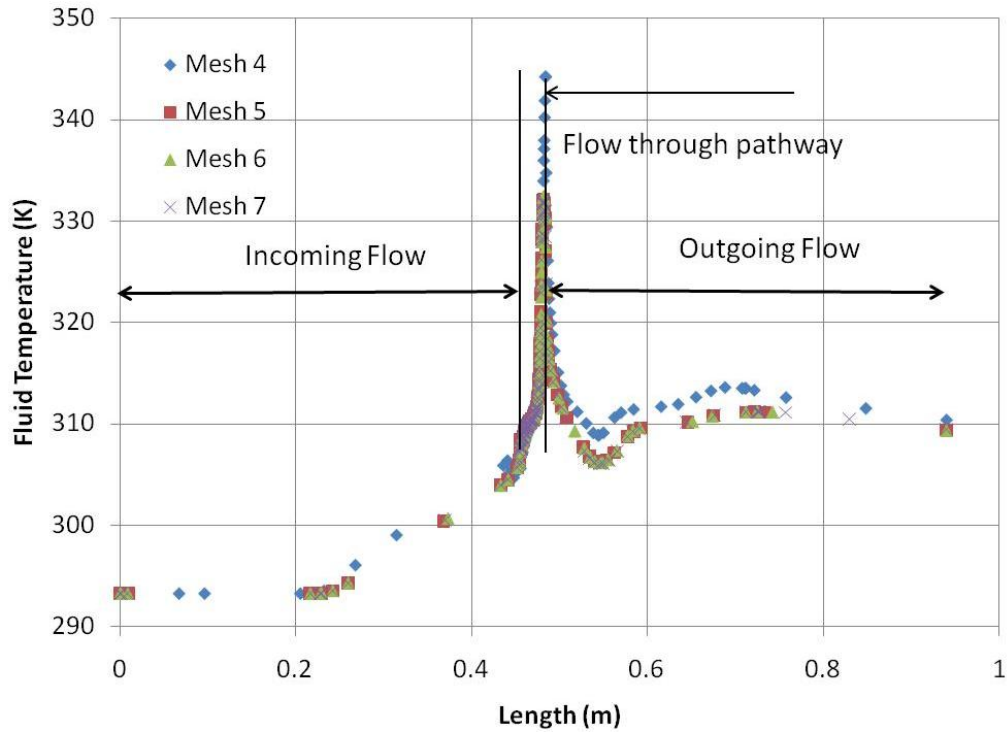


Figure 28. Comparison of grid mesh setting for insertion distance equal to 50% of augmentor diameter along flow path length.

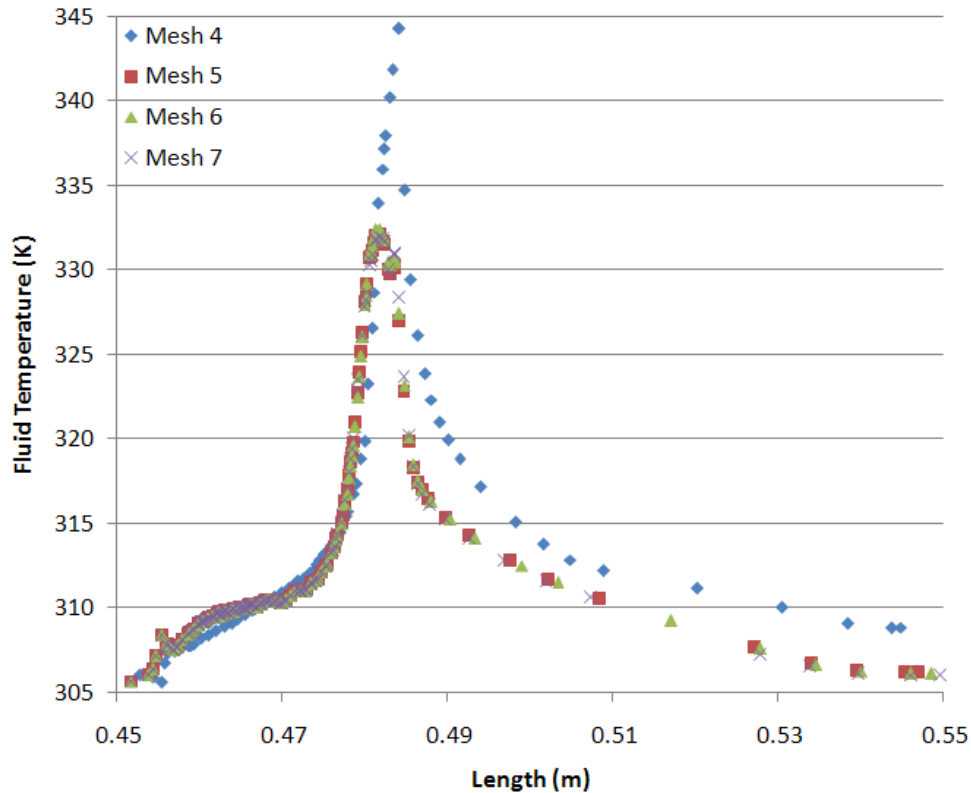


Figure 29. Magnification of comparison of grid mesh setting for insertion distance equal to 50% of augmentor diameter from 0.45 m to 0.55 m flow path length.

From this comparison, it may be seen that results for the temperature of the fluid are all approximately equal for mesh settings of 5, 6, and 7. A mesh setting of 6, which resulted in approximately one million cells for this particular configuration, was selected for use in the CFD calculations of all probe configurations because it was seen to optimize calculation accuracy and total computation time.

5.3.3 Probe Configurations

The different probe configurations simulated and analyzed are based on three different criteria: 1.) the distance the probes are inserted into the augmentor section; 2.) the type of probe tip used (flat or hemispherical) and; 3.) the Mach number of the augmentor inlet flow. Some of the configurations were computed without cooling liquid flowing in order to simulate pressure washer failure or a “worst case scenario”. The insertion distances of the probes into the

augmentor section are determined as a percentage of the 18 in. internal diameter of the augmentor, which has a length of two feet. The inner face of the jacket tip coincides with the point at which the LDV laser probe stops inside the water-cooled jacket and is used as the reference face for measuring the insertion distance. An image of a probe configuration with a flat tip inserted 50% of the augmentor diameter may be seen in Figure 30, below. The line in the image marks the center of the augmentor section and is also lined up with the jacket tip inner face. Table 1, below, lists the test matrix for the different configuration combinations computed and analyzed in this research.

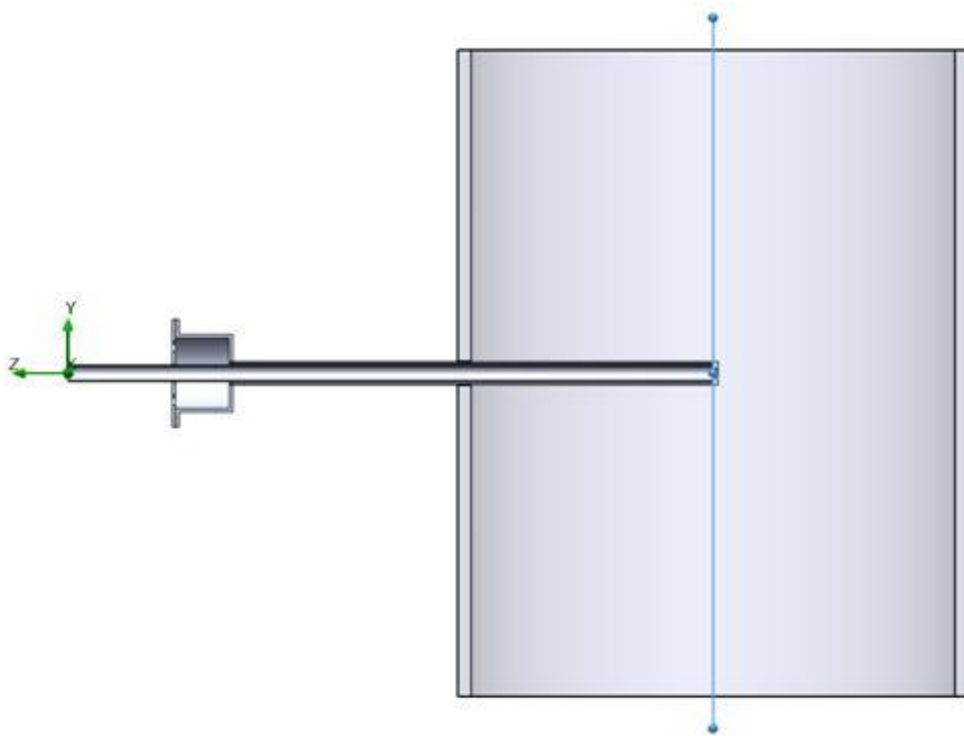


Figure 30. Image of probe configuration with flat tip inserted 50% of augmentor diameter.

Table 1. FloWorks Simulation Test Matrix

Configuration	Insertion Percentage	Mesh Setting	Augmentor Inlet Mach Number	Tip	Flow Rate (GPM)
1	50	4	0.7	Flat	3
2	50	5	0.7	Flat	3
3	50	6	0.7	Flat	3
4	50	7	0.7	Flat	3
5	50	6	0.5	Flat	3
6	50	6	0.3	Flat	3
7	50	6	0.1	Flat	3
8	50	6	0.7	Flat	0
9	50	6	0.7	Hem.	3
10	50	6	0.5	Hem.	3
11	50	6	0.3	Hem.	3
12	50	6	0.1	Hem.	3
13	75	6	0.7	Flat	3
14	75	6	0.7	Flat	0
15	88.9	6	0.7	Flat	3
16	88.9	6	0.7	Flat	0

The flat jacket tips were analyzed at all insertion distances while the hemispherical tips were only analyzed for the insertion distance of 50%. Based on the results of the analyses, which will be discussed in the next chapter, the augmentor inlet velocity needed to be reduced in order to determine the combination of the jacket tip and augmentor inlet Mach number at which the flow field disruption is minimal.

5.3.4 Initial and Boundary Conditions for Numerical Simulations

The numerical simulations of the various probe configurations require that initial and boundary conditions match the conditions that exist in the experimental setup. These conditions include the flow rate of water traveling through the probe, the atmospheric conditions at the probe exit, the augmentor inlet flow field Mach number, and the atmospheric conditions at the augmentor exit. It is also important to define the areas or subdomains of the model geometry

that contain water as the fluid and those that have air as the fluid. The simulation conditions may be seen in Table 2, below.

Table 2. FloWorks Boundary Conditions

Fluid	Location	Condition Type	Value	Units
Air	Augmentor Inlet	Mach Number	See Table 1	--
	Augmentor Inlet	Temperature	2000	K
	Augmentor Exit	Pressure	1	atm
	Augmentor Exit	Ambient Temperature	293.2	K
	Augmentor Zone	Kinetic Energy	1	J/kg
	Augmentor Zone	Energy Dissipation Rate	1	W/kg
Water	Probe Inlet	Flow Rate	See Table 1	GPM
	Probe Inlet	Temperature	293.2	K
	Probe Exit	Pressure	1	atm
	Probe Exit	Temperature	293.2	K
	Probe Zone	Kinetic Energy	1	J/kg
	Probe Zone	Energy Dissipation Rate	1	W/kg

These boundary and initial conditions were input into the FloWorks interface using standard control options within the program. All conditions were input into the software to simulate, as closely as possible, the actual conditions expected to be observed in experimental analysis. The turbulence parameters (i.e. kinetic energy and kinetic energy dissipation rate) were used at the default settings (seen in Table 2) because there is not currently any experimentally obtained information in this study to provide details on the turbulence parameters. The results obtained from the numerical simulations are presented in the next chapter.

CHAPTER 6

SIMULATION RESULTS AND DISCUSSION

The purpose of this chapter is to show and discuss the results obtained from the numerical simulations completed using the SolidWorks CFD add-in, FloWorks. The results presented here show the temperature and velocity distributions throughout the augmentor flow field (Section 6.1), the temperature distribution at the tip of the jacket for different configurations (Section 6.2), and the temperature distribution at a variety of cut planes along the probe for different jacket configurations (Section 6.3).

6.1 Effects of Water-Cooled Probe on Flow Field

The effectiveness of the LDV probe inserted into the augmentor is dependent on the water-cooled jacket affecting the augmentor flow field as little as possible. In order to determine the combination of design parameters and flow regimes where the jacket may be effectively used, a variety of numerical simulations were completed. For this purpose, the effects of the insertion distance (Section 6.1.1), augmentor inlet Mach number (Section 6.1.2), and water-cooled jacket tip design (Section 6.1.3) on the flow field were analyzed.

6.1.1 Effects of Jacket Insertion Distance on Augmentor Flow Field

In order to determine the effects of the insertion distance on the velocity and temperature distributions of the augmentor flow field, calculations were made with the jacket inserted distances equal to 50%, 75%, and 88.9% of the augmentor diameter. These insertion distance percentages were used to allow for clearance of the 60 mm focal length of the laser beams emitted from the LDV probe so that the beams focus within the flow. Flow field plots of velocity and temperature distributions at lateral and axial symmetry planes are shown in this section. The axial symmetry planes are located at half the distance between the inner face of the probe and the augmentor wall for each insertion distance. Results for the velocity distributions for the jacket inserted into the Mach 0.7 flow field at distances equal to 50%, 75%, and 88.9% of the augmentor diameter are shown in Figure 31, Figure 32, and Figure 33, respectively. The 60 mm laser beam focal point is approximated by a black dot in the figures below.

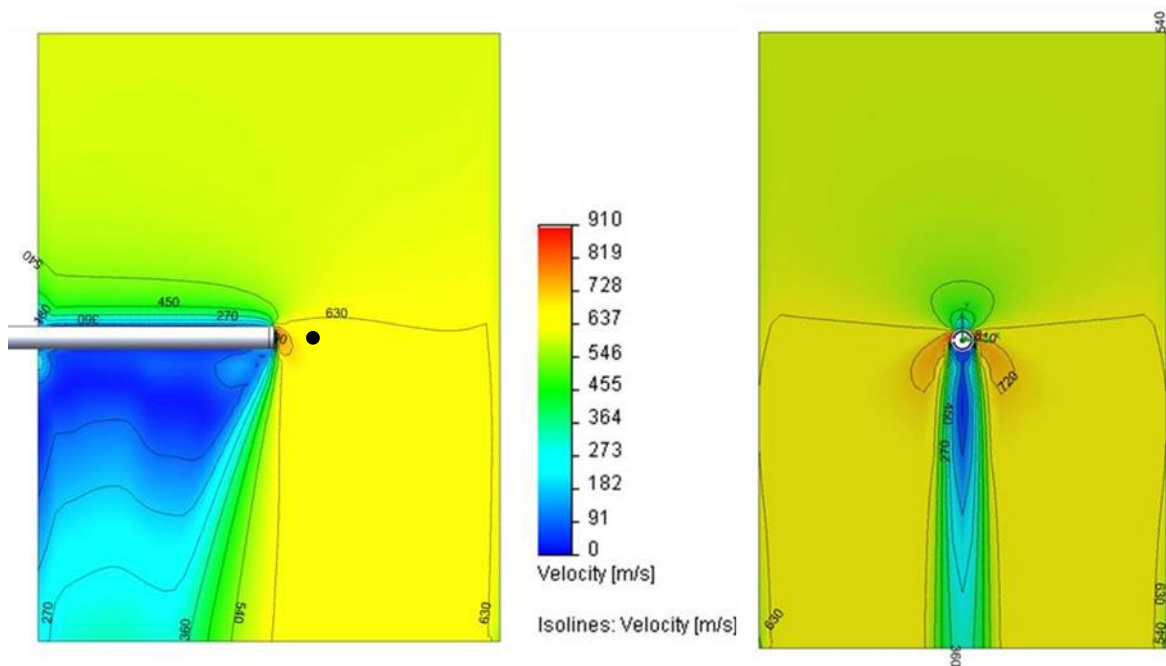


Figure 31. Velocity distribution for Mach 0.7 augmentor flow with flat tip probe insertion of 50%: lateral view (left) and axial view (right).

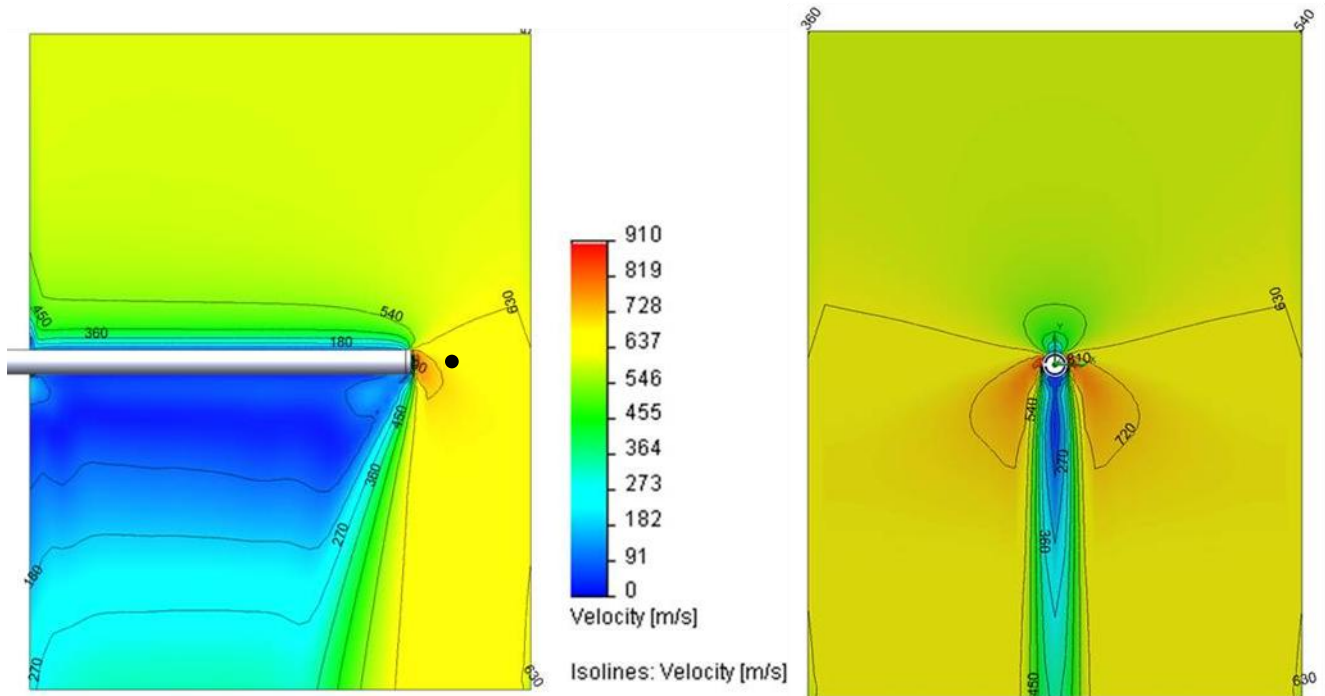


Figure 32. Velocity distribution for Mach 0.7 augmentor flow with flat tip probe insertion of 75%: lateral view (left) and axial view (right).

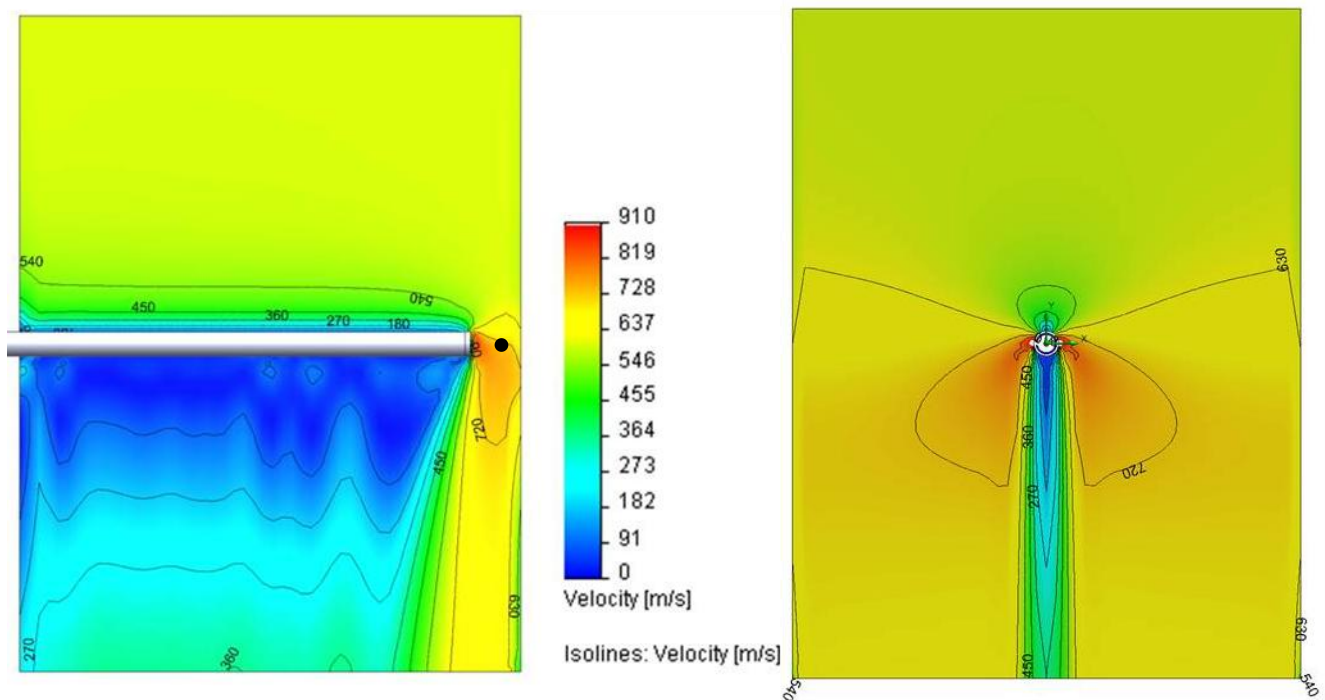


Figure 33. Velocity distribution for Mach 0.7 augmentor flow with flat tip probe insertion of 88.9%: lateral view (left) and axial view (right).

The figures with the velocity distributions show that the probe affects the augmentor flow field by varying quantities based on the distance in which the probe is inserted. As the probe is inserted further into the augmentor, the flow field is more greatly affected and disturbed. The flow field velocity is least affected when the water-cooled jacket is inserted 50% of the augmentor diameter. It may be seen in each of these figures that the flow field velocity in the LDV probe laser beam focal point region increases to become greater than the freestream velocity for each insertion distance case. The highest velocity is consistently found to be in the range of 850-900 m/s immediately in front of the jacket tip when the augmentor is operating at Mach 0.7. It may also be seen that as the jacket is inserted further into the augmentor, the disturbance in the wake velocity grows larger. Temperature distribution cut plots of the flow fields at Mach 0.7 with jacket insertion distances of 50%, 75%, and 88.9% may be seen in Figure 34, Figure 35, and Figure 36, respectively.

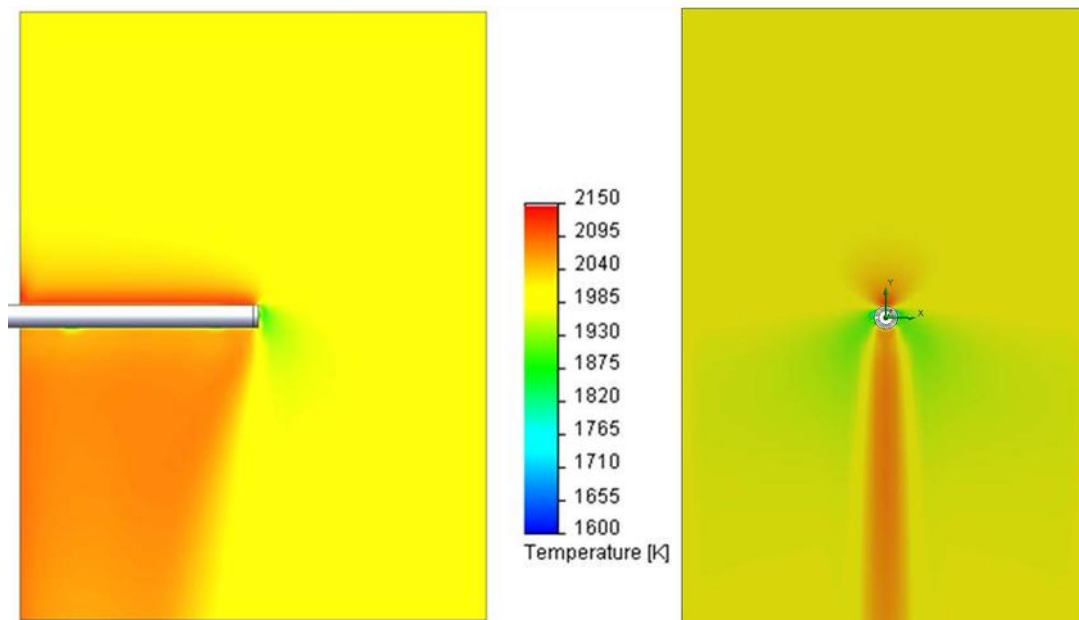


Figure 34. Temperature distribution for Mach 0.7 augmentor flow with flat tip probe insertion of 50%: lateral view (left) and axial view (right).

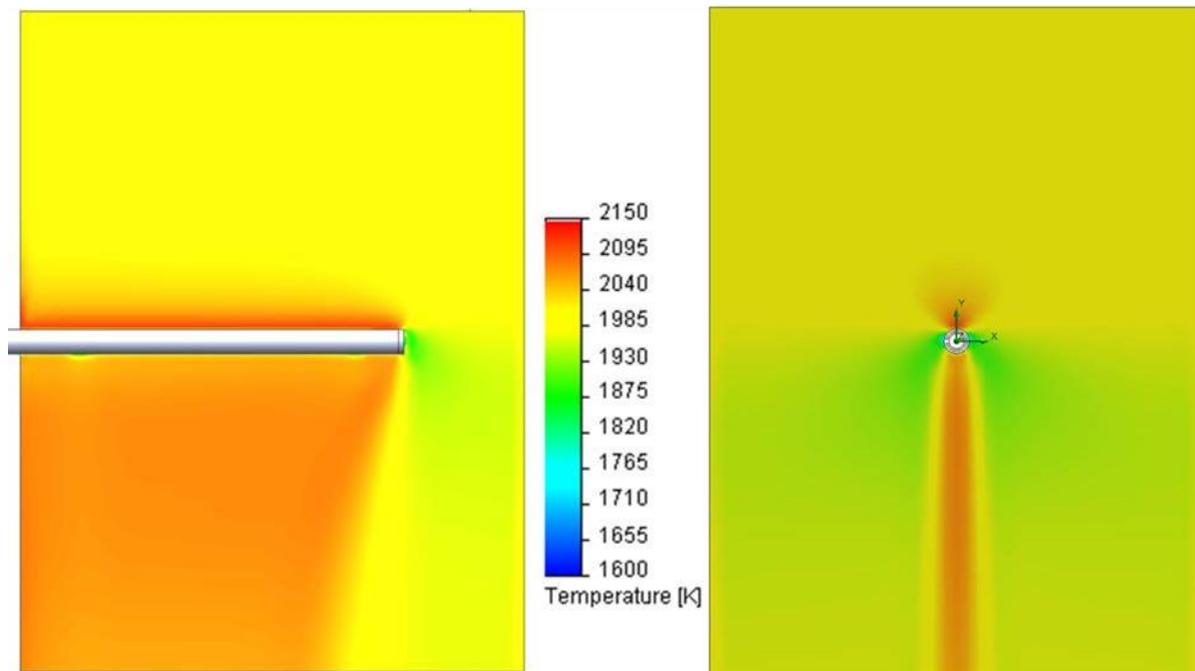


Figure 35. Temperature distribution for Mach 0.7 augmentor flow with flat tip probe insertion of 75%: lateral view (left) and axial view (right).

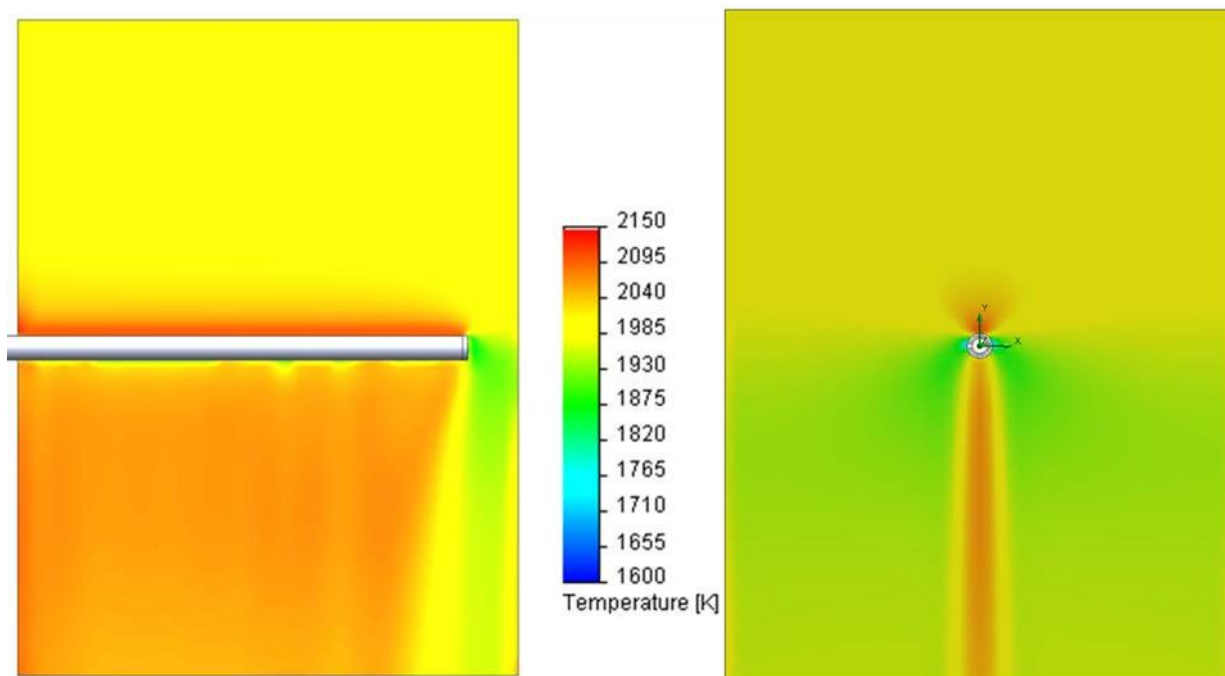


Figure 36. Temperature distribution for Mach 0.7 augmentor flow with flat tip probe insertion of 88.9%: lateral view (left) and axial view (right).

The temperature of the flow field is seen to be greatly affected in the wake of the water-cooled jacket. These effects, like those seen in the flow field velocity distributions, increase both laterally and axially as the jacket is inserted further into the augmentor. In each of the cases shown above, the flow field immediately upstream of the jacket increases to reach a temperature of approximately 2100 K; remains at elevated temperatures in the vicinity of 2050 K in the jacket wake; and reaches temperatures of approximately 1900 K both in front of the jacket tip and in areas surrounding the jacket wake. It may also be seen that the temperature of the flow field is mostly unaffected by the water-cooled jacket at a distance of approximately 2 inches past the tip measured axially along the jacket. The temperature of the flow field in the LDV probe beam focal point region recovers to be approximately equal to that of the freestream most quickly in the 50% insertion distance case.

The flow field velocities and temperatures, shown on the lateral and axial cut planes, are most affected in the areas immediately upstream of the jacket and in the jacket wake. The jacket interference and flow field disturbances generated decrease beyond the jacket tip, but may still be observed in the jacket wake and surrounding areas. From the velocity and temperature distributions shown and discussed in the figures above, it may be seen that the flow field is too greatly affected in the data collection area (60 mm away from LDV probe end) when the augmentor is operating in the Mach 0.7 range. In order to find the flow regime where the jacket least affects the flow field, an insertion distance equal to 50% of the augmentor diameter was further tested at reduced Mach number flows along with modified jacket tip shapes (configurations provided in Table 1 in Section 5.3.3).

6.1.2 Effects of Augmentor Inlet Mach number on Jacket/Flow Field Interaction

It was determined in Section 6.1.1 that the jacket inserted a distance equal to 50% of the augmentor diameter is the configuration that least disturbs the augmentor flow field. In an effort to determine the Mach number range that the cooling jacket causes the least disturbance on the flow field, calculations were conducted with the augmentor flow set to Mach 0.7, 0.5, 0.3, and 0.1. A comparison of these velocity distributions may be seen in Figure 37 and Figure 38.

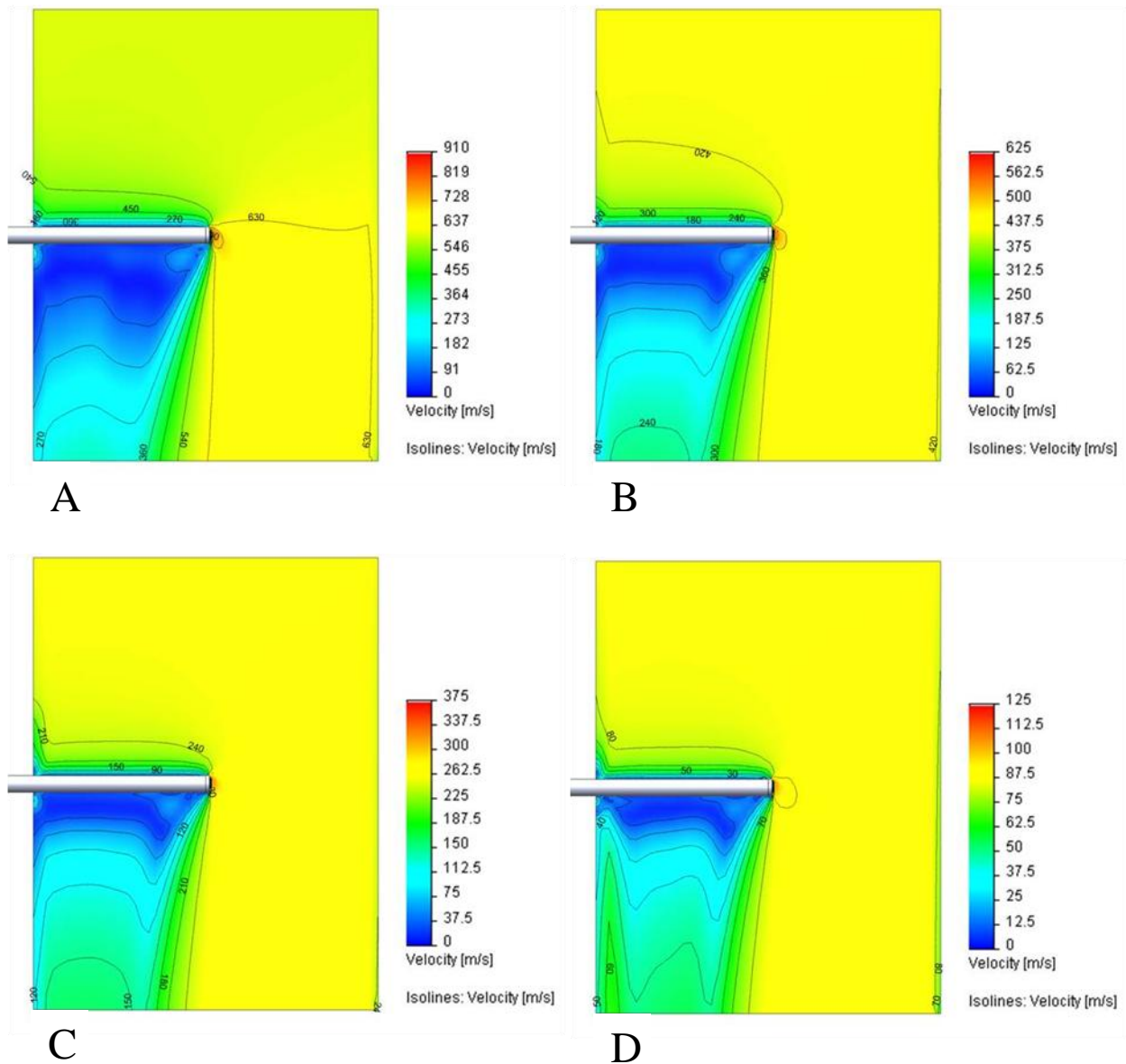


Figure 37. Lateral views of velocity distribution for probe with flat tip at insertion of 50% at augmentor inlet Mach numbers of: A) Mach 0.7 B) Mach 0.5 C) Mach 0.3 D) Mach 0.1.

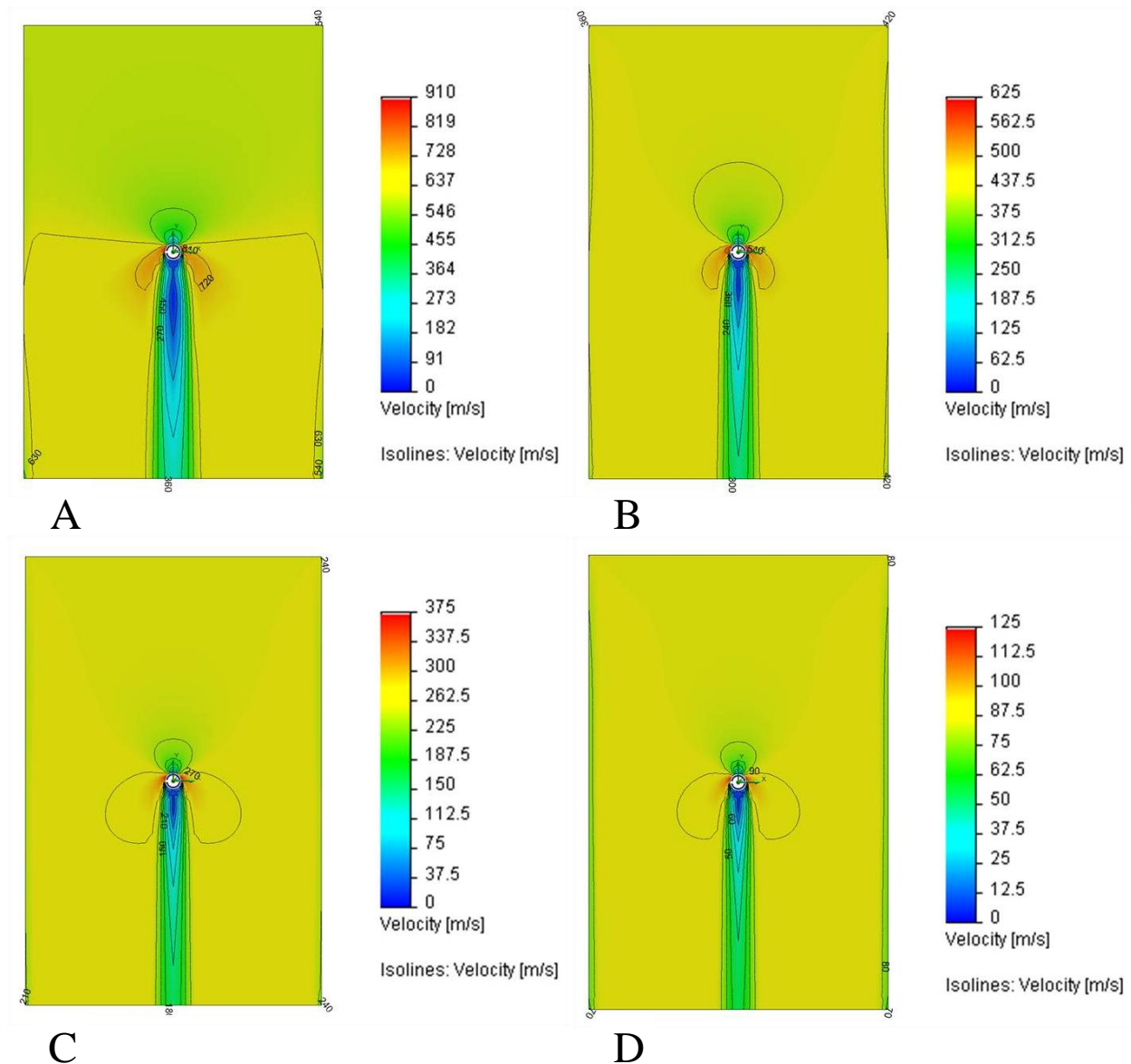


Figure 38. Axial views of velocity distribution for probe with flat tip at insertion of 50% at augmentor inlet Mach numbers of: A) Mach 0.7 B) Mach 0.5 C) Mach 0.3 D) Mach 0.1.

In Figure 37 A (Mach 0.7), it may be seen that the insertion of the probe into the augmentor affects the flow field velocity in the focal point area of the LDV probe laser beams. The freestream velocity of approximately 600 m/s is accelerated to approximately 630 m/s in front of the probe tip. At a flow velocity of Mach 0.7, the water-cooled jacket appears to disturb the flow so that any LDV data collection measurements made would not be accurate representations of the freestream velocity. Therefore, the jacket with a flat tip will not produce accurate results

when inserted into the augmentor with a Mach 0.7 flow. However, the cut plots shown in Figure 37 B, C, and D show reduced augmentor flow velocities in which the jacket affects the freestream flow differently. While the jacket does affect the flow velocity upstream and in its wake, the flow velocity in the area of the LDV probe laser beam focal point appears to be equal to that of the freestream flow velocity. Figure 38 shows that the velocity disturbances in the wake are reduced as the flow field velocity is also decreased. While the wake disturbances decrease, the disturbances around the circumference of the jacket are larger and extend further toward the augmentor walls as the augmentor inlet Mach number is decreased.

The temperature distribution plots with the jacket inserted 50% of the augmentor diameter at flow field velocities of Mach 0.7, 0.5, 0.3, and 0.1 may be seen in Figure 39. In Figure 39 A, corresponding to Mach 0.7 flow, it may be seen that the inserted jacket affects the temperature upstream, in its wake, and in front of the jacket tip (as discussed in 6.1.1), but the effects are different for the Mach 0.5, 0.3, and 0.1 cases. As the flow velocity decreases, the temperature of the flow in the jacket wake also decreases. Figure 39 B shows that the temperature immediately upstream of the jacket increases to approximately 2050 K, while images C and D show temperature variation primarily in the wake of the jacket. For the Mach 0.3 case (Figure 39 C), the temperature in the immediate wake of the jacket decreases to approximately 1900 K and then returns to the freestream temperature shortly after. At Mach 0.1, the flow field temperature decreases to approximately 1700 K in the immediate wake and begins to increase back toward the freestream temperature of 2000 K. Axial views of the temperature variations may be seen in Figure 40. The variation in temperature exists primarily in the jacket wake except for a flow velocity of Mach 0.7 in which a reduced temperature field surrounds the higher temperature wake.

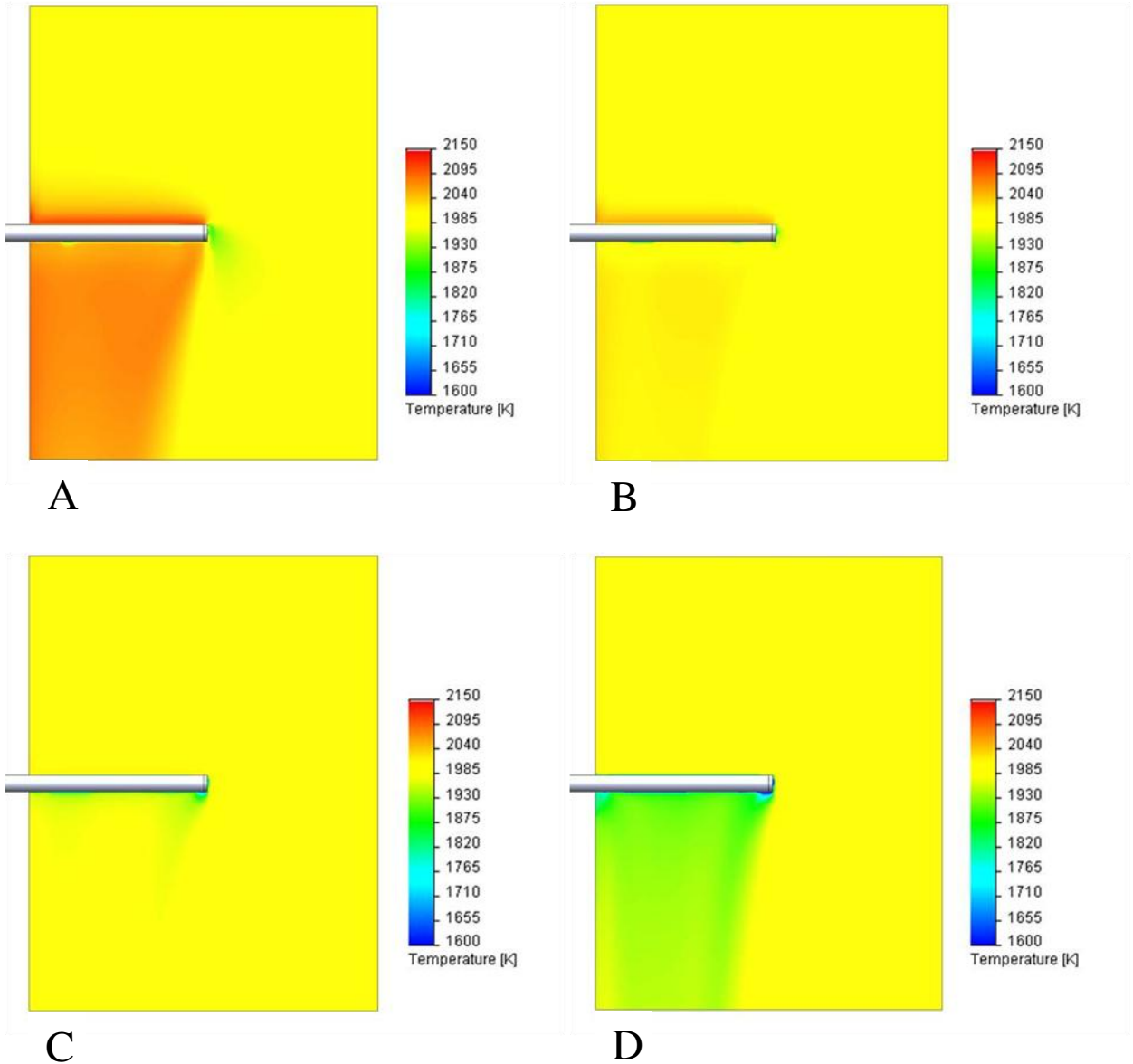


Figure 39. Lateral views of temperature distribution for probe with flat tip at insertion of 50% at augmentor inlet Mach numbers of: A) Mach 0.7 B) Mach 0.5 C) Mach 0.3 D) Mach 0.1.

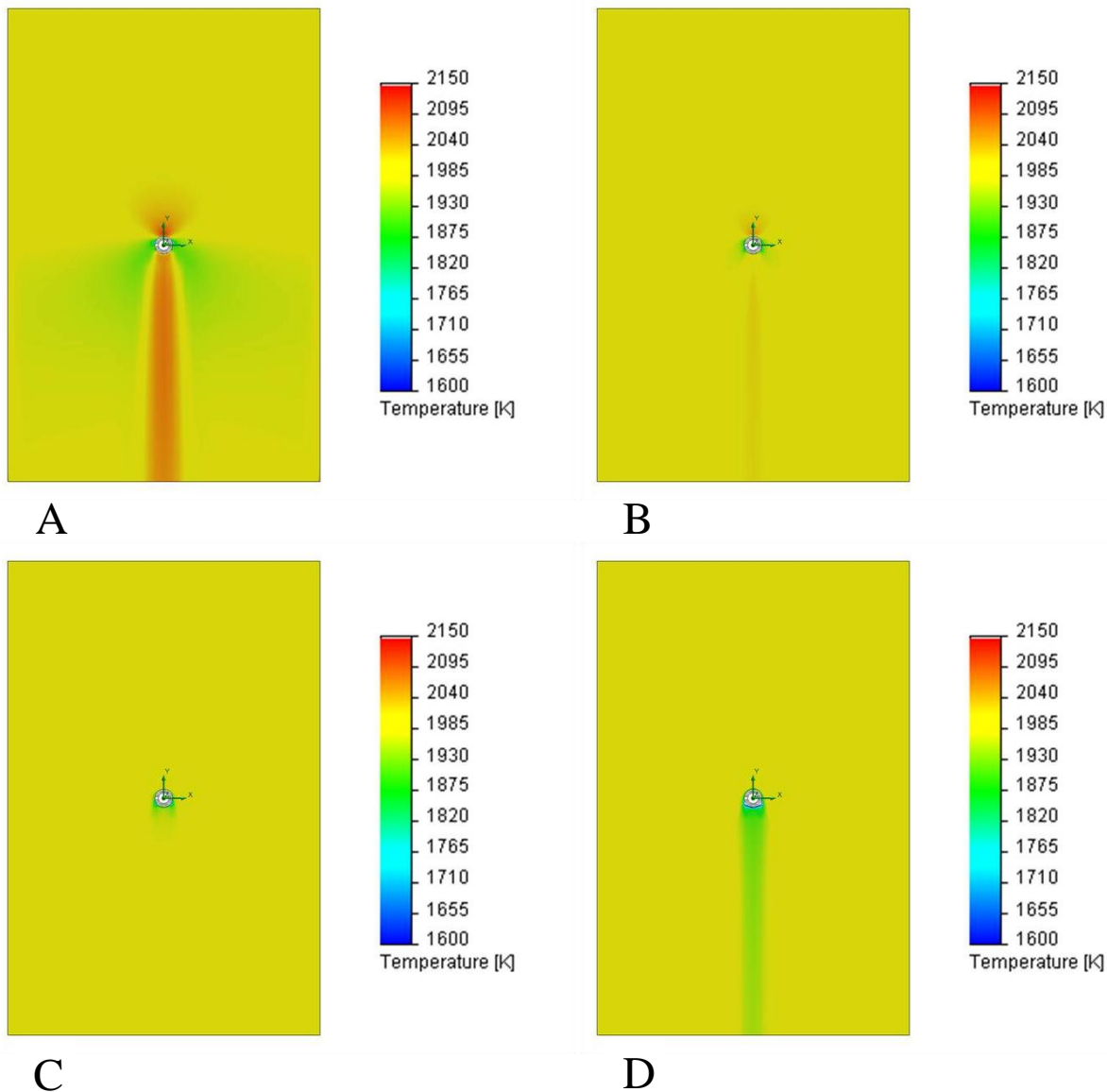


Figure 40. Axial views of temperature distribution for probe with flat tip at insertion of 50% at augmentor inlet Mach numbers of: A) Mach 0.7 B) Mach 0.5 C) Mach 0.3 D) Mach 0.1.

From the results presented in the figures above, it may be seen that the probe with a flat tip inserted 50% of the augmentor diameter at flow velocities of Mach 0.5 and below will allow for accurate LDV probe measurements. In an attempt to further reduce the flow field disturbance and potentially allow LDV measurements to be taken at the nominal GE J-85 augmentor flow conditions (Mach 0.7 at 2000 K), the probe tip design was modified to be hemispherical. The

results obtained from the implementation of a hemispherical tip on the water-cooled probe are discussed in the next section.

6.1.3 Effects of Jacket Tip Modification on Flow Field

The implementation of a hemispherical tip on the probe in an attempt to reduce flow field disturbances is presented in this section. So far, the probe inserted 50% into the augmentor flow at Mach 0.7 has shown that LDV data measurements cannot be taken and provide an accurate representation of the freestream flow velocity. A comparison of the effects of the probe with flat and hemispherical tips in the augmentor operating at Mach 0.7 may be seen in Figure 41 and Figure 42.

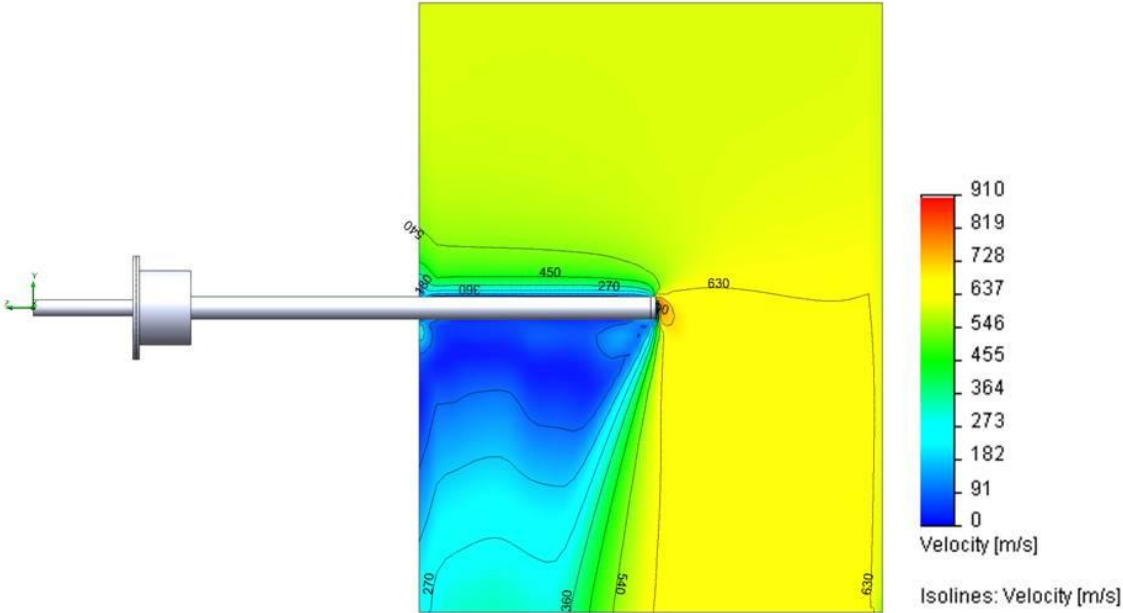


Figure 41. Velocity distribution for Mach 0.7 augmentor flow with flat tip probe insertion of 50%.

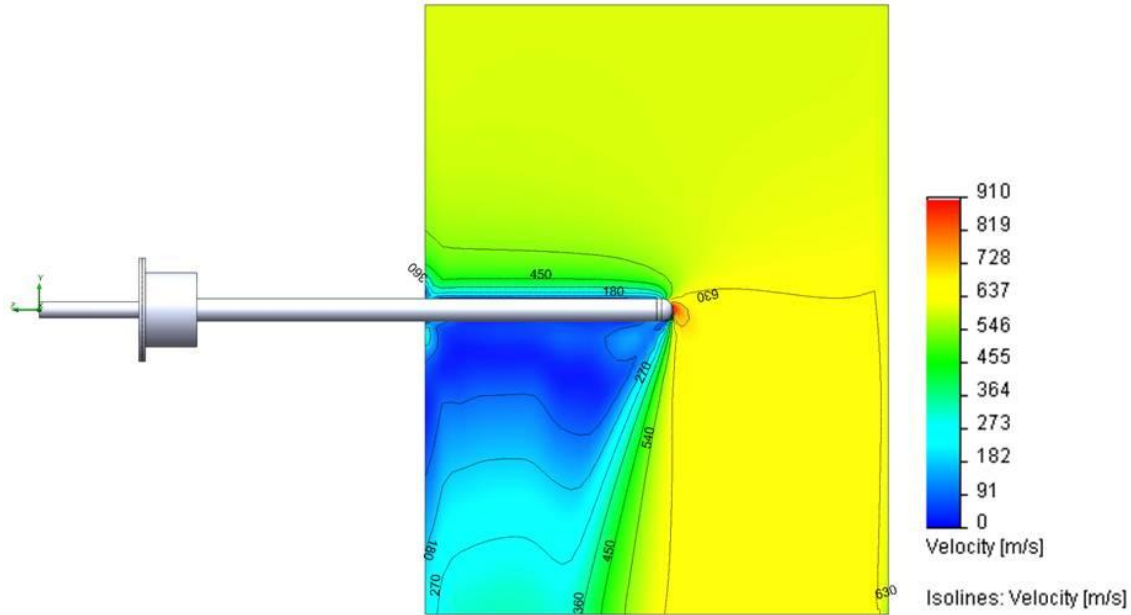


Figure 42. Velocity distribution for Mach 0.7 augmentor flow with hemispherical tip probe insertion of 50%.

The comparison of these two figures shows that the hemispherical tip does not mitigate the disturbance observed in the augmentor flow field velocity distributions when operating at Mach 0.7. Similar results, in which the addition of a hemispherical tip to the jacket does not largely affect the augmentor flow field, have been observed when the augmentor is operating at Mach 0.5 and so are not presented in this section. The images showing the comparison of the flat and hemispherical tips for the probe inserted 50% of the augmentor diameter operating at Mach 0.5 may be found in Appendix D. While the tip modification did not reduce flow disturbances at Mach 0.7 or Mach 0.5, the velocity distribution in the wake of the jacket is altered by the addition of a hemispherical tip in the Mach 0.3 and Mach 0.1 cases. These comparisons may be seen in Figure 43 and Figure 44 for Mach 0.3 augmentor flow velocity and Figure 45 and Figure 46 for Mach 0.1 augmentor flow velocity. The velocity isolines in Figure 43 show arc-like structures and the isolines in Figure 44 show the isolines approaching a saddle-like structure. When further reducing the augmentor flow velocity to Mach 0.1, the flat tip (Figure 45) shows

the isolines approaching a saddle-like structure while the hemispherical tip (Figure 46) shows fully developed saddle structures in the isolines.

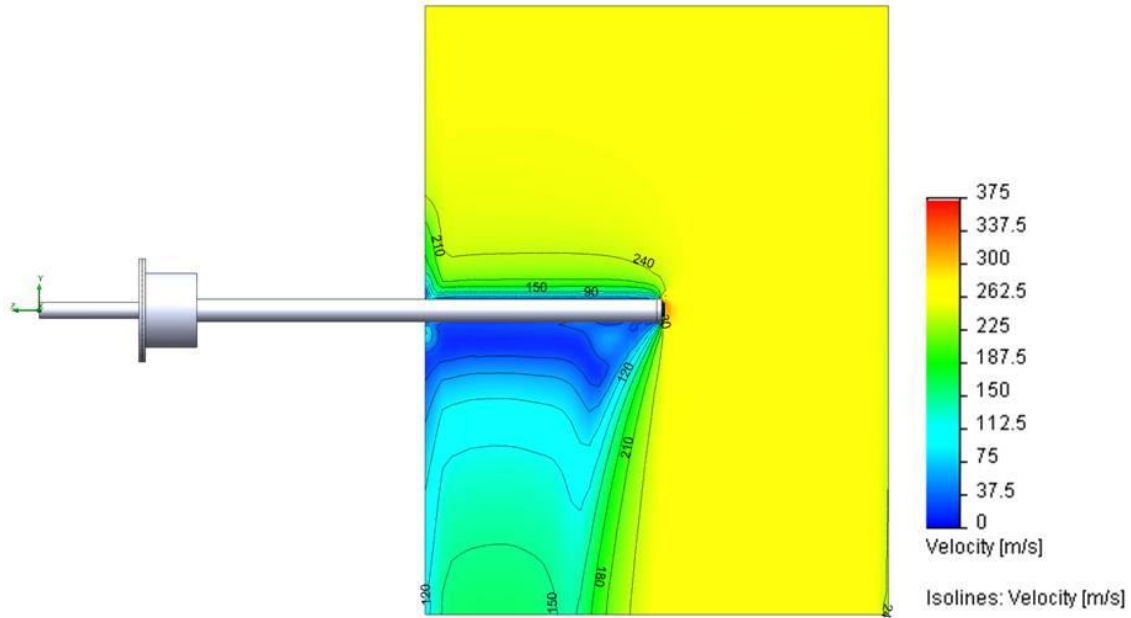


Figure 43. Velocity distribution for Mach 0.3 augmentor flow with flat tip probe insertion of 50%.

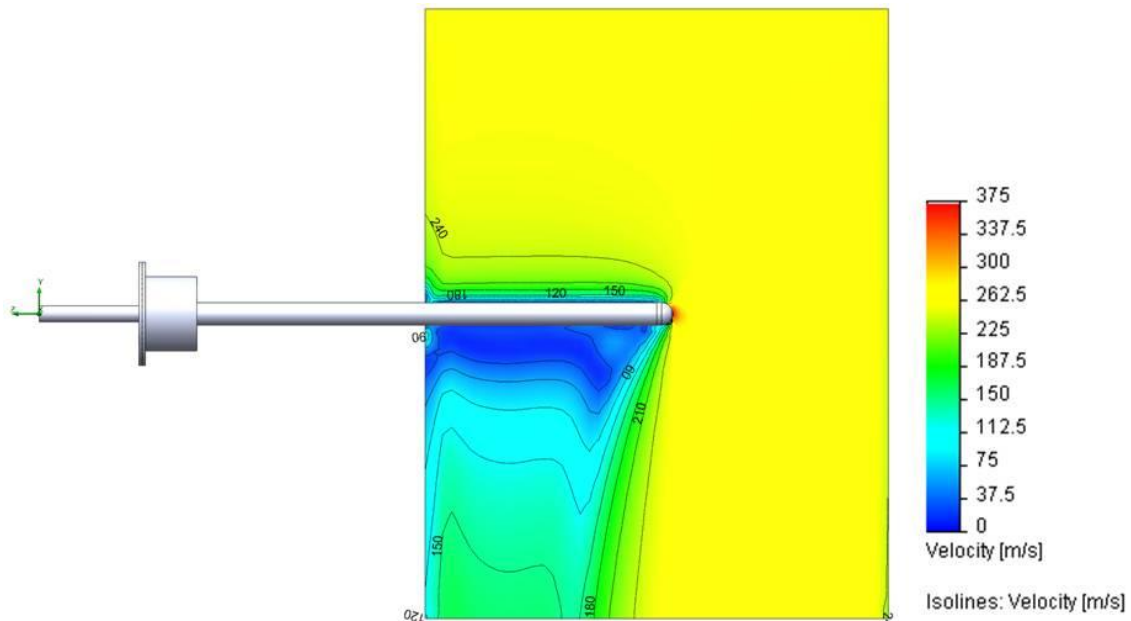


Figure 44. Velocity distribution for Mach 0.3 augmentor flow with hemispherical tip probe insertion of 50%.

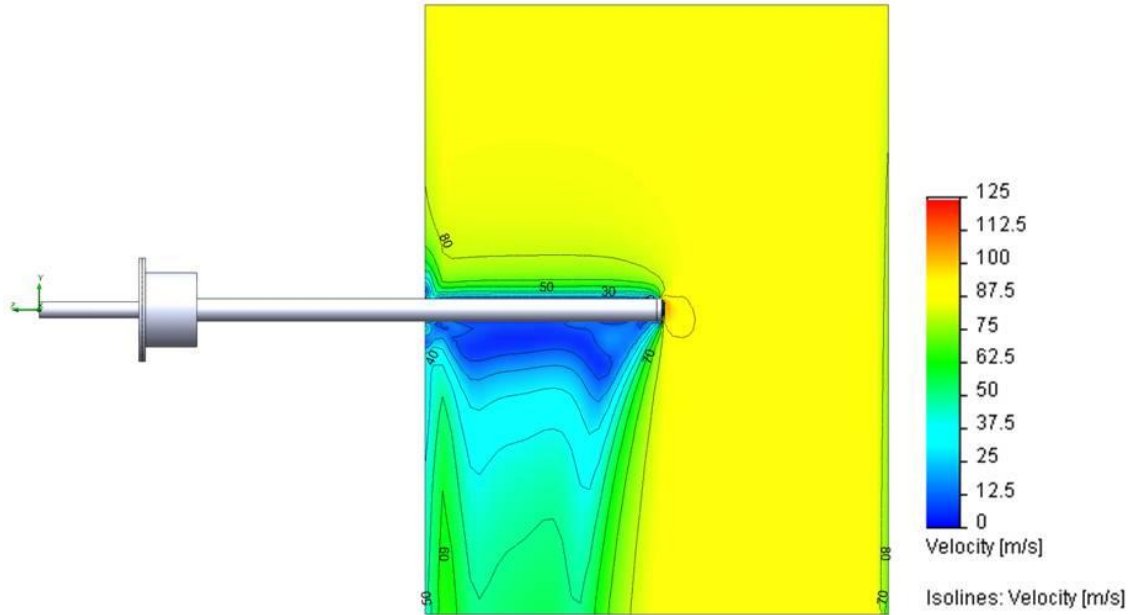


Figure 45. Velocity distribution for Mach 0.1 augmentor flow with flat tip probe insertion of 50%.

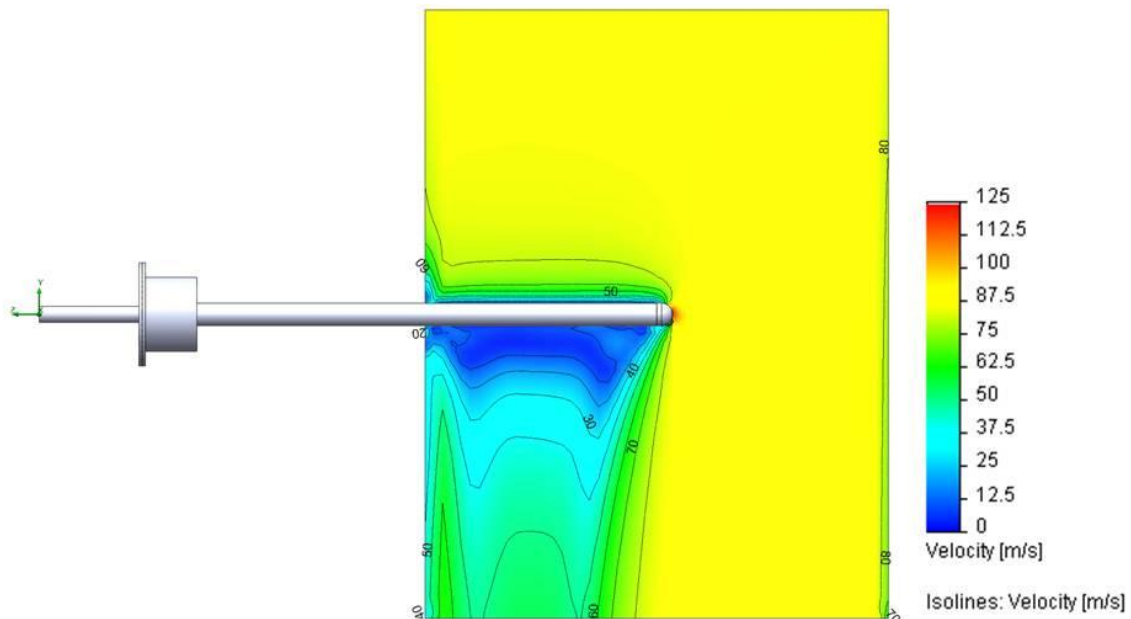


Figure 46. Velocity distribution for Mach 0.1 augmentor flow with hemispherical tip probe insertion of 50%.

From these cut plots and comparisons showing the velocity distributions of the probe inserted 50% with flat and hemispherical tips, it can be seen that the addition of a hemispherical tip to the water-cooled jacket adds few benefits in its current use. However, the rounded tip

could later be modified to increase the flow efficiency of the cooling fluid within the jacket, and so it will remain a topic of discussion in future sections. It has been determined that the insertion of the probe 50% of the augmentor diameter into the flow will not alter the flow field so as to compromise LDV data collection measurements in flow velocities of Mach 0.5 and below either with a flat or hemispherical tip. The full set of flow field velocity and temperature distribution plots for the different configurations listed in Table 1 in Section 5.3.3 may be seen in Appendix D. The effects of the flow field on the probe and the cooling water are discussed in the following sections.

6.2 Probe Tip Temperature Distributions

The figures presented in Section 6.1 provide an understanding of how the probe affects the flow field, but not how the flow field affects the temperature of the probe or the temperature of the cooling fluid traveling through the probe. This section shows results obtained from the simulations focused on the tip of each probe configuration listed in Table 1. A comparison of the temperature distribution in the tip of the probe configurations of 50%, 75%, and 88.9% with flat tips at Mach 0.7 may be seen in Figure 47, Figure 48, and Figure 49, respectively.

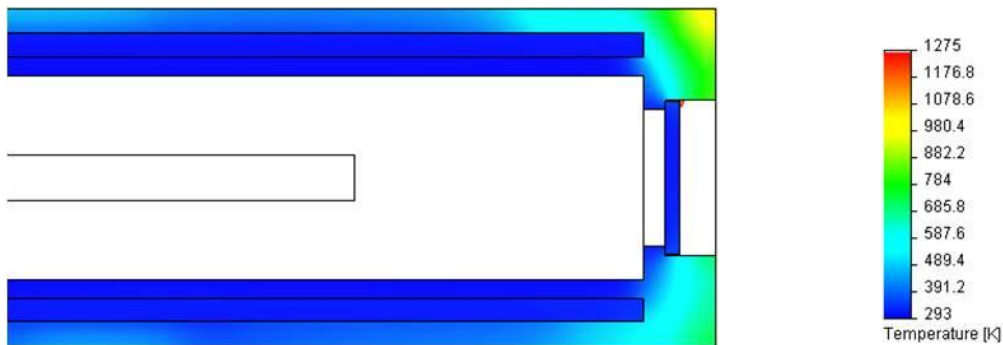


Figure 47. Magnified tip temperature distribution for Mach 0.7 augmentor flow with flat tip probe insertion of 50%.

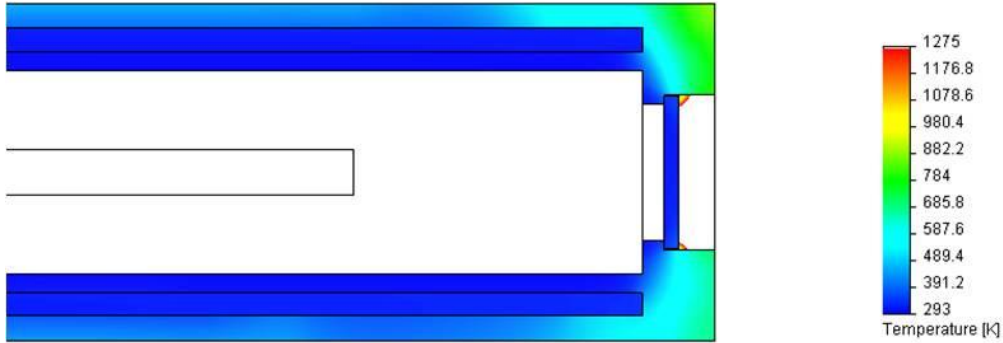


Figure 48. Magnified tip temperature distribution for Mach 0.7 augmentor flow with flat tip probe insertion of 75%.

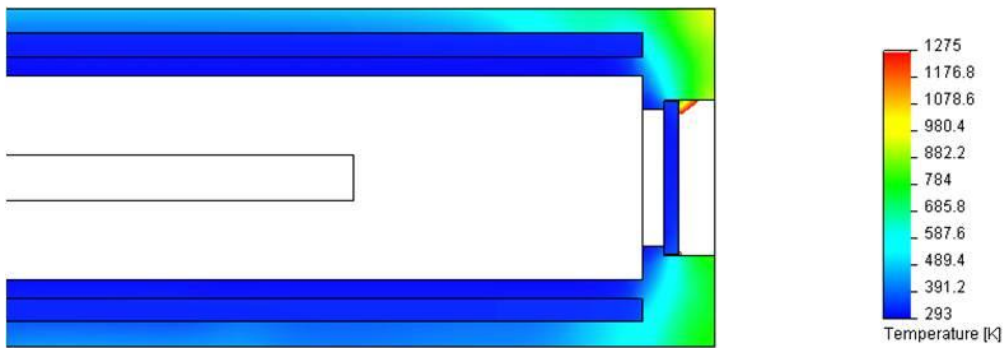


Figure 49. Magnified tip temperature distribution for Mach 0.7 augmentor flow with flat tip probe insertion of 88.9%.

The temperature scales in each of the figures is broad enough to provide an accurate representation of the temperature throughout the stainless steel walls of the jacket, but is beyond the range needed to show the temperature of the fluid traveling throughout the jacket. The results discussing the temperature of the cooling fluid will be presented in Section 6.3. It can be seen in the figures above that the area of the jacket that reaches the highest temperature is the tip facing the incoming flow (top, where there is no contact with the cooling flow), while the outer jacket wall as a whole experiences the greatest temperature increase, as is to be expected. These figures show that the outer walls climb from approximately 400 K to approximately 1000 K for an insertion distance of 50%. The maximum temperature reached is approximately 800 K for an insertion distance of 75% and approximately 900 K for an insertion distance of 88.9%. The

probe configuration inserted 50% of the augmentor diameter experiences the greatest temperature because the tip ends along the center line of the augmentor flow.

A comparison of the flat and hemispherical jacket tips implemented in this research at Mach 0.5 may be seen in Figure 50 and Figure 51.

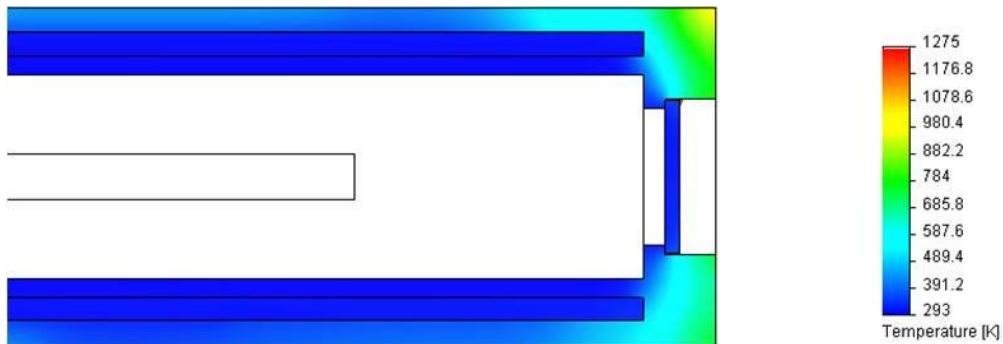


Figure 50. Magnified tip temperature distribution for Mach 0.5 augmentor flow with flat tip probe insertion of 50%.

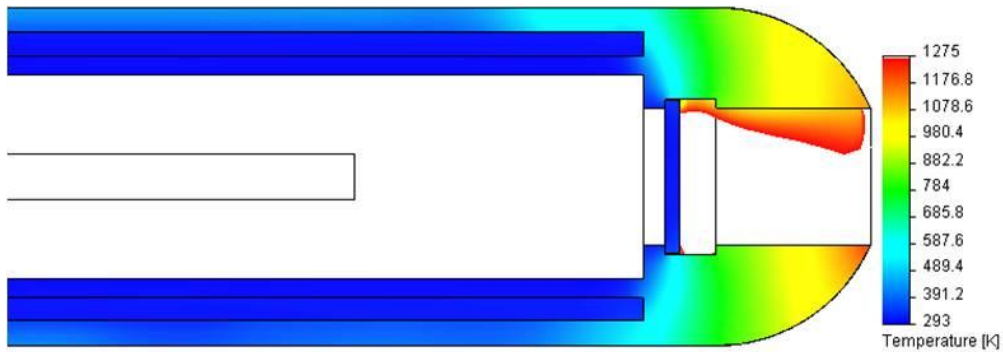


Figure 51. Magnified tip temperature distribution for Mach 0.5 augmentor flow with hemispherical tip probe insertion of 50%.

It is quite obvious that the probe configuration with the hemispherical tip experiences an even greater increase in temperature. This temperature increase is caused by the fact that the hemispherical tips were not added in a way that allows cooling throughout them, but instead were simply mounted to the existing flat tip of the jacket. The maximum temperature reached in the configuration using a hemispherical tip inserted into a Mach 0.5 flow is approximately 1100 K. The remaining cases in which the flat tip configuration is compared to the hemispherical tip

configuration show similar results to those observed in Figure 50 and Figure 51 with the only differences being the maximum temperature reached by the outer-most edge of the jacket tips may be seen in Appendix E.

As previously discussed in Section 5.3.3, a “worst case scenario” was simulated in which the pressure washer failed, eliminating the cooling flow through the jacket. Figure 52 shows the numerical results obtained for the probe inserted 50% at Mach 0.7 with a flat tip with no cooling water flowing through the jacket.

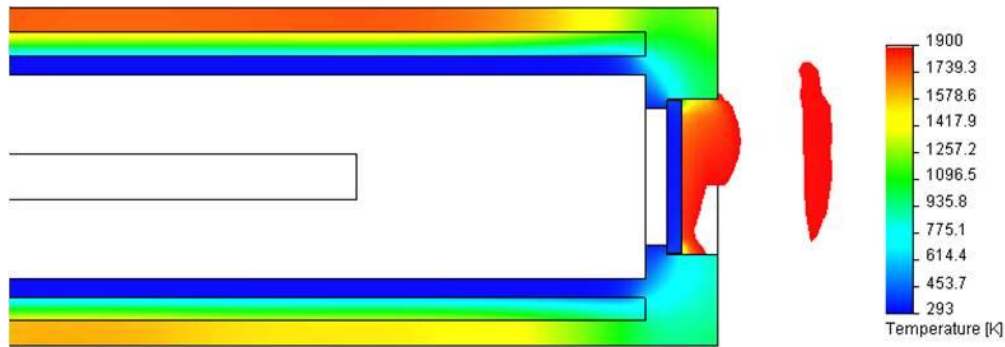


Figure 52. Magnified tip temperature distribution for Mach 0.7 augmentor flow with flat tip probe insertion of 50%—No water.

It can be seen from the figure above that the maximum temperature reached in this case is approximately 1800 K, which is above the melting temperature of the stainless steel walls of 1683.15 K. The results for the “worst case scenario” simulations for insertion distances of 75% and 88.9% are similar to those observed in Figure 52 and may be found in Appendix E.

From the cut plots presented and discussed in this section, it has been determined that the probe will not reach solid wall temperatures beyond the melting point of the stainless steel alloy used in this research as long as the cooling fluid continues to flow throughout the jacket. The full set of magnified tip temperature plots for the different configurations listed in Table 1 may be seen in Appendix E. The next section discusses the temperature and fluid temperature distributions observed at different planar locations along the length of the jacket.

6.3 Cut Plane Temperature Distributions

In order to show a more accurate representation of the temperatures of both solids and fluids throughout the jacket, contour plots on eight different locations were created at various points along the axial length of the jacket. Each of the eight planes and their locations are shown in Figure 53 and are the same regardless of tip configuration. In this case, the configuration shown in the figure below is the probe inserted 50% at Mach 0.7 with the flat tip to show that the water-cooled jacket is capable of operation within these flow conditions.

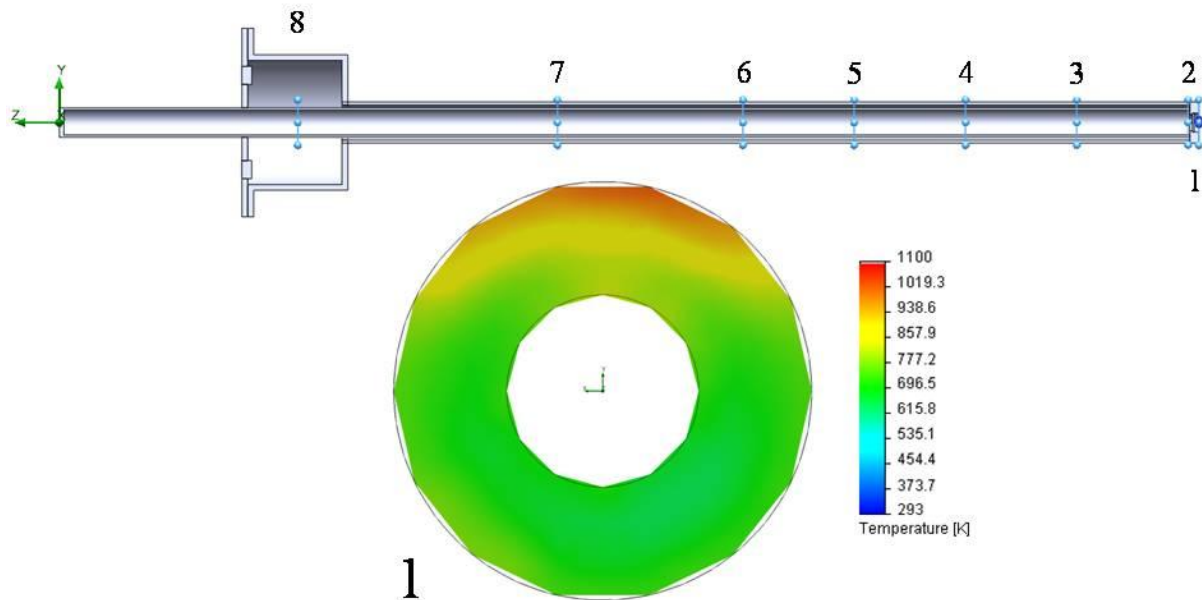


Figure 53. Plane locations along jacket length (top). Temperature distribution for probe insertion of 50% at Mach 0.7 with flat tip at Plane 1 (bottom).

Plane 1, which is located on the outer face of the flat jacket tip, shows the temperature distribution of the solid walls and may be seen in Figure 53. Plane 2 is located 1 mm away from the inner face of the jacket tip (same for flat and hemispherical tip configurations), which is equivalent to 5.76 mm inside the jacket from Plane 1. Planes 3, 4, 5, and 6 are placed in 60 mm increments from Plane 2 traveling toward the reservoir tank. Plane 7 is located a distance of 100 mm inside the jacket from Plane 6 and Plane 8 is located 140 mm from Plane 7. Figure 54

shows the temperature distributions of solid and fluid temperatures on the left and the fluid temperature separately on the right at Planes 2, 3, and 4 within the jacket when inserted into the augmentor flow field. The temperature scales in these figures differ from plane to plane for the solid and fluid temperature together (left) in order to provide a range of temperatures that best represents each particular plane. The minimum temperature for each scale is 293 K. The maximum scale temperatures for each plane showing both solid and fluid temperatures with the probe inserted 50% at Mach 0.7 with the flat tip are as follows: Plane 1—1100 K; Plane 2—700 K; Planes 3-5—500 K; Planes 6-8—350 K. The maximum temperature on the scale for each of the planes showing only the isolated fluid temperature is 373 K, which is the boiling point of water at standard atmospheric conditions. Figure 55 shows the temperatures at Planes 5, 6, and 7 while Figure 56 shows the temperatures at Plane 8. In each of these figures, the incoming water is shown on the top portion and the exiting water is on the bottom.

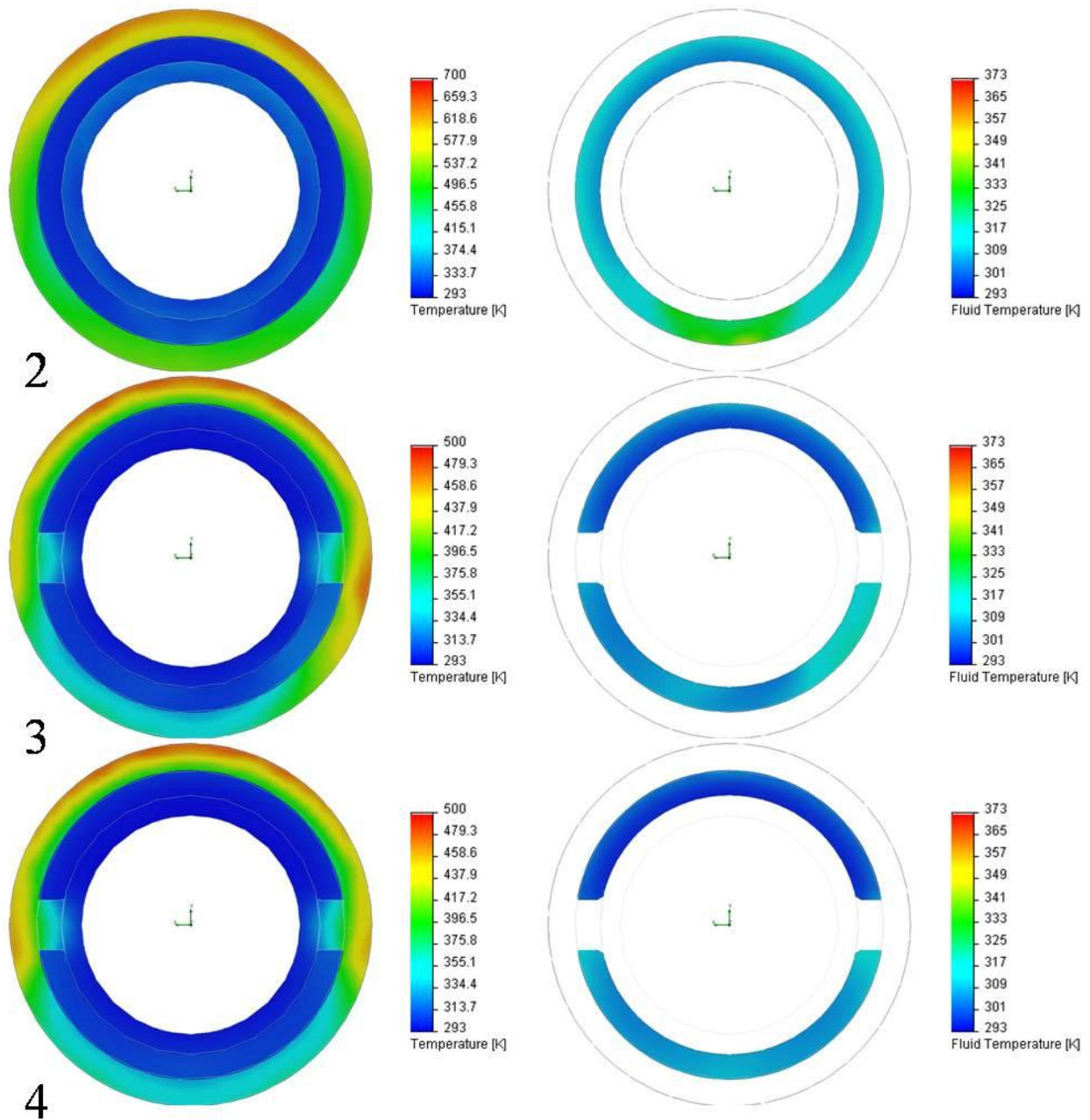


Figure 54. Temperature (left) and Fluid Temperature (right) distributions for probe insertion of 50% at Mach 0.7 with flat tip at Planes 2, 3, and 4.

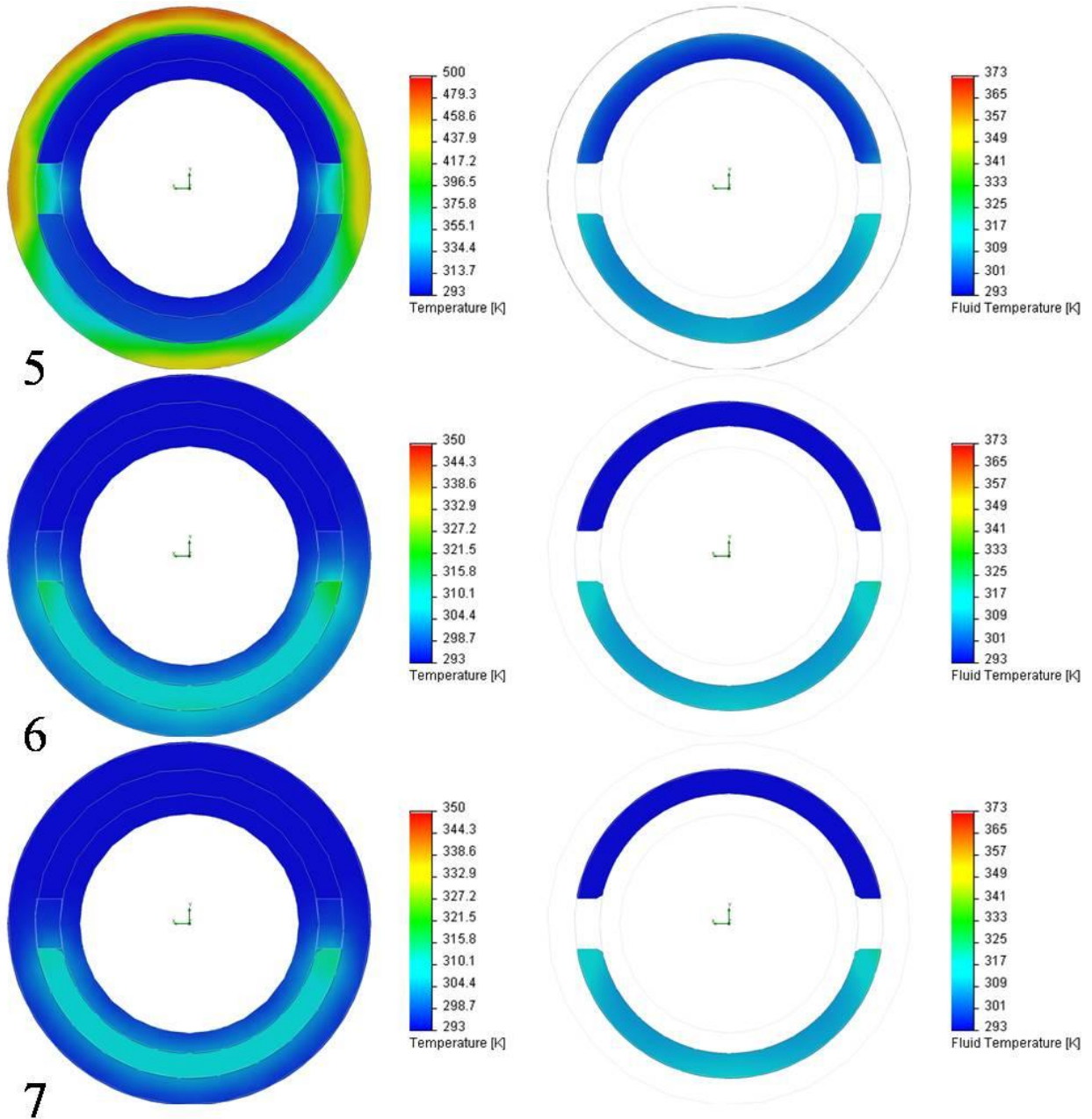


Figure 55. Temperature (left) and Fluid Temperature (right) distributions for probe insertion of 50% at Mach 0.7 with flat tip at Planes 5, 6, and 7.

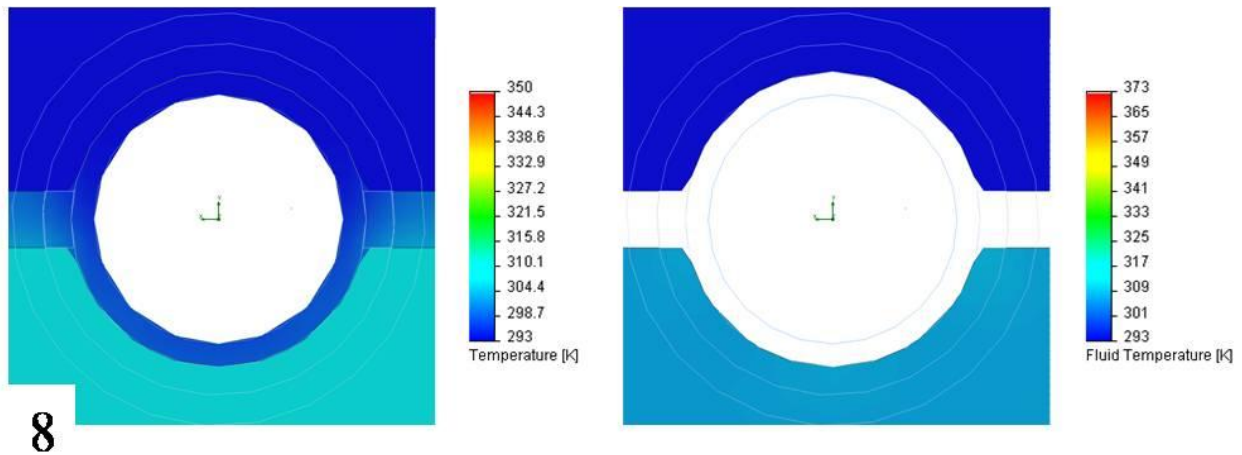


Figure 56. Temperature (left) and Fluid Temperature (right) distributions for probe insertion of 50% at Mach 0.7 with flat tip at Plane 8.

From these figures, it is easy to see which planes along the probe axis are located within the augmentor and which planes are located outside the augmentor. These figures also show that the solid walls of the probe experience a wide variation in temperature along the jacket length while the water temperature increases in temperature as it travels through the jacket reaching a maximum temperature of approximately 340 K. As the water exits the augmentor section, it begins to cool and reaches a temperature of approximately 310 K once it enters the reservoir tank at Plane 8. The results obtained at each of the eight planar locations are similar for each configuration and only differ by the maximum temperatures reached in solid and fluid regions and which planes are located inside the augmentor section. The full set of temperature contour plots at each of the planes for all of the configurations simulated and analyzed with water flowing through the jacket may be seen in Appendix F.

CHAPTER 7

CONCLUSIONS AND FUTURE WORK

The design, development, and computations of a water-cooled jacket for use in conjunction with an existing sub-miniature LDV probe in rocket and gas-turbine engine environments have been reported. The design and development of the jacket were completed using the 3D parametric modeling software package SolidWorks. The computational fluid dynamics add-in component of SolidWorks, called FloWorks, was used to carry out the computational analysis of the interaction of the water-cooled jacket and the extreme flow conditions found in the augmentor section of a GE J-85 jet engine.

7.1 Model Configurations

The water-cooling jacket has been analyzed at three different insertion distances relative to the dimensions of the augmentor after first determining the pre-defined grid mesh setting to optimize the accuracy of results and to minimize the time necessary for each of the computations. Along with these three different insertion distances tested (50%, 75%, and 88.9% of the 18 inch augmentor diameter) using the flat probe tip, variations of the probe tip (flat and hemispherical) were analyzed and the augmentor inlet Mach number was reduced in an attempt to mitigate flow field disturbance. Several configurations were also analyzed in order to simulate a “worst case scenario” in which the water supply or pressure washer were to fail and stop the flow of the coolant throughout the jacket.

7.2 Conclusions

The jacket has been shown to withstand the extreme environment experienced in a Mach 0.7 flow at 2000 K by using the water-cooling to prevent the stainless steel walls from melting as well as keeping the water at sub-boiling temperatures. However, in the event that either the supply of water or the pressure washer were to fail while the jacket is inserted into the augmentor, the jacket and any equipment inside will fail catastrophically as a result. This was shown in the figures in which a “worst case scenario” was analyzed and showed that the outer walls of the jacket reach temperatures of approximately 1800 K. The jacket would most certainly fail in these conditions as the melting temperature of the stainless steel alloy modeled is 1683.15 K.

The computational results obtained in this research indicate that the jacket design interferes with the augmentor flow field. Combinations of different jacket tips and reduced freestream Mach number flow at an insertion distance of 50% were evaluated to determine where the flow field/jacket disturbances were minimized. It was determined that the velocity of the flow field in the LDV laser beam focal point region (60 mm from the inner face of the jacket tip) approximately matches the freestream flow velocity when the freestream Mach numbers 0.5 and below are used. The implementation of a hemispherical jacket tip did not appear to reduce the flow disturbances as much as was expected.

7.3 Future Work

The research presented here, along with the results obtained, leave several possible avenues available for future research and design modifications. The dimensions of the LDV probe developed by Esirgemez and Ölçmen (2005) were the driving factors of the design of the

water-cooling jacket. In order to reduce the size of the cooling jacket, the LDV probe must first be redesigned to reduce the overall diameter. By reducing the overall size of the cooling jacket, the disturbances in the freestream flow field may also be reduced as a direct result. Along with reducing the overall diameter of the water-cooling jacket, an alternate cross-sectional shape may be applied. The modified shape of the jacket may be made to resemble an airfoil to aid in the reduction of flow field disturbances. The purpose of the hemispherical tip was to help reduce flow interference, but it was observed that this tip experienced temperatures greater than the rest of the outer walls of the jacket due to the lack of cooling in this region. The implementation of the hemispherical tip may be further modified to allow cooling liquid to reach the region and improve cooling fluid flow efficiency. These design modifications could potentially increase the cooling ability of the jacket and the reliability of the system by reducing the flow interference.

Before the potential design modifications of both the LDV probe and the water-cooling jacket are explored, the current jacket must be first tested experimentally in a hot flow. The data and results obtained from these real-world experiments would allow for the verification of the numerical analysis and simulations presented in this research. After experimentally verifying the results, future CFD computations may be reliably used to make new designs and improve existing designs.

REFERENCES

- , "COSMOS 2008: COSMOSFloWorks Fundamentals," Penn State Personal Web Server: Jeremy Alan Hall [online], URL: <http://www.personal.psu.edu/jah5420/Misc/SolidWorks/COSMOSFloWorks/FloWorks/lang/english/Docs/Fundamentals.pdf> [cited January 2011].
- , "Standard for Testing and Rating Performance of Pressure Washers: Determination of Pressure and Water Flow," Pressure Washer Manufacturers' Association, PWMA PW101-2010, Cleveland, OH, 2010.
- Albrecht, H.E., Borys, M., Damaschke, N., and Tropea, C., *Laser Doppler and Phase Doppler Measurement Techniques*, Springer-Verlag, Berlin, 2003, Chaps. 1, 2, 5.
- Bates, S.C., and Pollack, M.J., "Gas Cooled Probe Protectors," *SPIE Harsh Environment Sensors II*, Vol. 3852, 8 December 1999, pp. 113-123.
- Beitel, G.R., Catalano, D.R., and Edwards, R., "Electroformed Diagnostic Probes for High-Temperature Gas Flows," *24th AIAA Aerodynamic Measurement Technology and Ground Testing Conference*, AIAA 2004-2592, Portland, OR, 28 June-1 July 2004.
- Beitel, G.R., Plemmons, D.H., Catalano, D.R., Hiers, R.S. III, "Development of Gas Turbine Engine Embedded Instrumentation," *U.S. Air Force T&E Days*, AIAA 2005-7645, Nashville, TN, 6-8 December 2005.
- Beitel, G.R., Savage, K.P., Catalano, D.R., and Hiers, R.S. III, "Combustor Imaging Probe for Gas Turbine Engines," *43rd AIAA/ASME/SAE/ASEE Joint Propulsion Conference & Exhibit*, AIAA 2007-5717, Cincinnati, OH, 8-11 July 2007.
- Bohátka, S., Szöör, Gy., Czél, Gy., and Balázs, É., "High temperature direct probe for MS and its use for thermal decomposition monitoring," *Vacuum*, Vol. 80, 14 October 2005, pp. 247-252.
- Brouckaert, J.-F., Mersinligil, M., and Pau, M., "A Conceptual Design Study for a New High Temperature Fast Response Cooled Total Pressure Probe," *Journal of Engineering for Gas Turbines and Power*, Vol. 131, March 2009.
- Ciezki, H.K., and Schwein, B., "Investigation of gaseous and solid reaction products in a step combustor using a water-cooled sampling probe," *32nd AIAA/ASME/SAE/ASEE Joint Propulsion Conference & Exhibit*, AIAA 1996-2768, Lake Buena Vista, FL, 1-3 July 1996.

Ebrahimi, H.B., "Overview of Gas Turbine Augmentor Design, Operation, and Combustion Oscillation," *42nd AIAA/ASME/SAE/ASEE Joint Propulsion Conference & Exhibit*, AIAA 2006-4916, Sacramento, CA, 9-12 July 2006.

Esirgemez, E., and Ölçmen, S. M., "A spark-plug LDV probe for in-cylinder flow analysis of production IC engines," *Measurement Science and Technology*, Vol. 16, September 2005, pp. 2038-2047.

Grey, J., and Jacobs, P.F., "Cooled Electrostatic Probe," *AIAA Journal*, Vol. 5, No. 1, 1967, pp.84-90.

Grey, J., Jacobs, P.F., and Sherman, M.P., "Calorimetric Probe for the Measurement of Extremely High Temperatures," *The Review of Scientific Instruments*, Vol. 33, No. 7, July 1962, pp. 738-741.

Hiers, R.S. III, and Hiers, R.S. Jr., "Development of Exit-Plane Probes for Turbine Engine Condition Monitoring," *38th AIAA/ASME/SAE/ASEE Joint Propulsion Conference and Exhibit*, AIAA 2002-4304, Indianapolis, IN, 7-10 July 2002.

Hiers, R.S. Jr., and Hiers, R.S. III, "Development of High-Temperature Image Probes for Viewing Turbine Engine Augmentors," *22nd AIAA Aerodynamic Measurement Technology and Ground Testing Conference*, AIAA 2002-2919, St. Louis, MO, 24-26 June 2002.

Hurley, C.D., Copplestone, R.W., and Wilson, C.W., "Optical Measurements of Turbulence and Residence Time in a Gas Turbine Combustor," *35th AIAA/ASME/SAE/ASEE Joint Propulsion Conference & Exhibit*, AIAA 1999-2641, Los Angeles, CA, 20-23 June 1999.

Ivanchenko, O., Esirgemez, E., and Ölçmen, S., "A miniature three-component LDV probe," *Measurement Science and Technology*, Vol. 18, May 2007, pp. 2014-2020.

Jankovic, M., and Mostaghimi, J., "Thermally Induced Measurement Error by a Water-Cooled Enthalpy Probe," *Plasma Chemistry and Plasma Processing*, Vol. 18, No. 1, 1998, pp. 53-71.

Jiang, L., Manipurath, S., Bourque, G., and Houde, M., "Flow field of a triple-walled gas-sampling probe with sub-cooled boiling effect," *Flow Measurement and Instrumentation*, Vol. 18, June 2007, pp. 156-165.

Lagen, N.T., and Seiner, J.M., "Correction Analysis for a Supersonic Water Cooled Total Temperature Probe Tested to 1370 K," *International Congress on Instrumentation in Aerospace Simulation Facilities*, IEEE, Rockville, MD, 27-31 October 1991, pp. 123-135.

Lagen, N.T., and Seiner, J.M., "Evaluation of Water Cooled Supersonic Temperature and Pressure Probes for Application to 2000°F Flows," NASA TM-102612, June 1990.

Liebert, C.H., "Miniature Convection Cooled Plug-Type Heat Flux Gauges," NASA TM-106483, February 1994.

Liebert, C.H., "Miniature High Temperature Plug-Type Heat Flux Gauges," NASA TM-105403, 1992.

Liebert, C.H., and Kolodziej, P., "Dual Active Surface Heat Flux Gage Probe," NASA TM-106861, February 1995.

Lombard, Matt, *SolidWorks 2010 Bible*, Wiley, Indianapolis, IN, 2010, Chaps. 4, 10, 12, 24.

MacKinnon, H.M., Beitel, G.R., Hiers, R.S. III, and Catalano, D.R., "Advances in Aerodynamic Probes for High-Enthalpy Applications," 24th AIAA Aerodynamic Measurement Technology and Ground Testing Conference, AIAA 2004-2594, Portland, OR, 28 June-1 July 2004.

Martin, J.K., Witze, P.O., Borgnakke, C., "Multiparameter Conditionally Sampled Laser Velocimetry Measurements During Flame Propagation in a Spark Ignition Engine," *Twentieth Symposium (International) on Combustion*, Vol. 20, No. 1, 1985, pp. 29-36.

Most, J.M, Trouillet, P., Jallais, S., Mandin, P., Marchand, F., Le-Masson, C., Witwicki, P., and Rampelberg, D., "Development of a LDV Probe for Velocity Measurements in a 600MW Pulverized Coal Power Plant," 10th International Symposium on Applications of Laser Techniques to Fluid Mechanics, Lisbon, Portugal, 10-13 July 2000.

Ölçmen, S., and Daly, D.T. (To The University of Alabama), "Spark-Plug LDV, LIF, and LII Probe for Engine Flow and Combustion Analysis," U.S. Patent 7,395,699, 8 July 2008.

Rottier, C., Godard, G., Corbin, F., Boukhalfa, A.M., and Honore, D., "An endoscopic particle image velocimetry system for high-temperature furnaces," *Measurement Science and Technology*, Vol. 21, September 2010.

Savage, K.P., Winkleman, B.C., Beitel, G.R., Plemmons, D.H., Catalano, D.R., and Hiers, R.S. III, "Imaging Probes for Gas Turbine Engines," 42nd AIAA/ASME/SAE/ASEE Joint Propulsion Conference & Exhibit, AIAA 2006-4301, Sacramento, CA, 9-12 July 2006.

SolidWorks Education Edition, Software Package, 2010-2011, Dassault Systèmes, The University of Alabama, Tuscaloosa, AL, 2010.

Suits, E.L., Plemmons, D.H., Beitel, G.R., Howard, R.P., and Hiers, R.S. III, "Gas Turbine Engine Flow-Field Diagnostics: Needs, Capabilities, and Proposed Development," 25th AIAA Aerodynamic Measurement Technology and Ground Testing Conference, AIAA 2006-3440, San Francisco, California, 5-8 June 2006.

Verscheure, K., Campforts, M., Verhaeghe, F., Boydens, E., Van Camp, M., Blanpain, B., and Wollants, P., "Water-Cooled Probe Technique for the Study of Freeze Lining Formation," *Metallurgical and Materials Transactions B*, Vol. 37B, December 2006, pp. 929-940.

APPENDIX A

LDV Probe 3-View Drawings

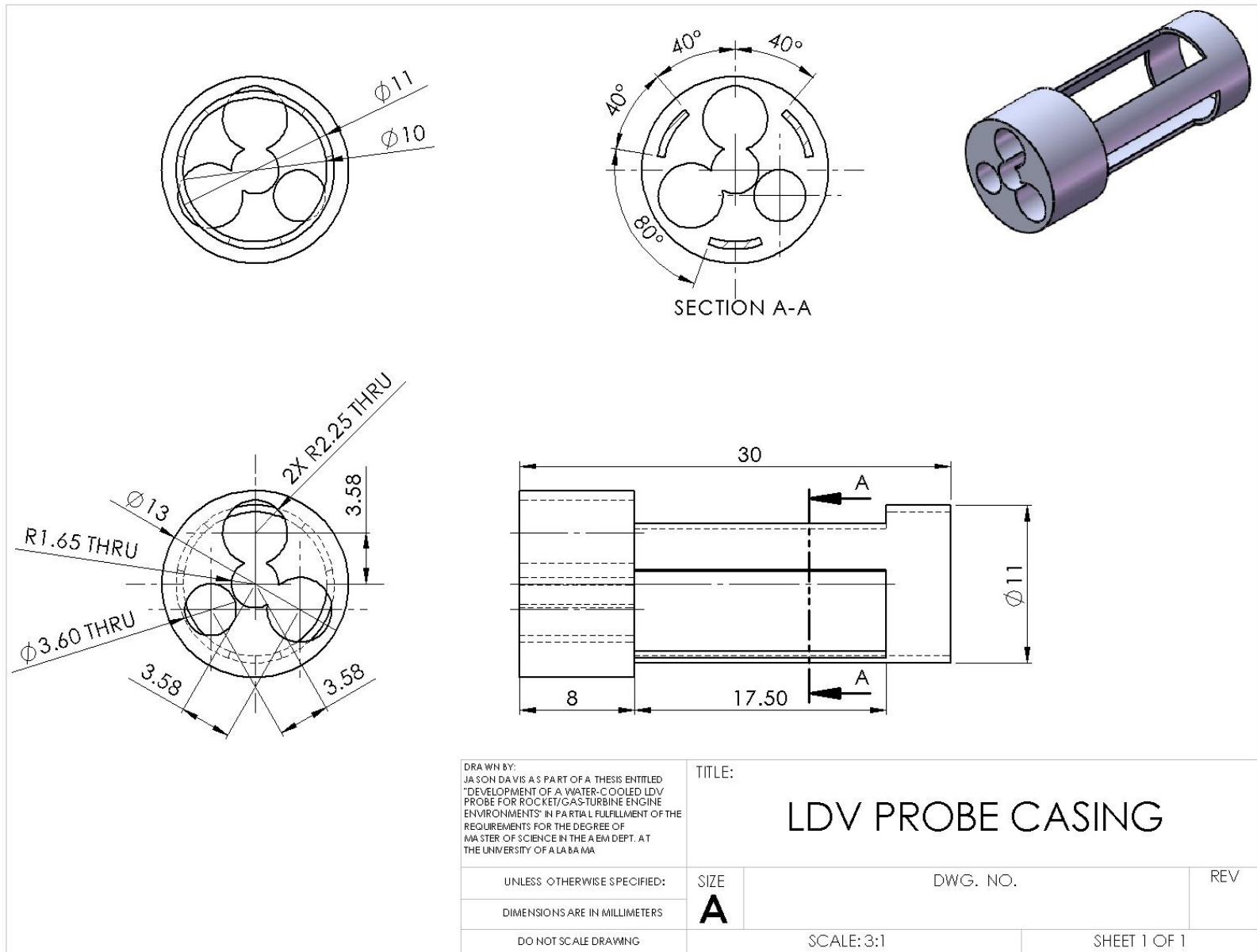


Figure 57. 3-View drawing of LDV probe casing

APPENDIX B

Water-Cooled Probe 3-View Drawings

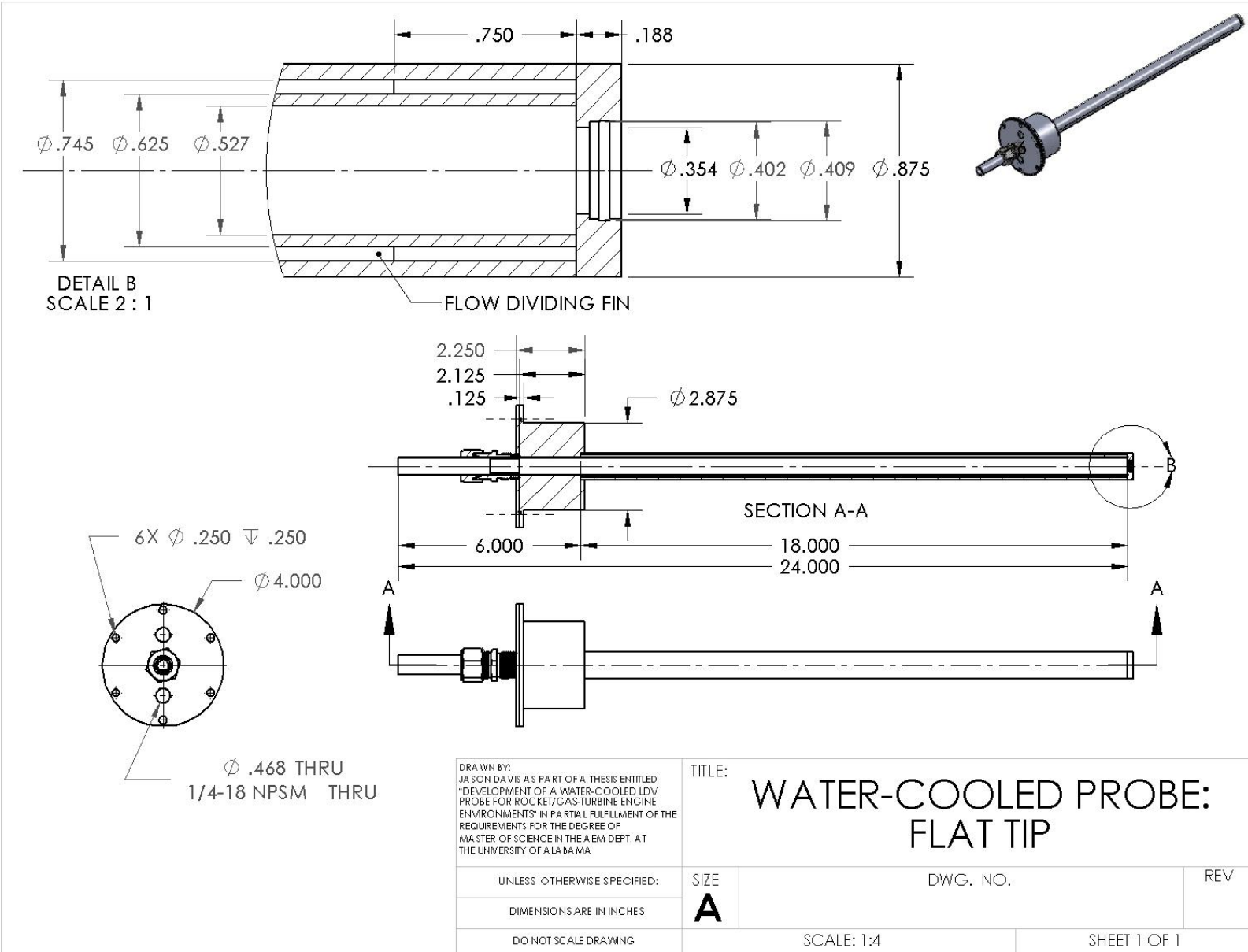


Figure 58. 3-View drawing of water-cooled probe with flat tip.

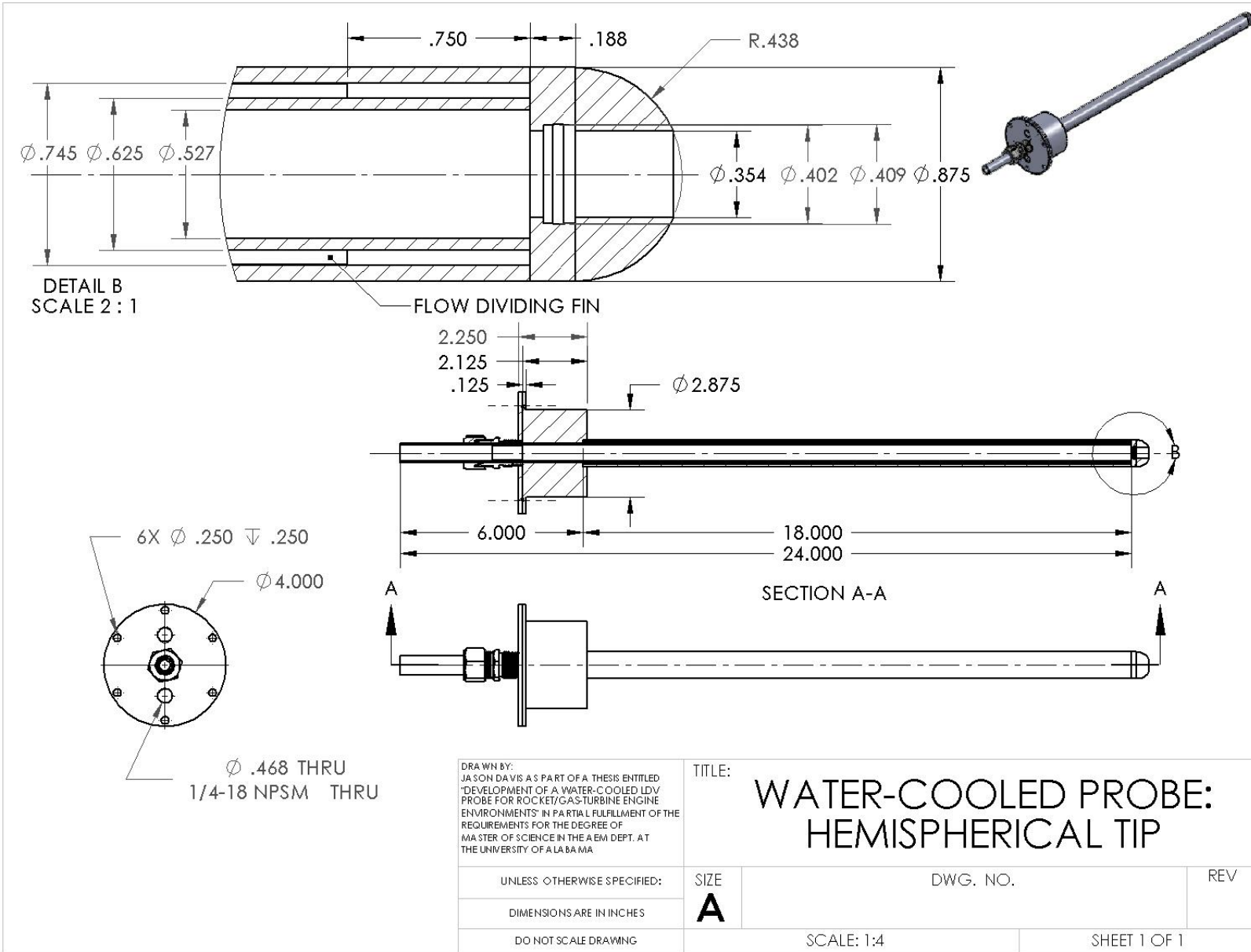


Figure 59. 3-View drawing of water-cooled probe with hemispherical tip.

APPENDIX C

Pressure Washer Specifications

Table 3. Husky-HU80911A Pressure Washer Specifications

Feature	Value	Units
Engine	Kohler Cougar XT-7	--
Fuel Tank Capacity	0.375	Gallons
Maximum Pressure	2600	psi
Maximum Flow Rate	2.4	GPM
Maximum Inlet Water Temperature	104	°F

The maximum pressure and flow rate were determined using the Pressure Washer Manufacturers' Association (PWMA) Standard 101 when tested with a 0° spray pattern nozzle. The PWMA Standard 101 is "intended to provide a uniform method for testing and rating the primary performance characteristics of pressure washers: pressure and water flow."

APPENDIX D

Flow Field Velocity and Temperature Distributions

Flow Field Velocity Distributions

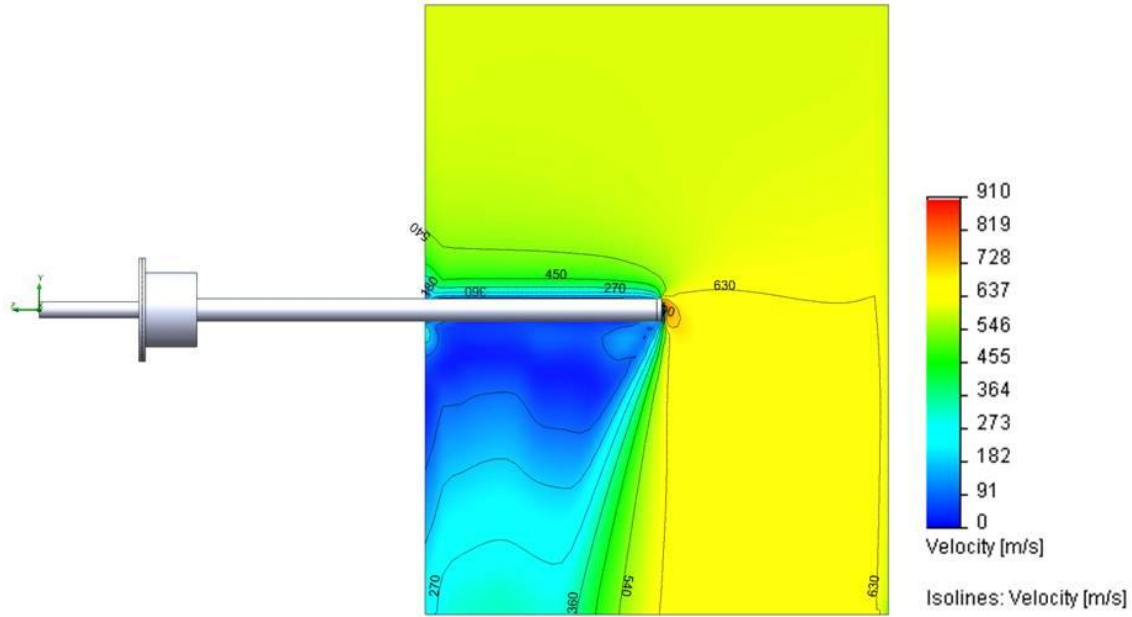


Figure 60. Velocity distribution for Mach 0.7 augmentor flow with flat tip probe insertion of 50%.

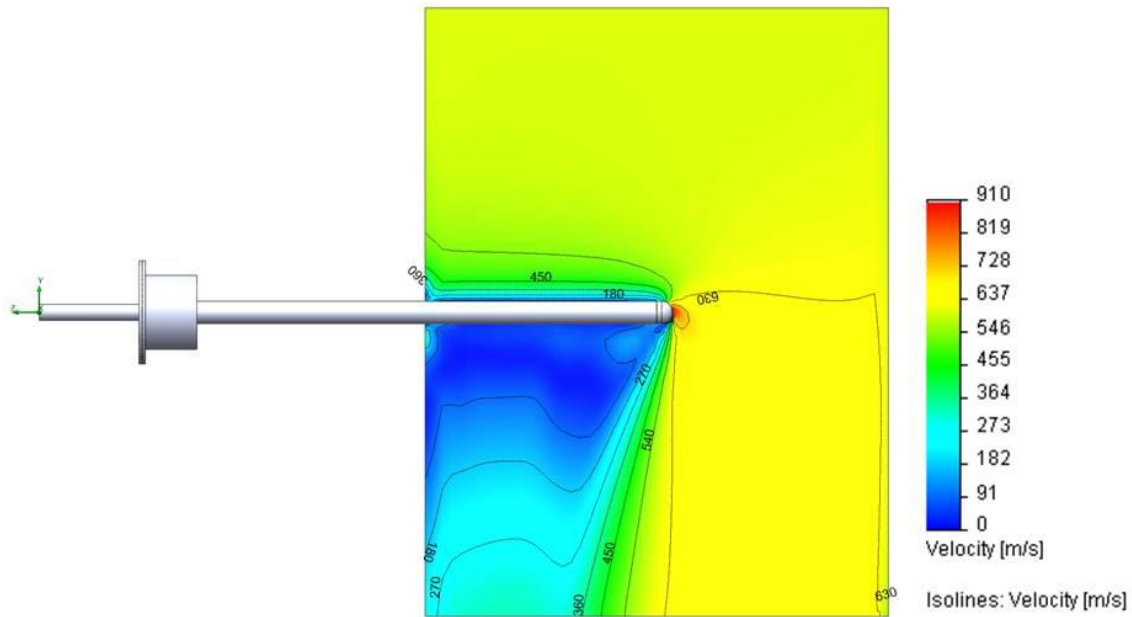


Figure 61. Velocity distribution for Mach 0.7 augmentor flow with hemispherical tip probe insertion of 50%.

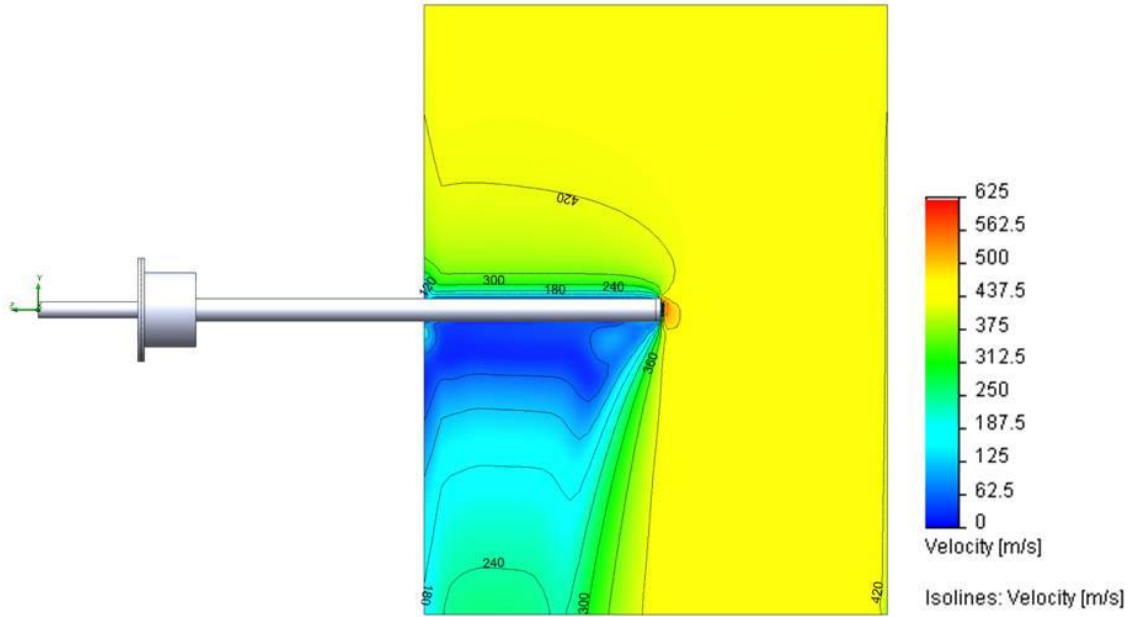


Figure 62. Velocity distribution for Mach 0.5 augmentor flow with flat tip probe insertion of 50%.

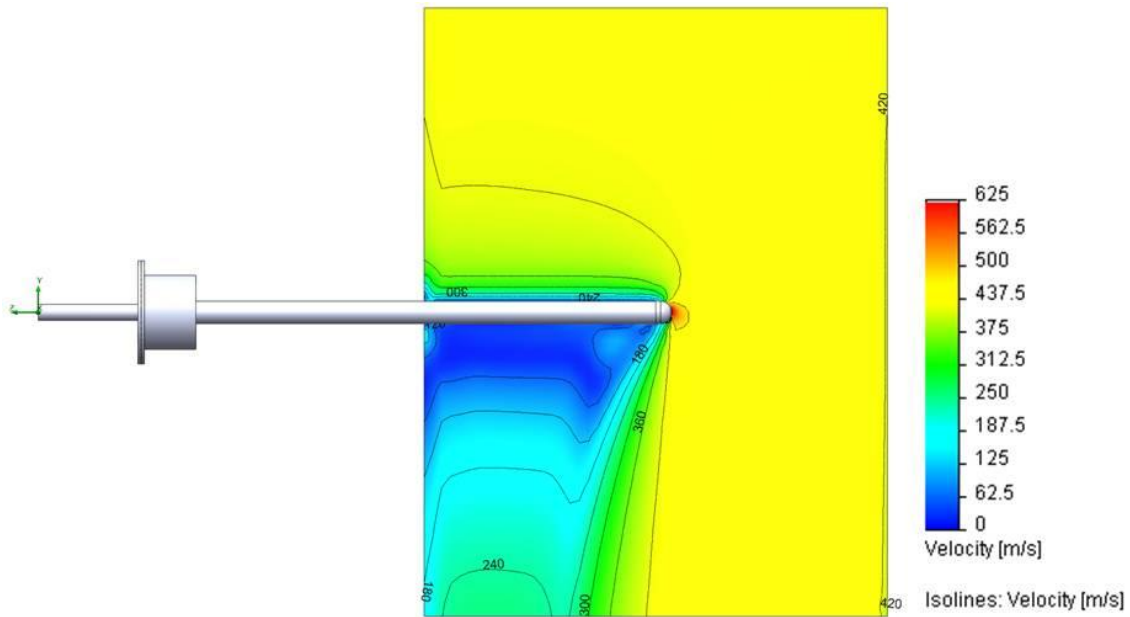


Figure 63. Velocity distribution for Mach 0.5 augmentor flow with hemispherical tip probe insertion of 50%.

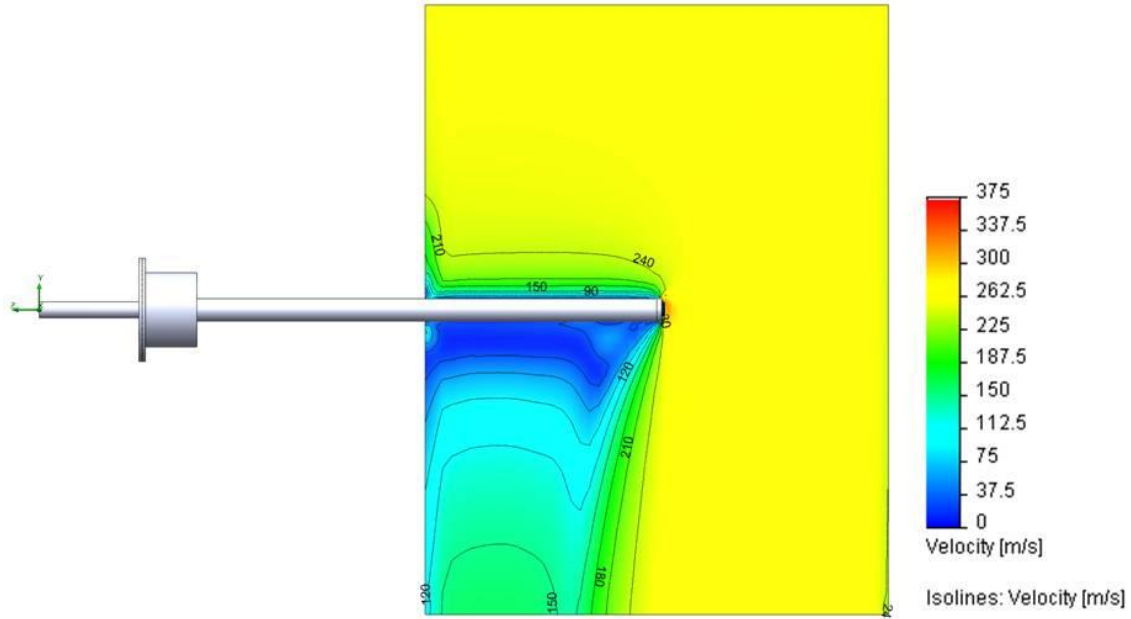


Figure 64. Velocity distribution for Mach 0.3 augmentor flow with flat tip probe insertion of 50%.

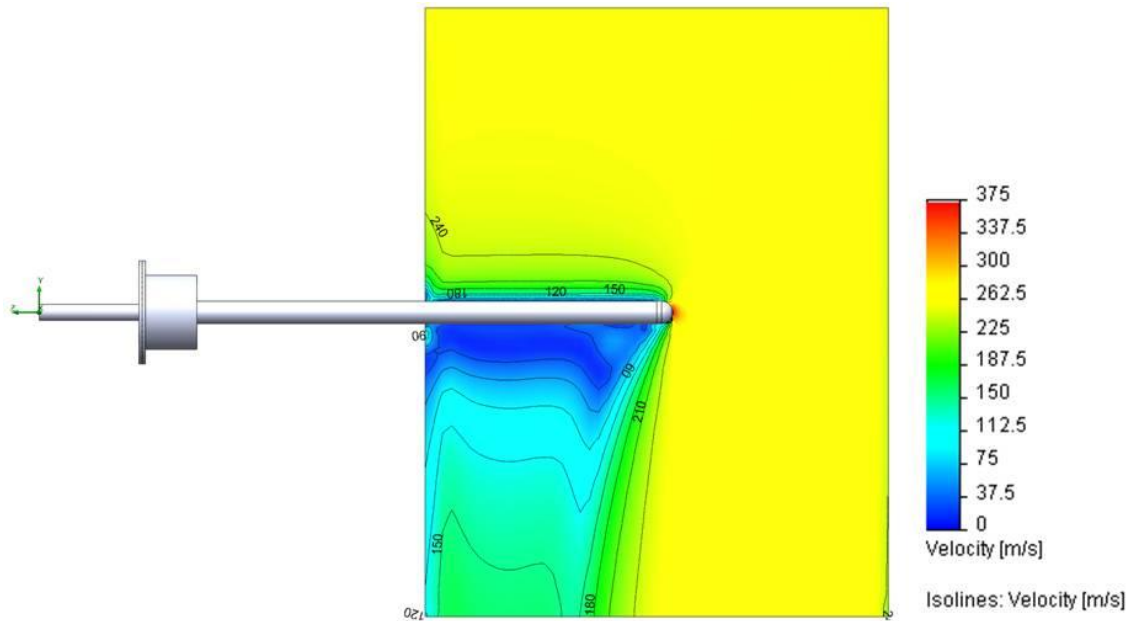


Figure 65. Velocity distribution for Mach 0.3 augmentor flow with hemispherical tip probe insertion of 50%.

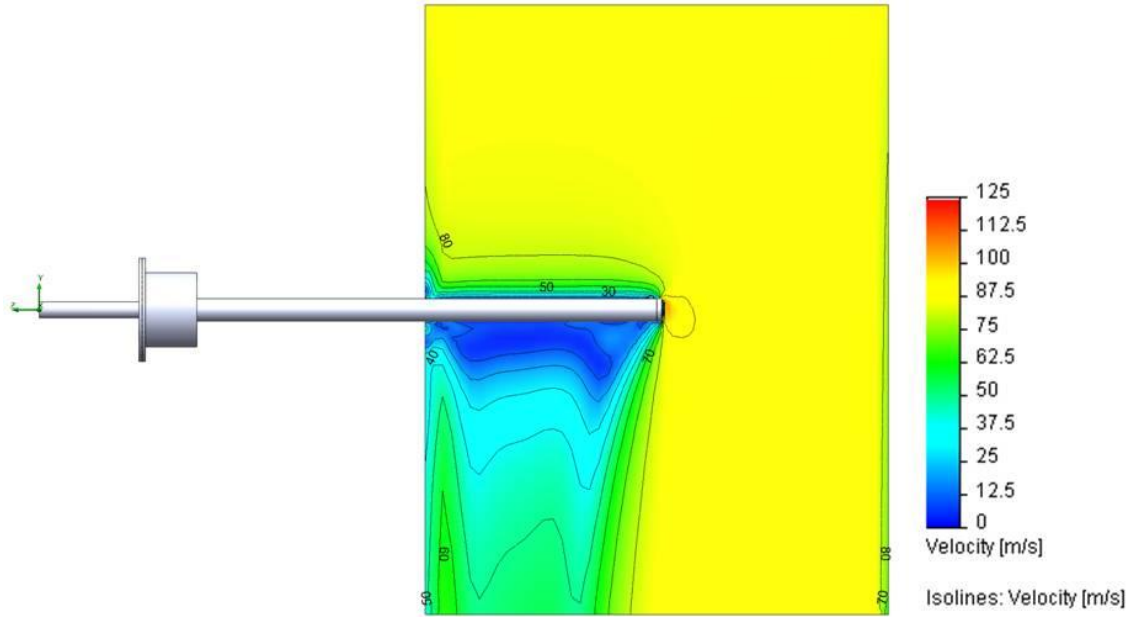


Figure 66. Velocity distribution for Mach 0.1 augmentor flow with flat tip probe insertion of 50%.

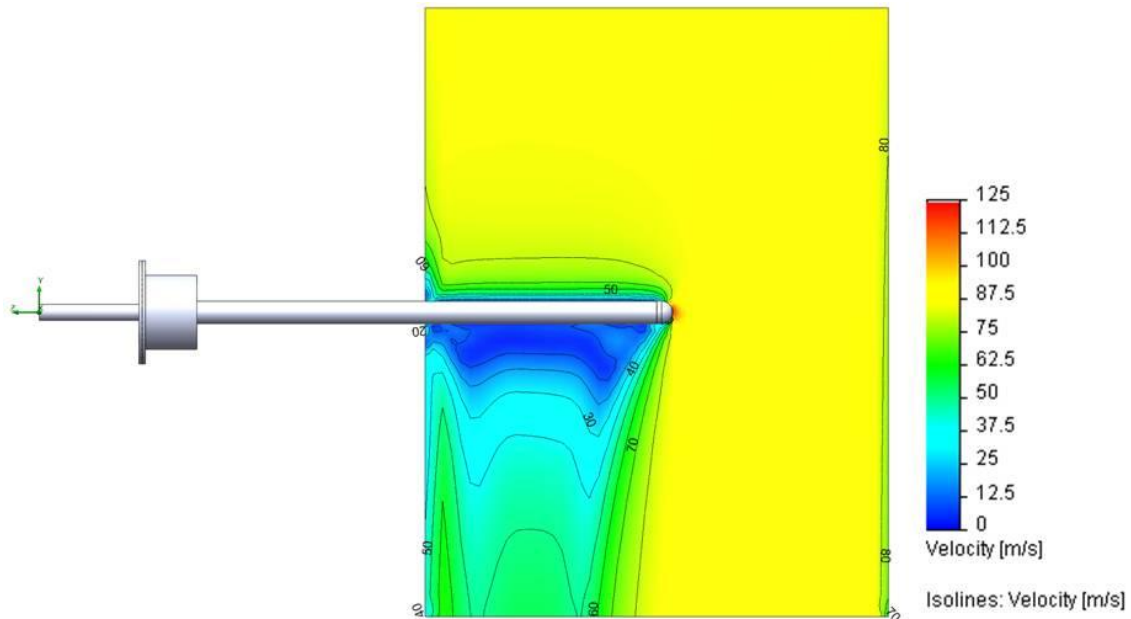


Figure 67. Velocity distribution for Mach 0.1 augmentor flow with hemispherical tip probe insertion of 50%.

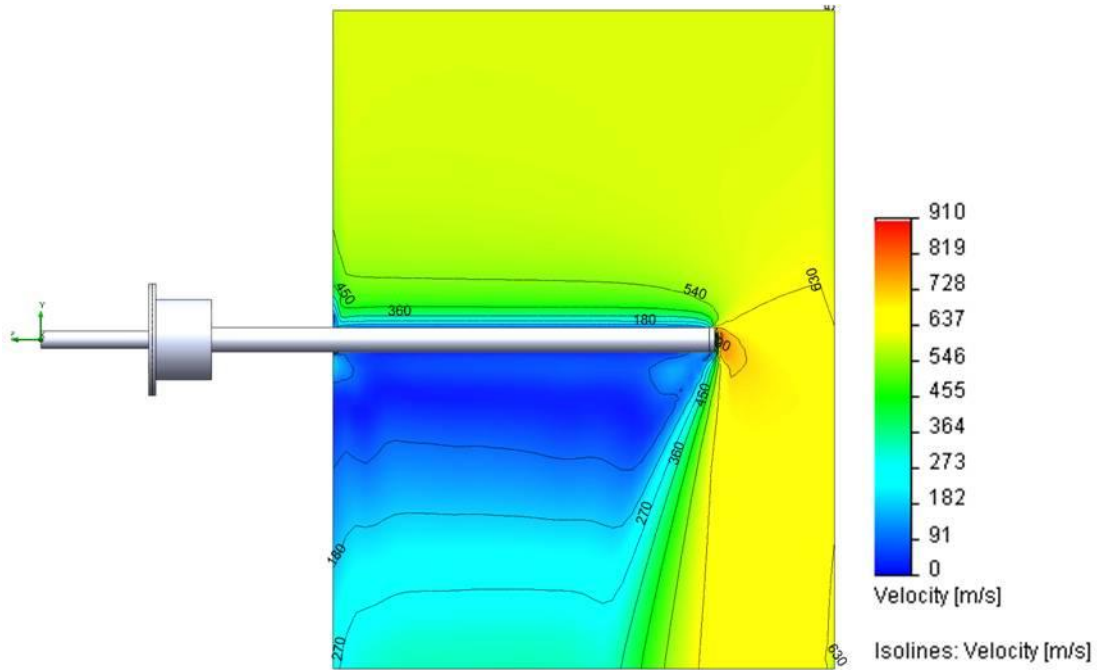


Figure 68. Velocity distribution for Mach 0.7 augmentor flow with flat tip probe insertion of 75%.

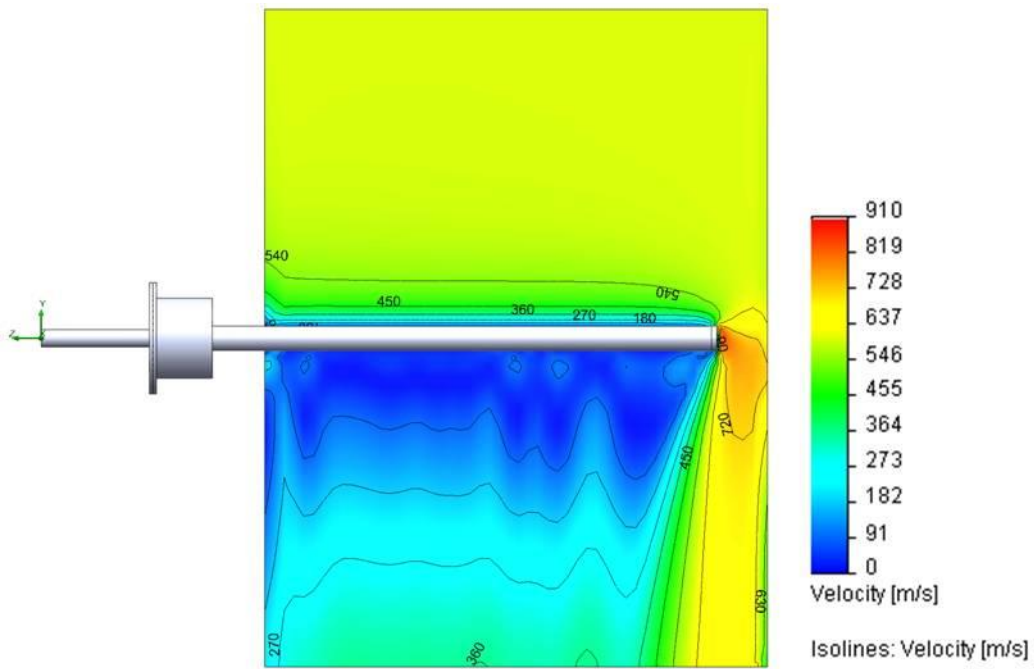


Figure 69. Velocity distribution for Mach 0.7 augmentor flow with flat tip probe insertion of 88.9%.

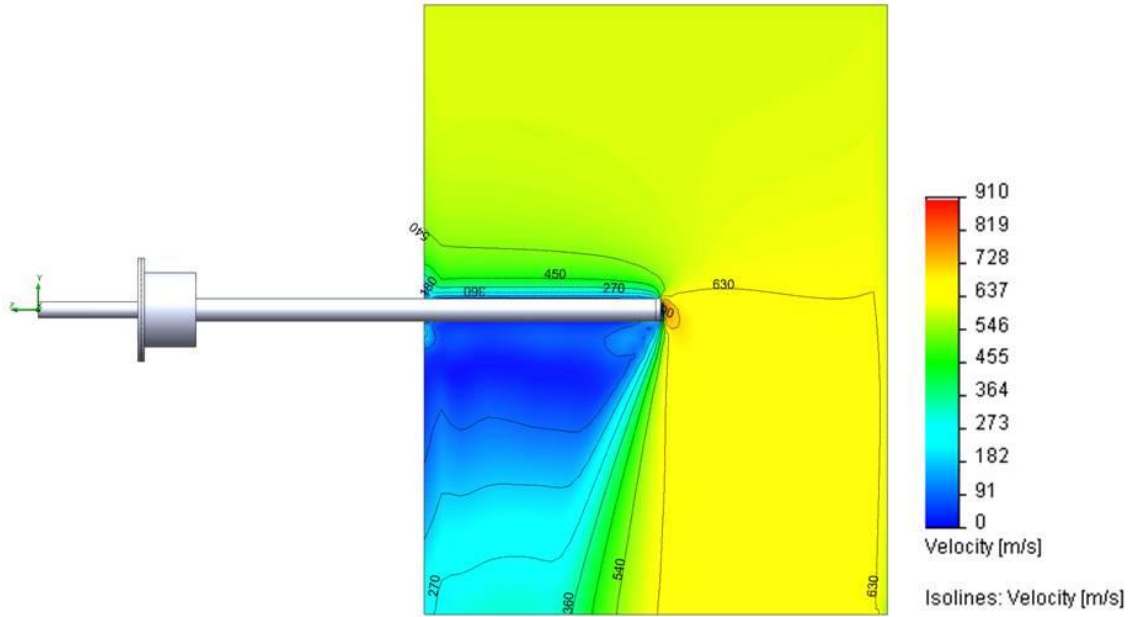


Figure 70. Velocity distribution for Mach 0.7 augmentor flow with flat tip probe insertion of 50%—No water.

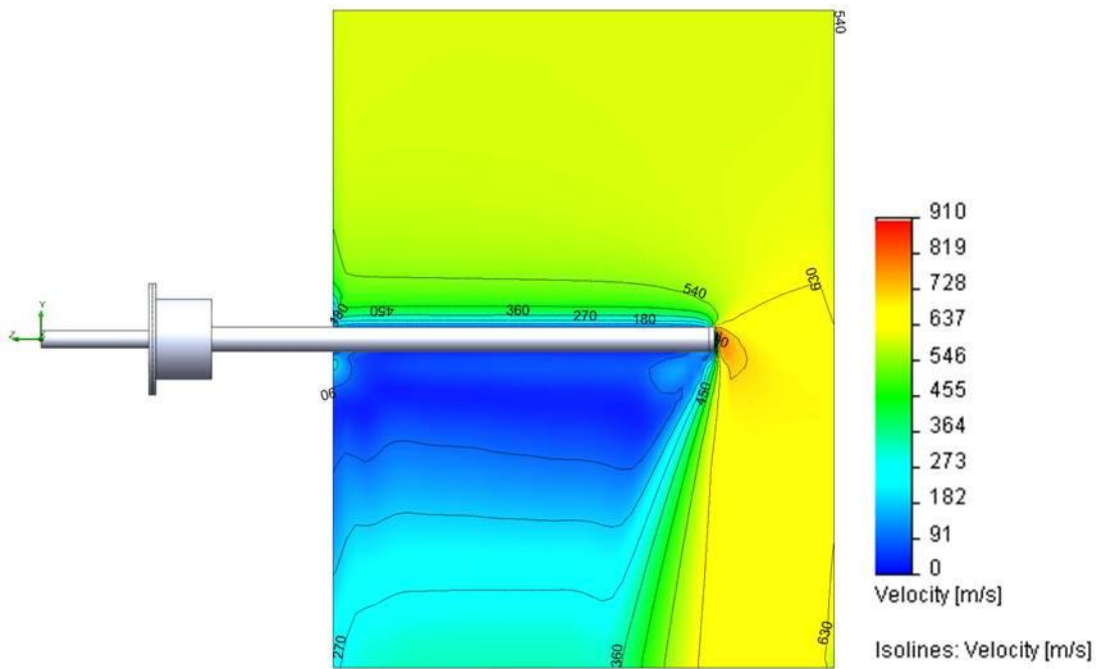


Figure 71. Velocity distribution for Mach 0.7 augmentor flow with flat tip probe insertion of 75%—No water.

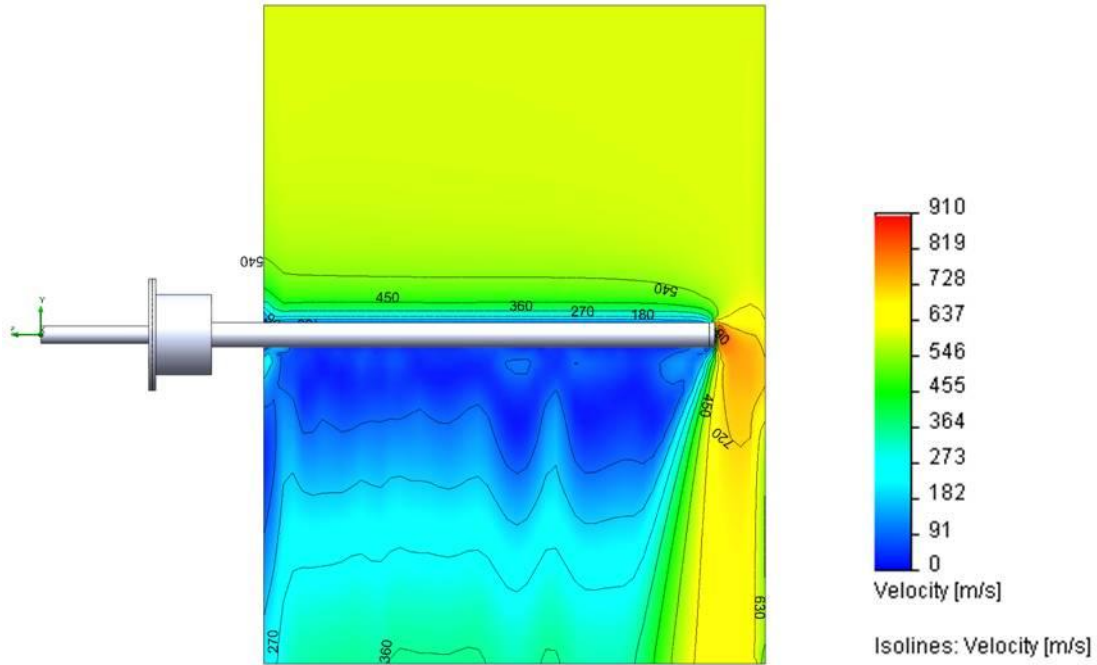


Figure 72. Velocity distribution for Mach 0.7 augmentor flow with flat tip probe insertion of 88.9%—No water.

Flow Field Temperature Distributions

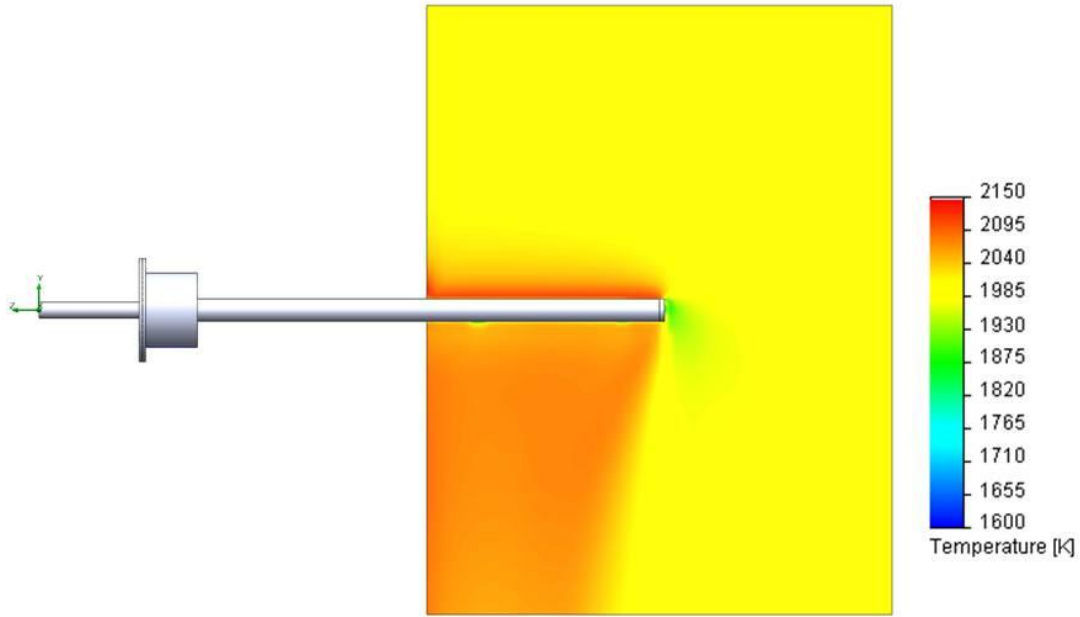


Figure 73. Temperature distribution for Mach 0.7 augmentor flow with flat tip probe insertion of 50%.

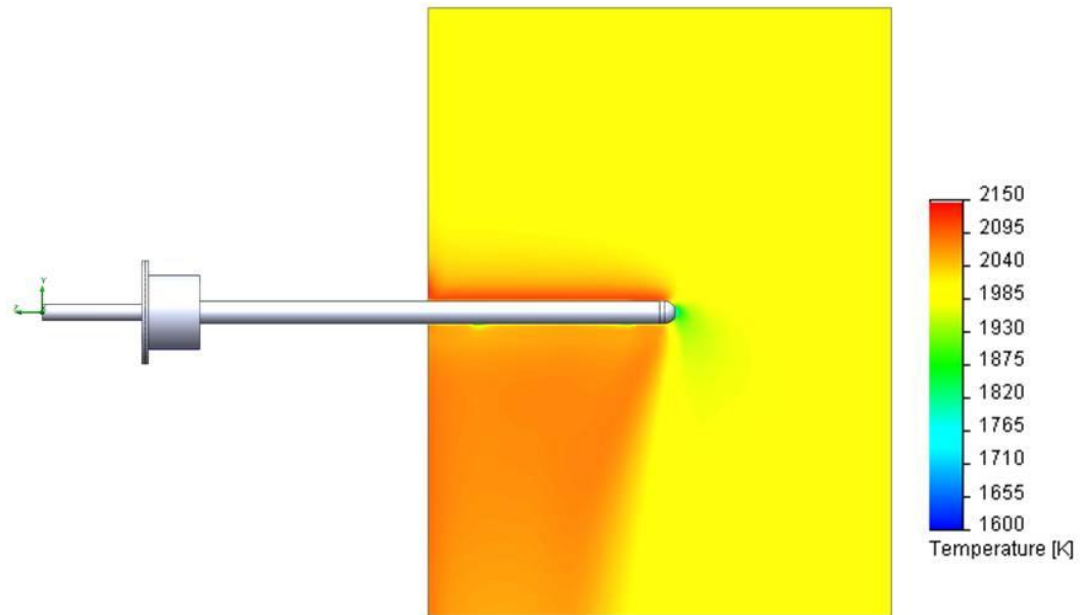


Figure 74. Temperature distribution for Mach 0.7 augmentor flow with hemispherical tip probe insertion of 50%.

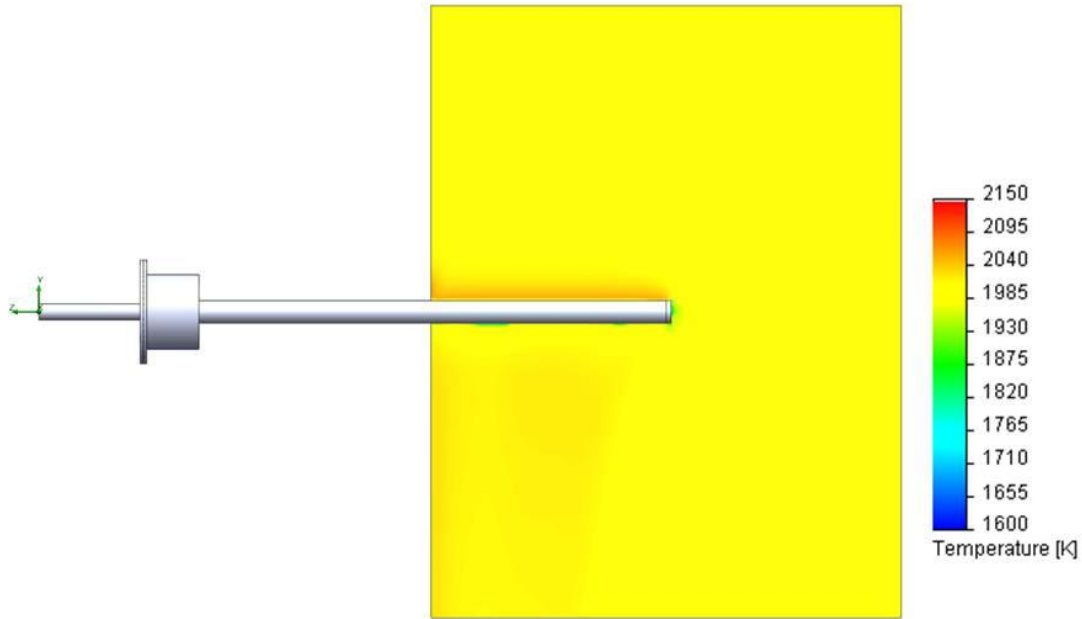


Figure 75. Temperature distribution for Mach 0.5 augmentor flow with flat tip probe insertion of 50%.

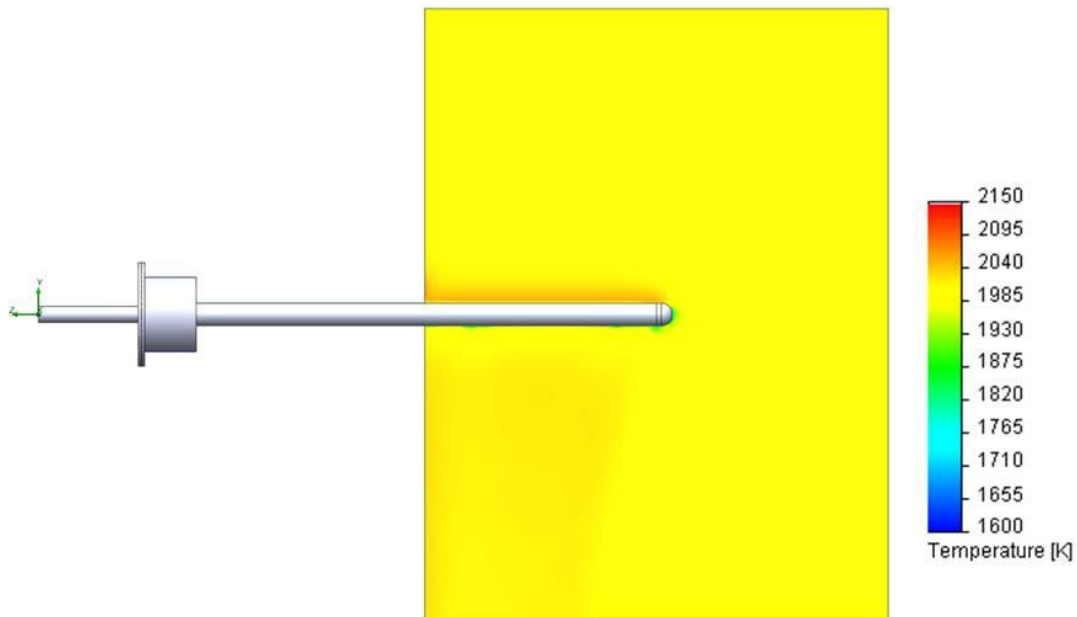


Figure 76. Temperature distribution for Mach 0.5 augmentor flow with hemispherical tip probe insertion of 50%.

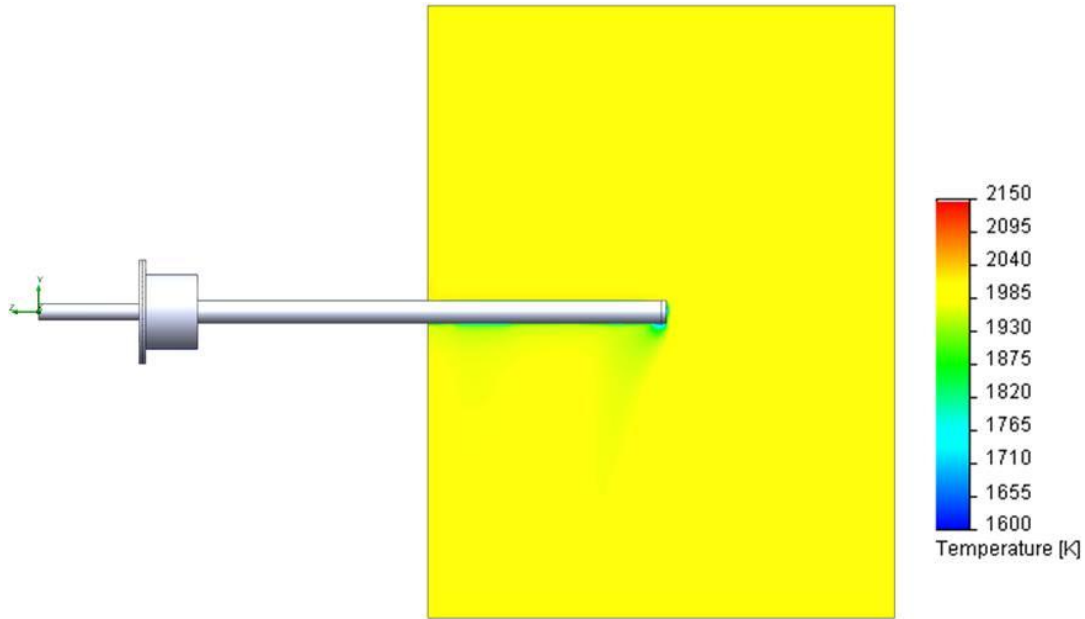


Figure 77. Temperature distribution for Mach 0.3 augmentor flow with flat tip probe insertion of 50%.

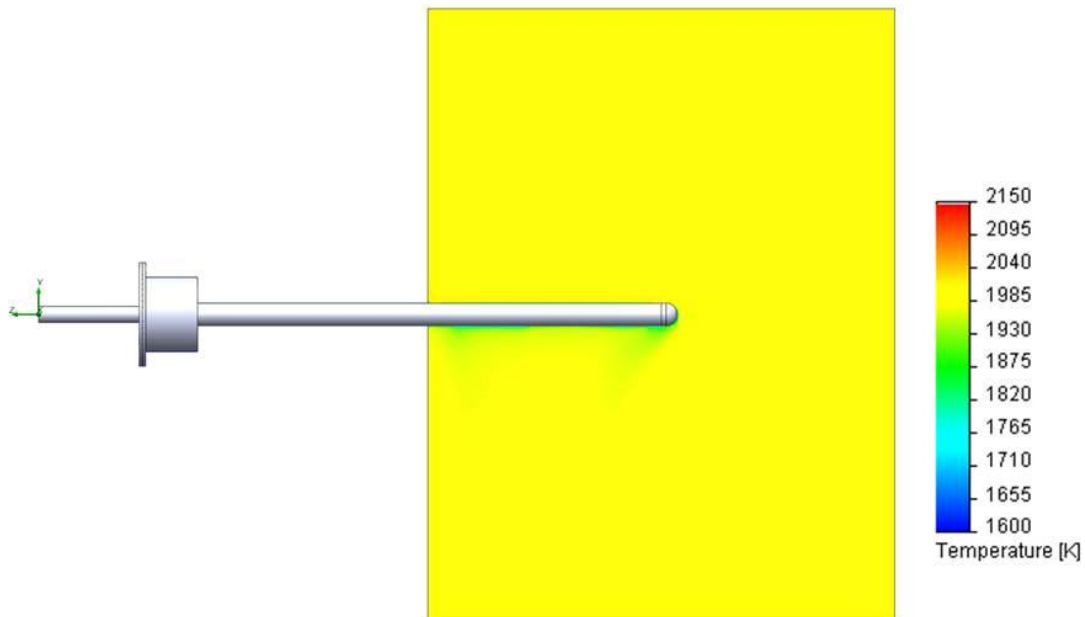


Figure 78. Temperature distribution for Mach 0.3 augmentor flow with hemispherical tip probe insertion of 50%.

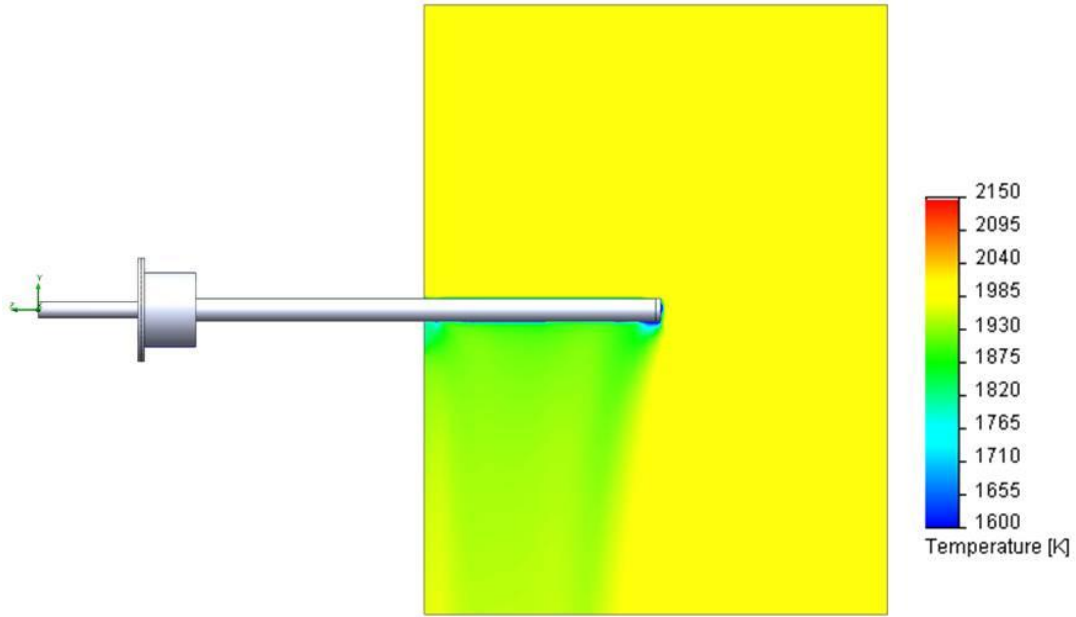


Figure 79. Temperature distribution for Mach 0.1 augmentor flow with flat tip probe insertion of 50%.

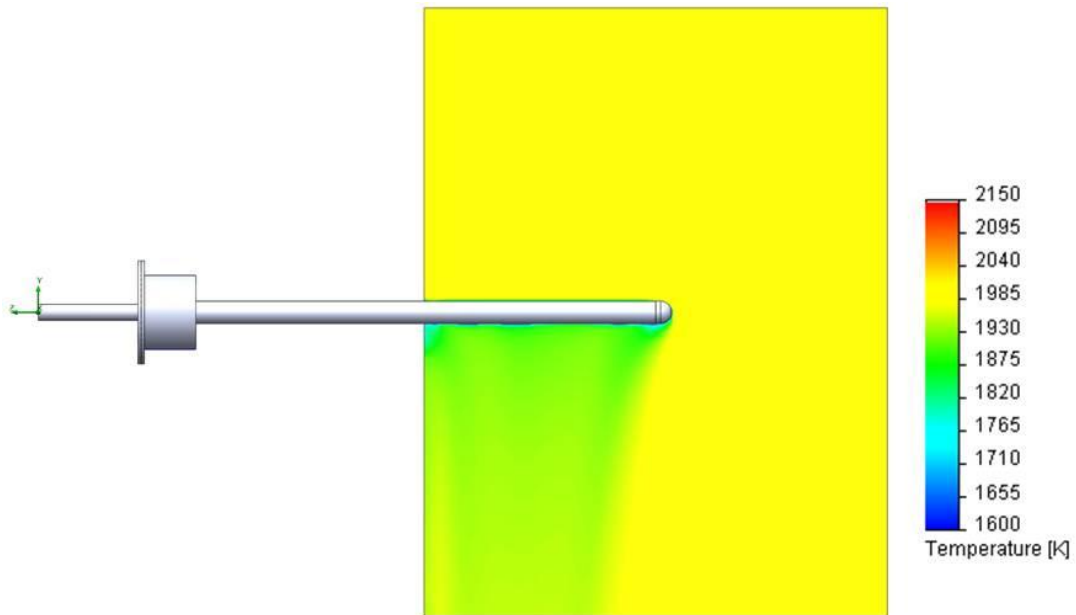


Figure 80. Temperature distribution for Mach 0.1 augmentor flow with hemispherical tip probe insertion of 50%.

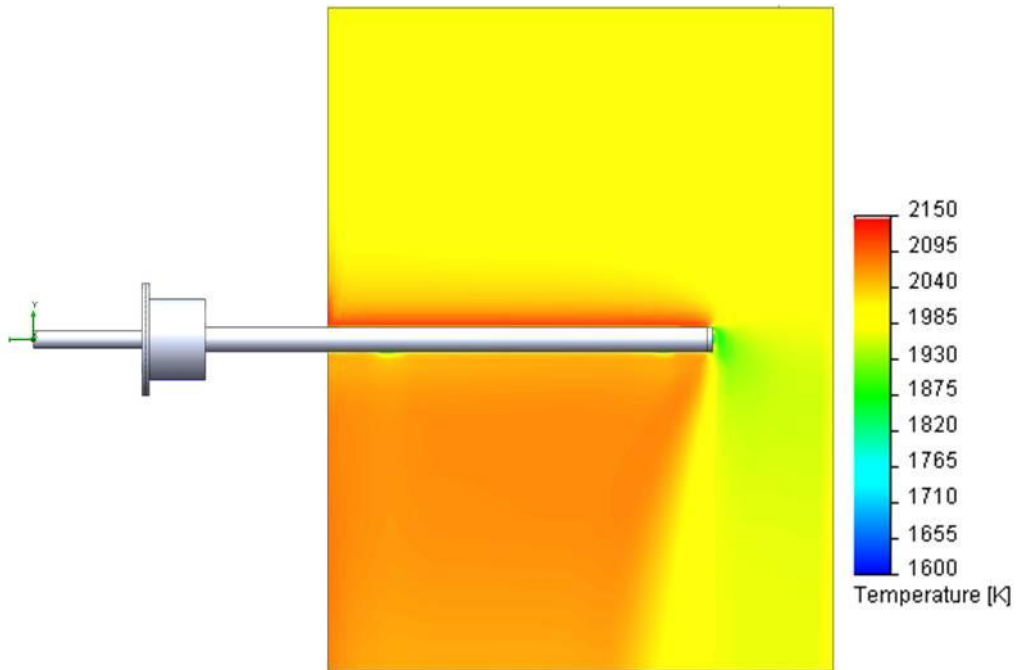


Figure 81. Temperature distribution for Mach 0.7 augmentor flow with flat tip probe insertion of 75%.

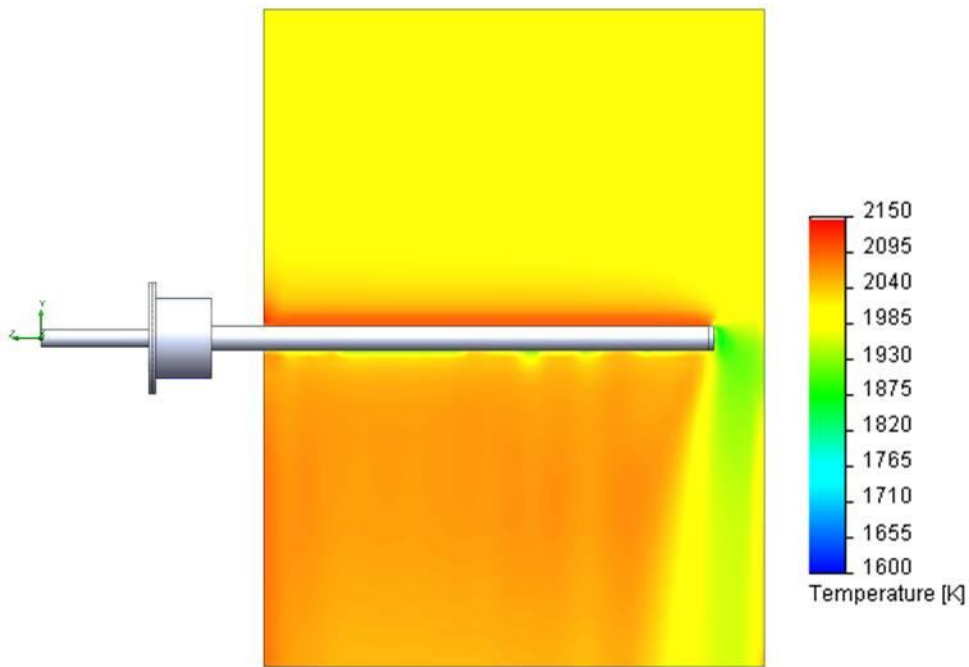


Figure 82. Temperature distribution for Mach 0.7 augmentor flow with flat tip probe insertion of 88.9%.

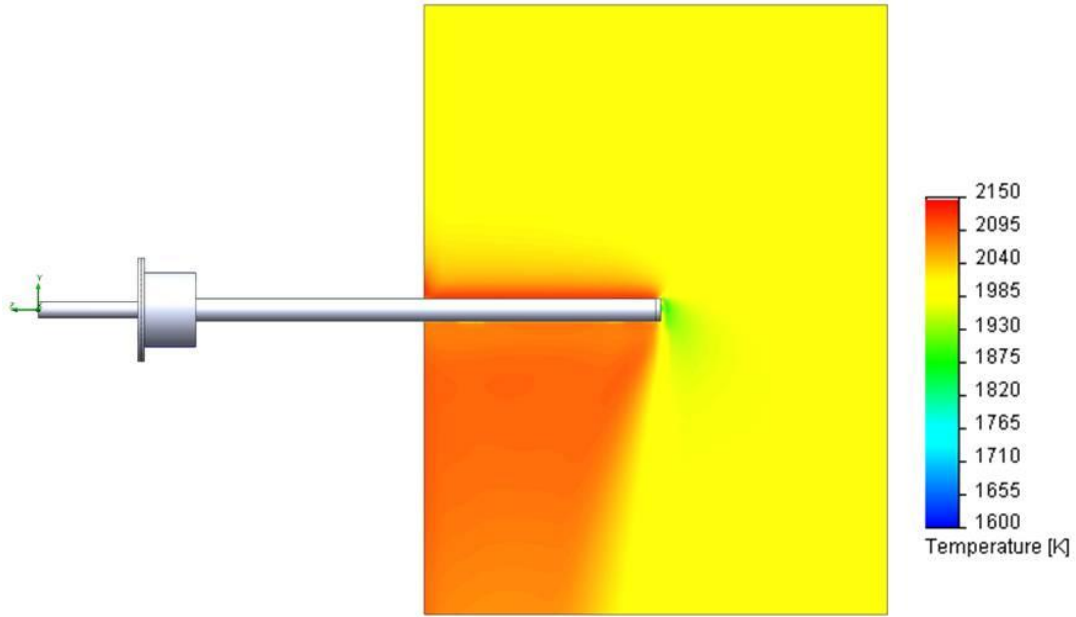


Figure 83. Temperature distribution for Mach 0.7 augmentor flow with flat tip probe insertion of 50%—No water.

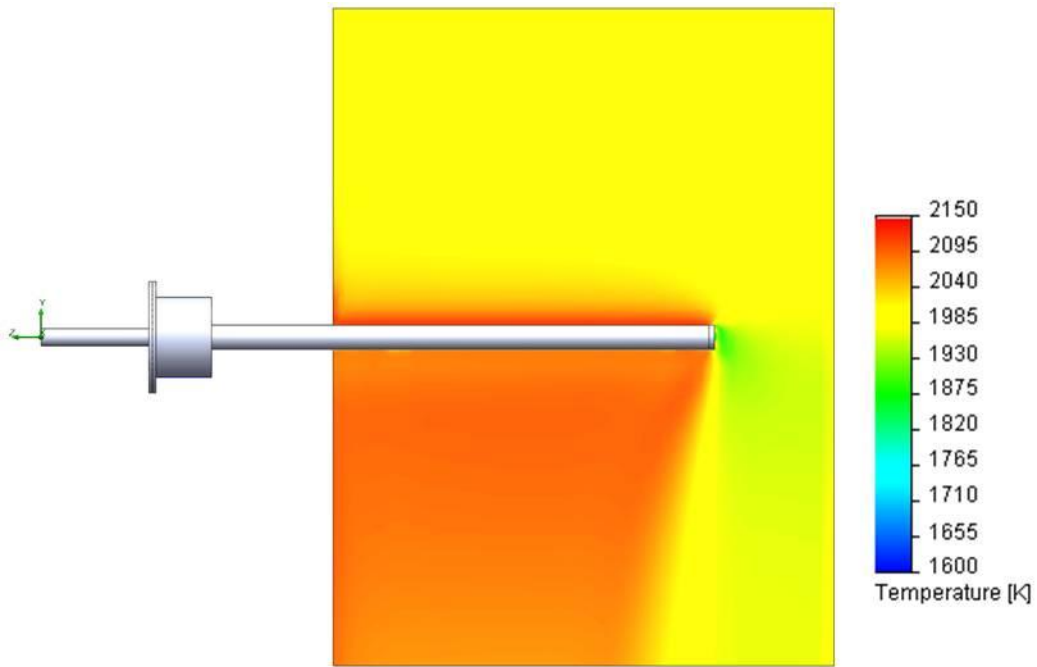


Figure 84. Temperature distribution for Mach 0.7 augmentor flow with flat tip probe insertion of 75%—No water.

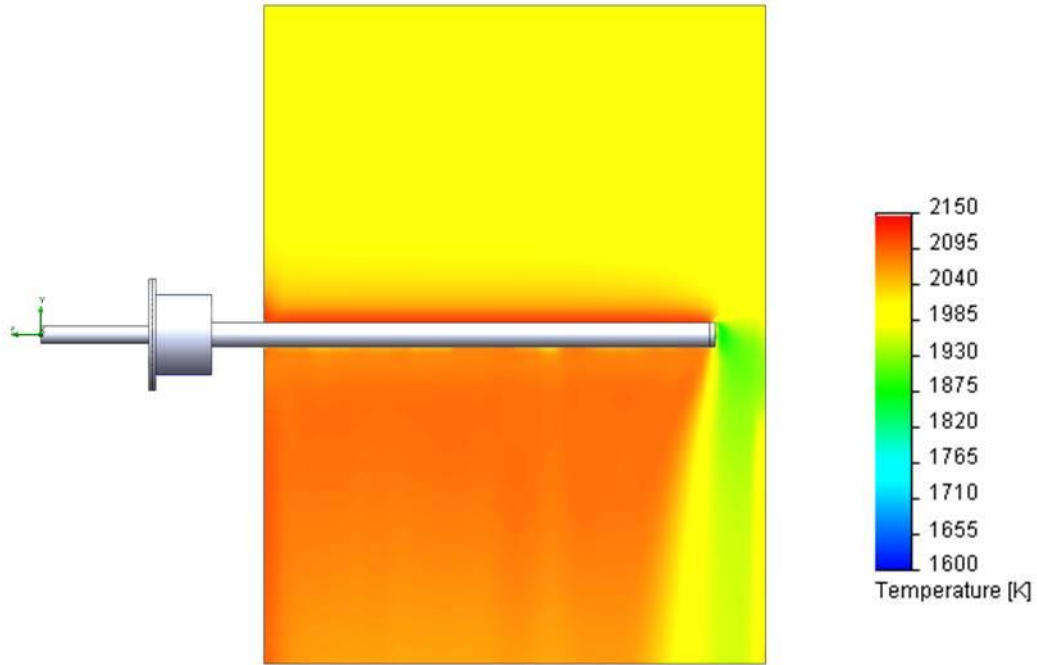


Figure 85. Temperature distribution for Mach 0.7 augmentor flow with flat tip probe insertion of 88.9%—No water.

APPENDIX E

Magnified Probe Tip Temperature Distribution

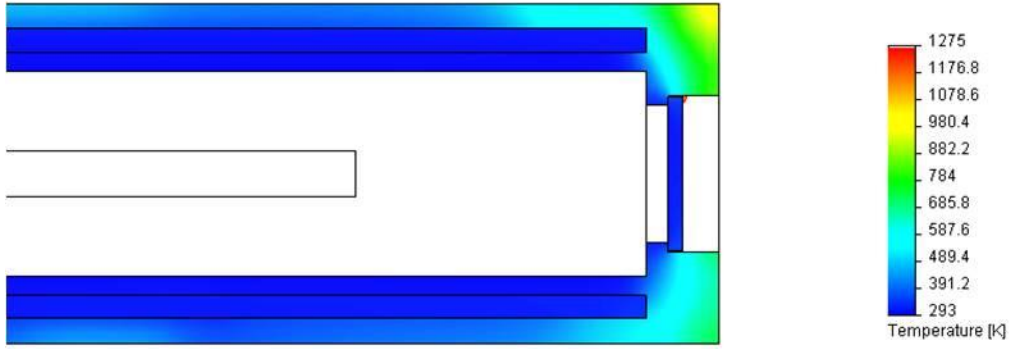


Figure 86. Magnified tip temperature distribution for Mach 0.7 augmentor flow with flat tip probe insertion of 50%.

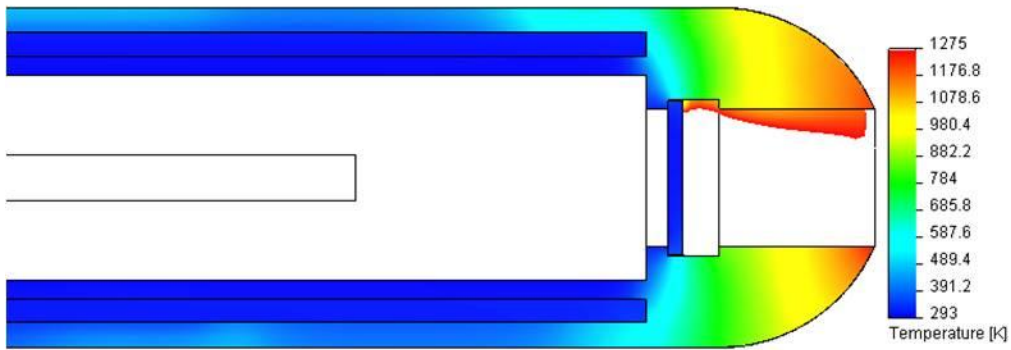


Figure 87. Magnified tip temperature distribution for Mach 0.7 augmentor flow with hemispherical tip probe insertion of 50%.

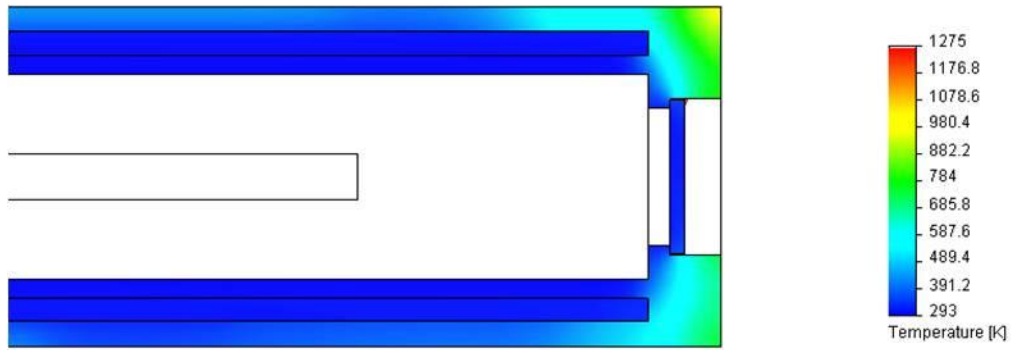


Figure 88. Magnified tip temperature distribution for Mach 0.5 augmentor flow with flat tip probe insertion of 50%.

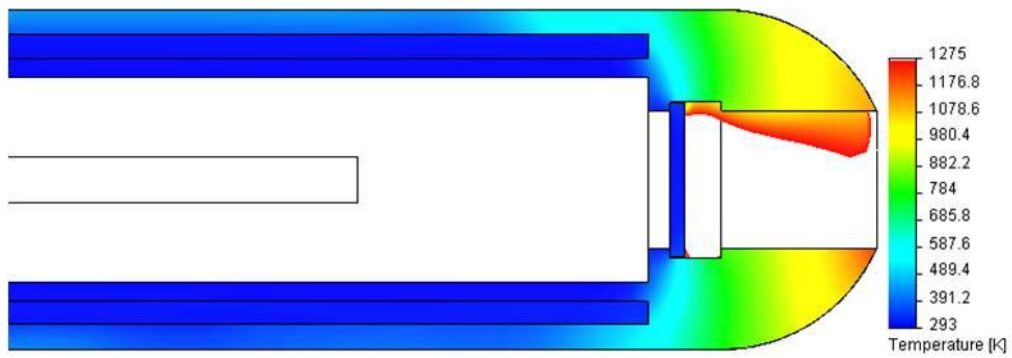


Figure 89. Magnified tip temperature distribution for Mach 0.5 augmentor flow with hemispherical tip probe insertion of 50%.

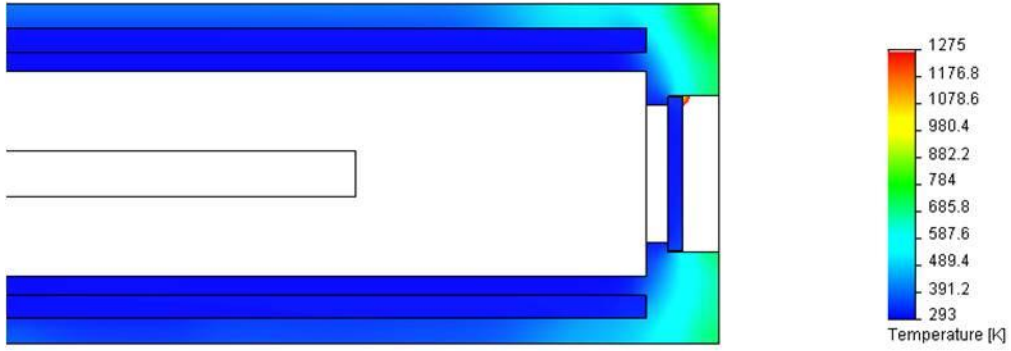


Figure 90. Magnified tip temperature distribution for Mach 0.3 augmentor flow with flat tip probe insertion of 50%.

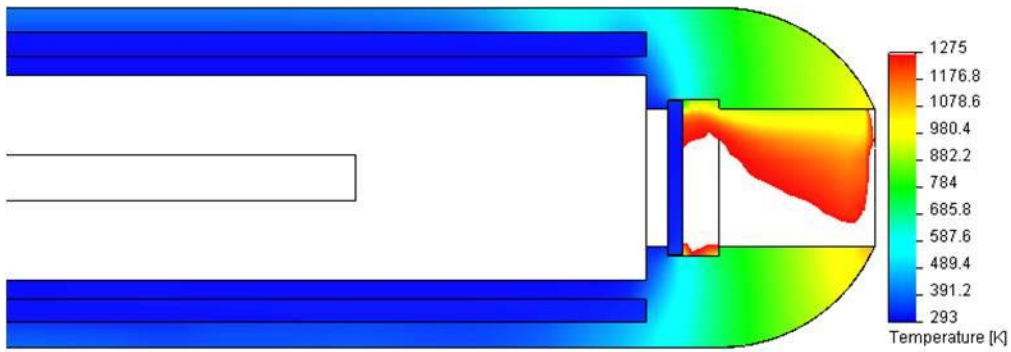


Figure 91. Magnified tip temperature distribution for Mach 0.3 augmentor flow with hemispherical tip probe insertion of 50%.

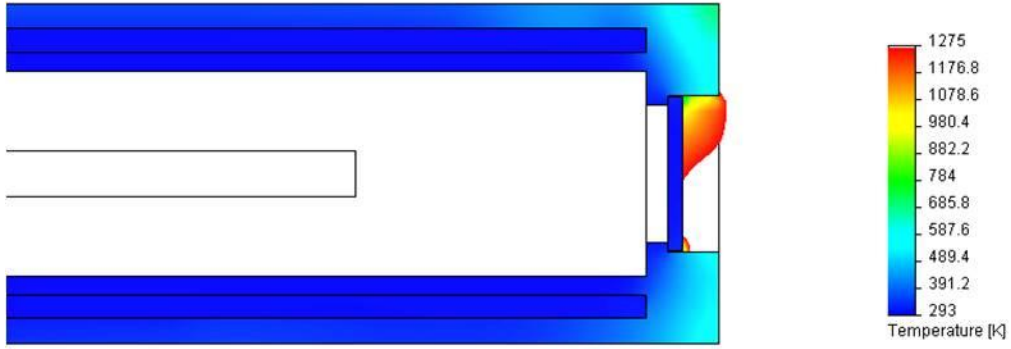


Figure 92. Magnified tip temperature distribution for Mach 0.1 augmentor flow with flat tip probe insertion of 50%.

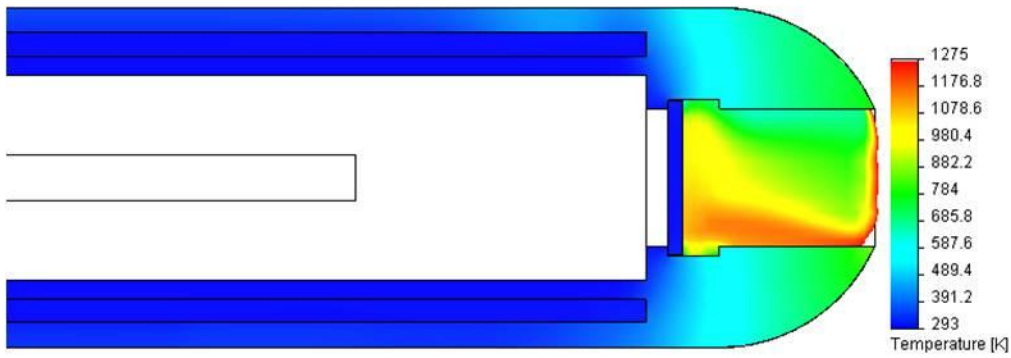


Figure 93. Magnified tip temperature distribution for Mach 0.1 augmentor flow with hemispherical tip probe insertion of 50%.

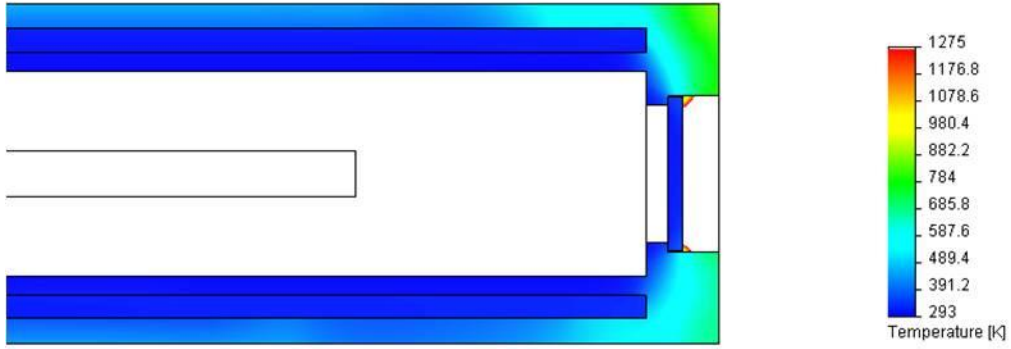


Figure 94. Magnified tip temperature distribution for Mach 0.7 augmentor flow with flat tip probe insertion of 75%.

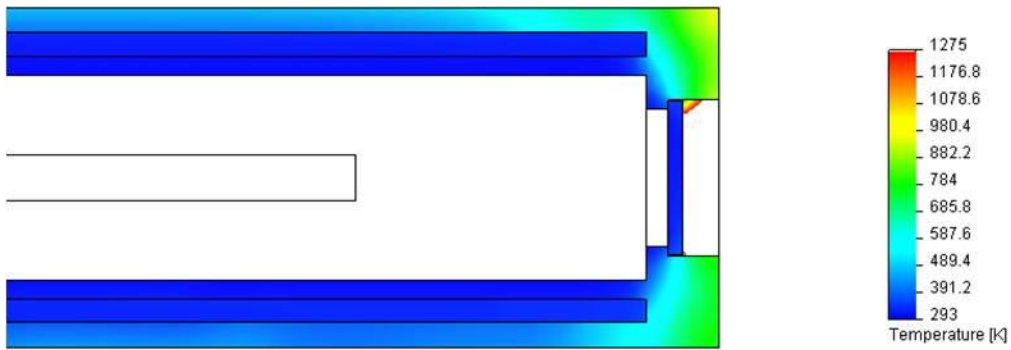


Figure 95. Magnified tip temperature distribution for Mach 0.7 augmentor flow with flat tip probe insertion of 88.9%.

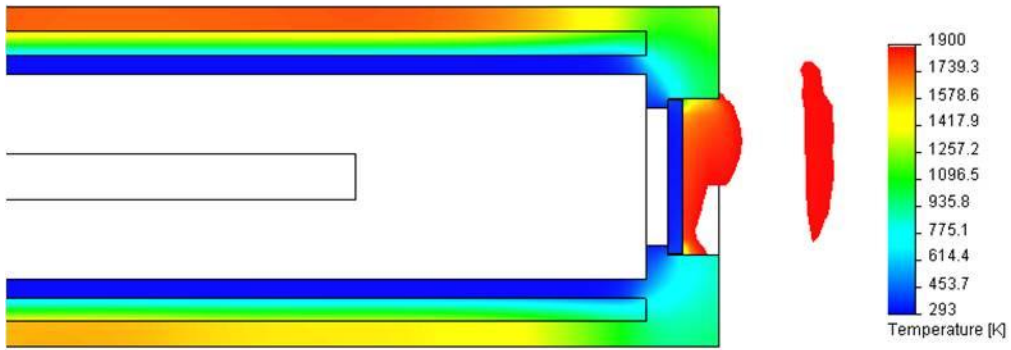


Figure 96. Magnified tip temperature distribution for Mach 0.7 augmentor flow with flat tip probe insertion of 50%—No water.

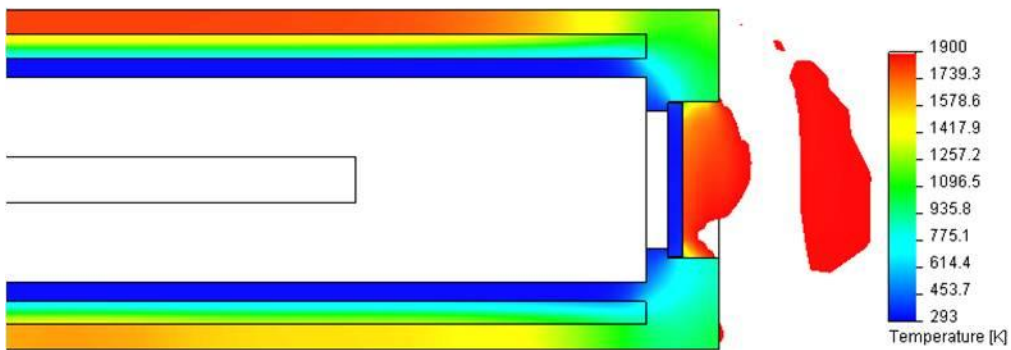


Figure 97. Magnified tip temperature distribution for Mach 0.7 augmentor flow with flat tip probe insertion of 75%—No water.

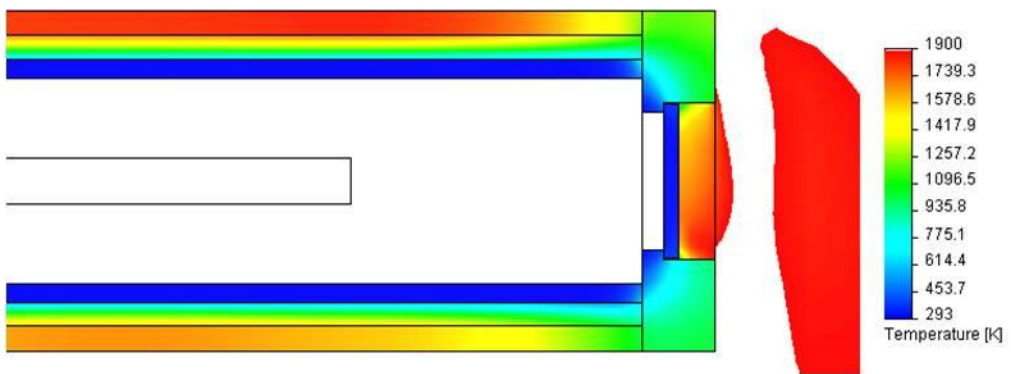


Figure 98. Magnified tip temperature distribution for Mach 0.7 augmentor flow with flat tip probe insertion of 88.9%—No water.

APPENDIX F

Temperature and Fluid Temperature Distributions of Probe Cut-Planes

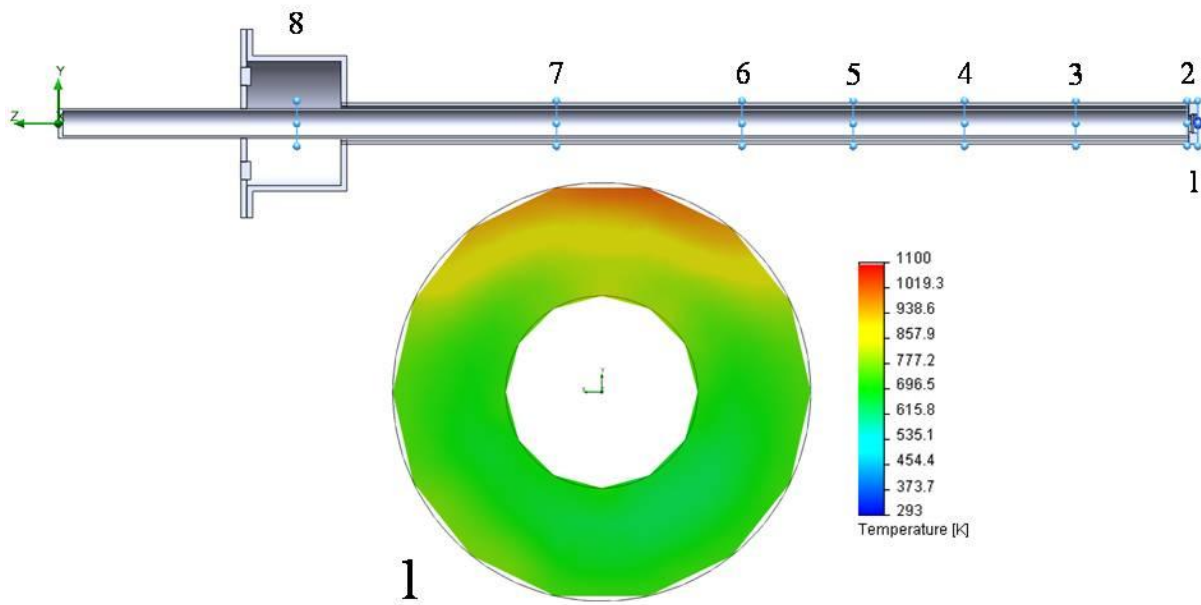


Figure 99. Plane locations along jacket length (top). Temperature distribution for probe insertion of 50% at Mach 0.7 with flat tip at Plane 1 (bottom).

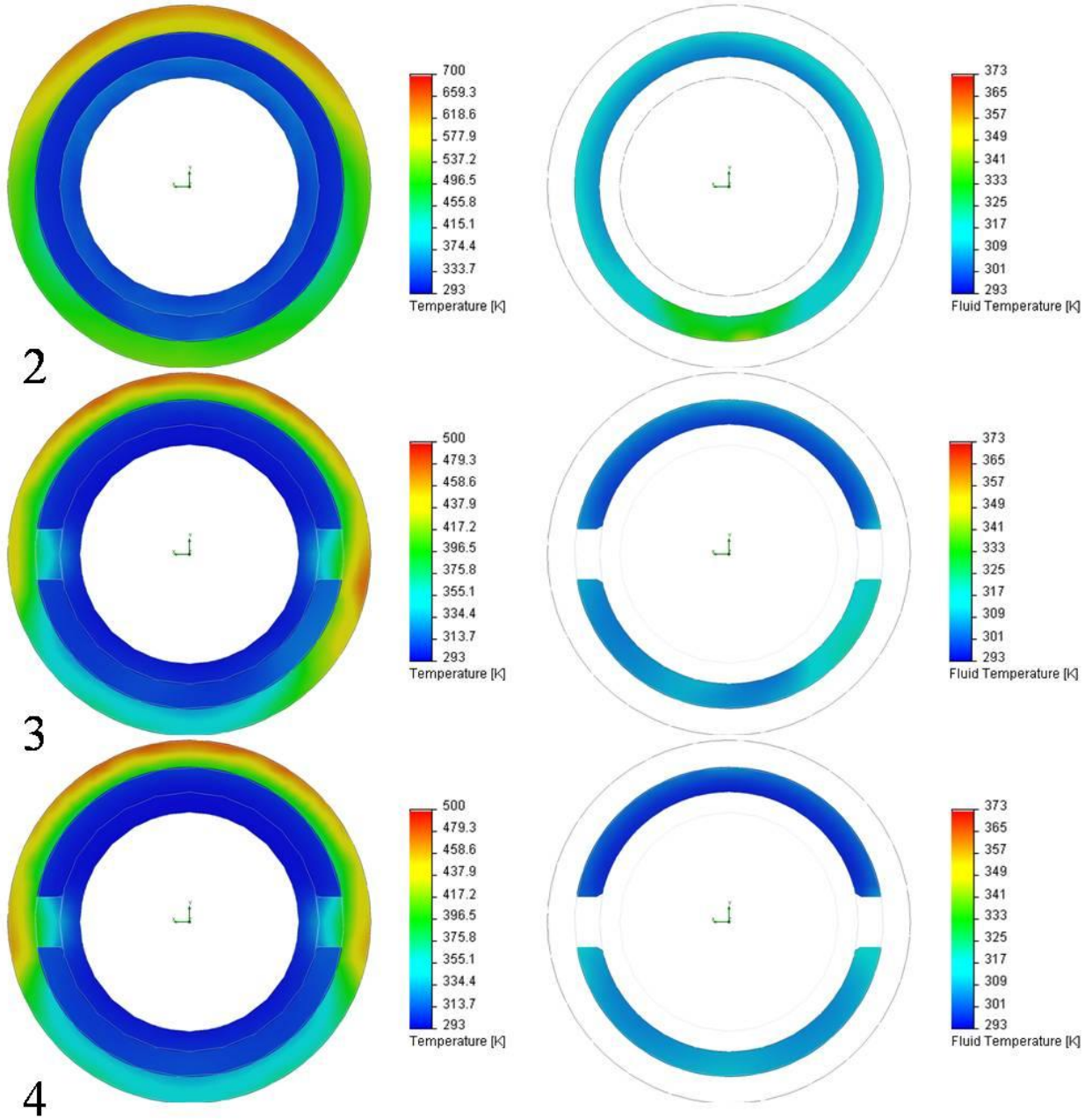


Figure 100. Temperature (left) and Fluid Temperature (right) distributions for probe insertion of 50% at Mach 0.7 with flat tip at Planes 2, 3, and 4.

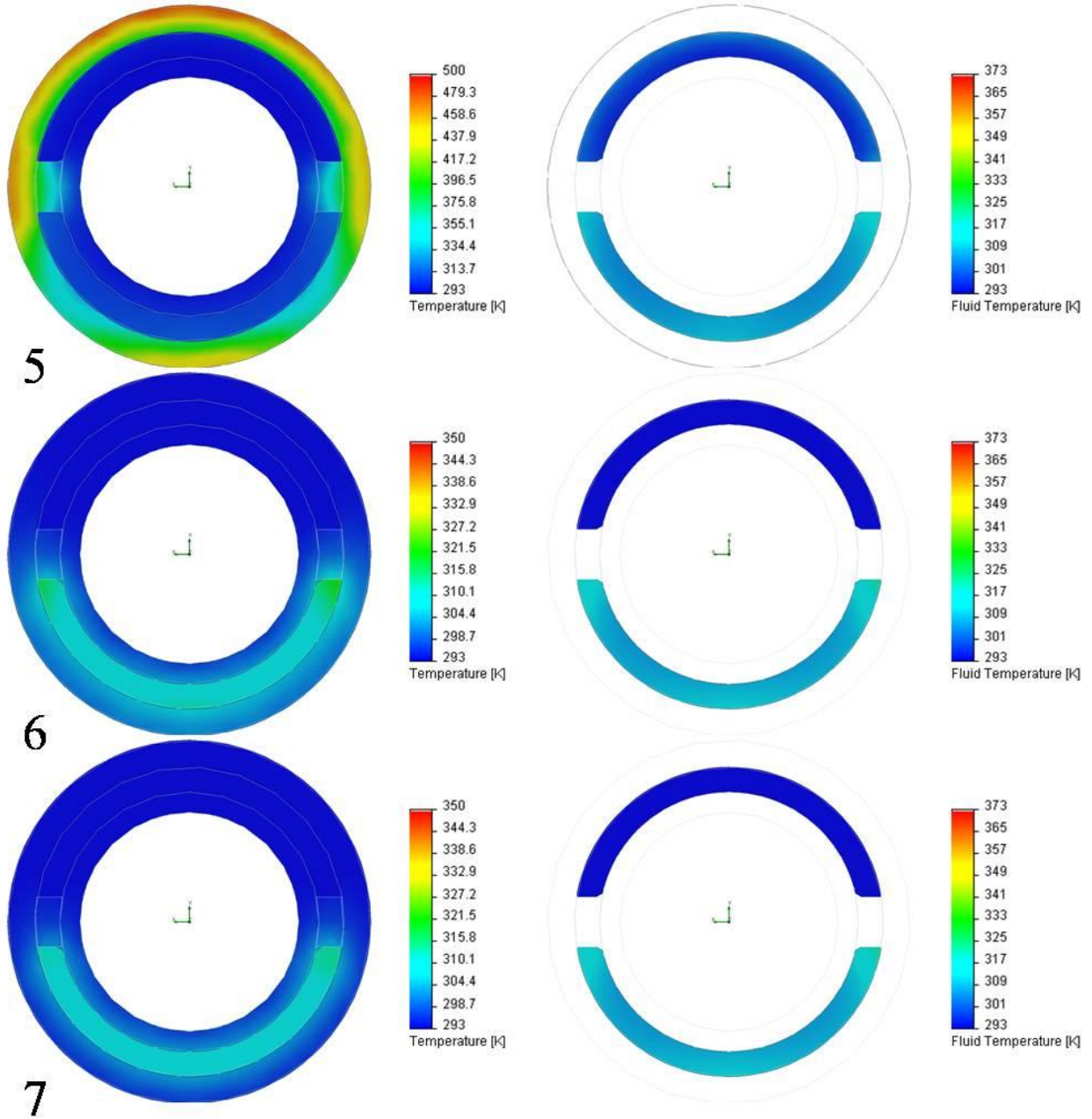


Figure 101. Temperature (left) and Fluid Temperature (right) distributions for probe insertion of 50% at Mach 0.7 with flat tip at Planes 5, 6, and 7.

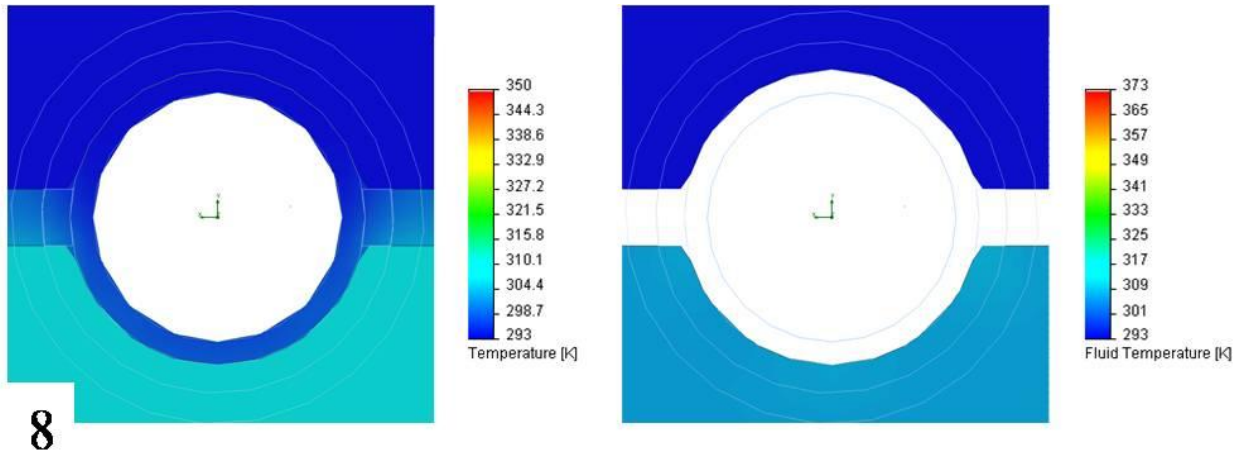


Figure 102. Temperature (left) and Fluid Temperature (right) distributions for probe insertion of 50% at Mach 0.7 with flat tip at Plane 8.

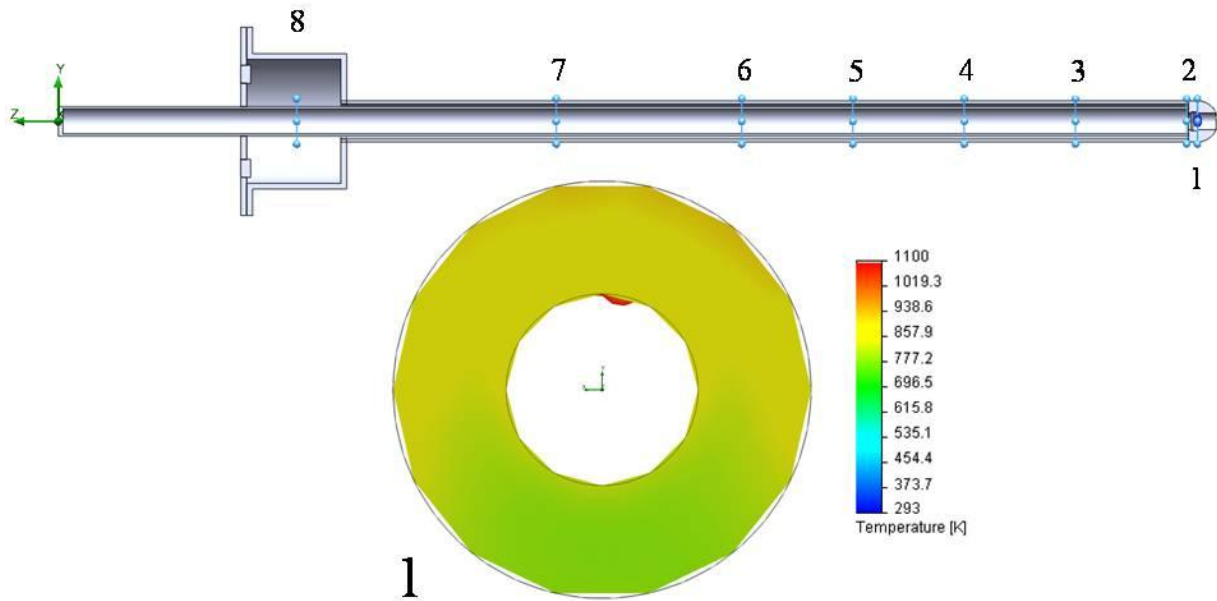


Figure 103. Plane locations along jacket length (top). Temperature distribution for probe insertion of 50% at Mach 0.7 with hemispherical tip at Plane 1 (bottom).

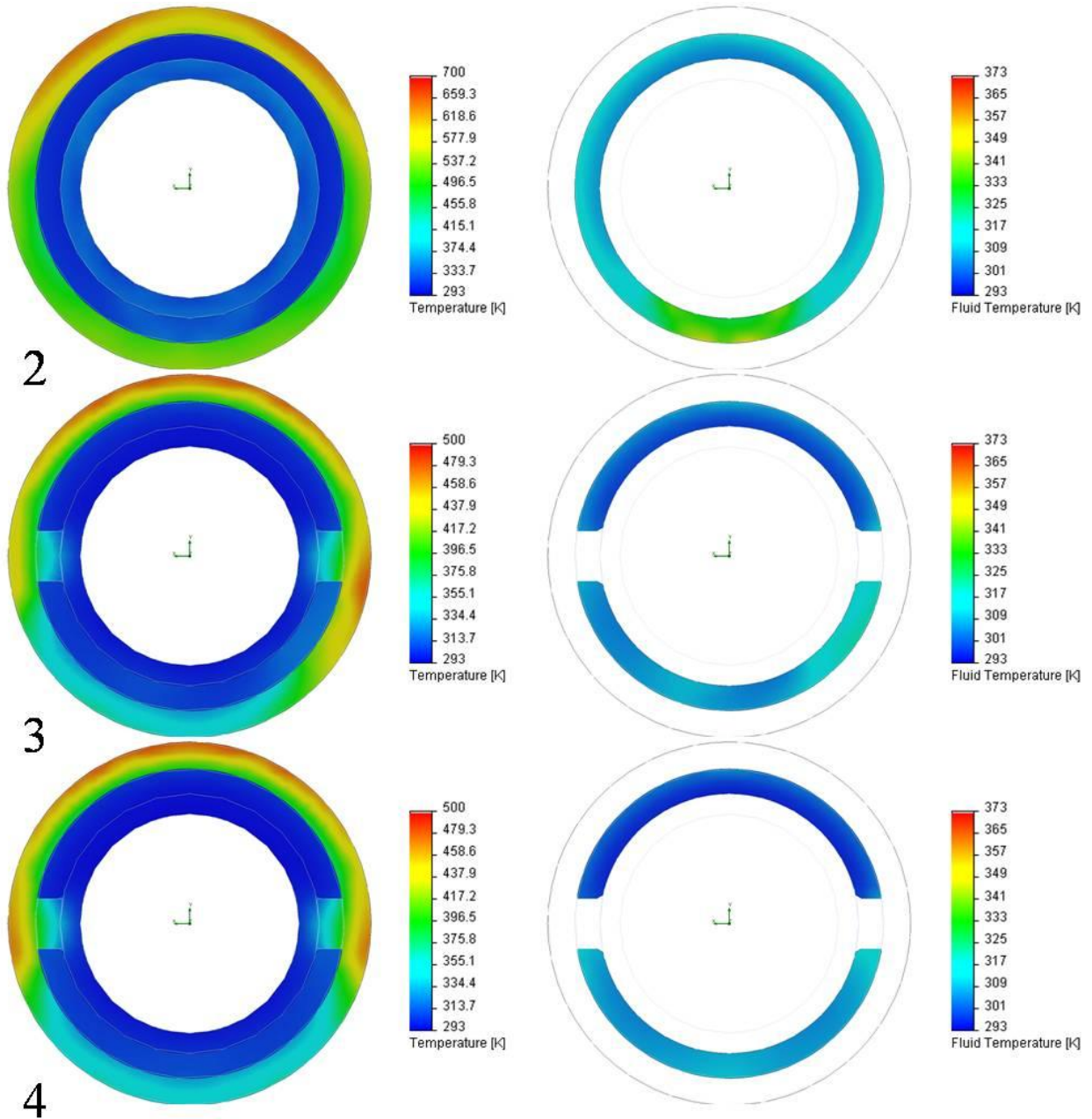


Figure 104. Temperature (left) and Fluid Temperature (right) distributions for probe insertion of 50% at Mach 0.7 with hemispherical tip at Planes 2, 3, and 4.

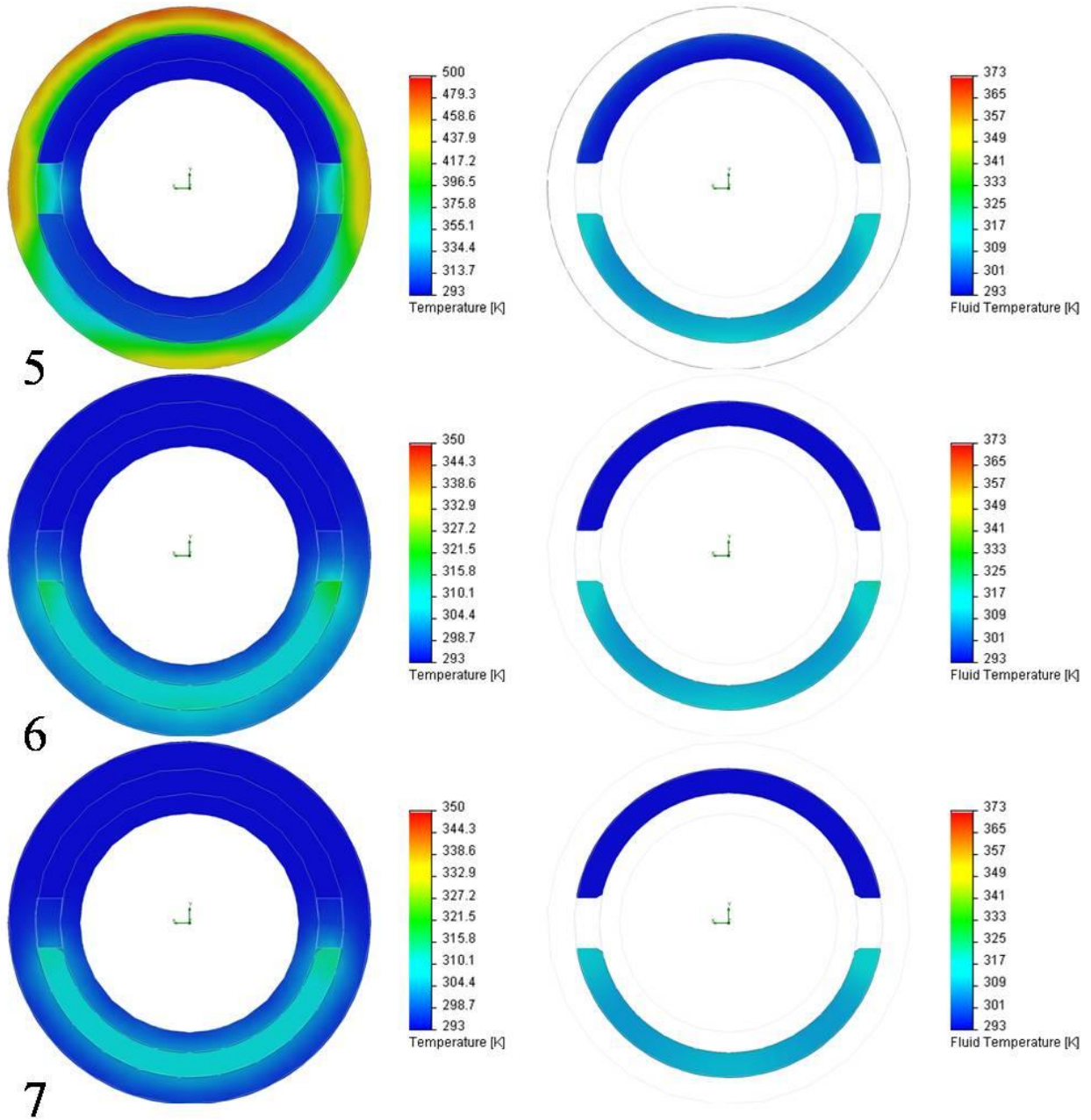


Figure 105. Temperature (left) and Fluid Temperature (right) distributions for probe insertion of 50% at Mach 0.7 with hemispherical tip at Planes 5, 6, and 7.

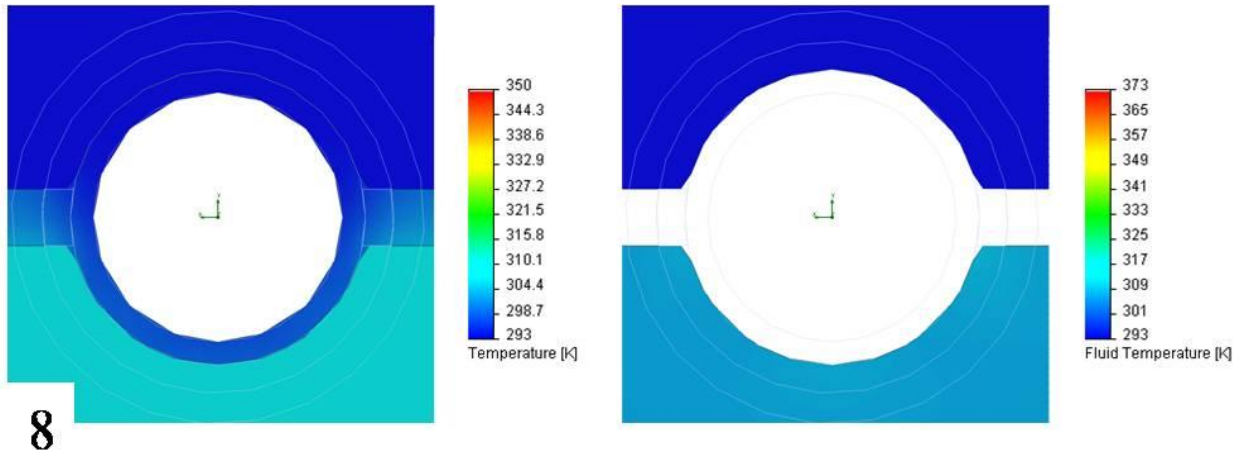


Figure 106. Temperature (left) and Fluid Temperature (right) distributions for probe insertion of 50% at Mach 0.7 with hemispherical tip at Plane 8.

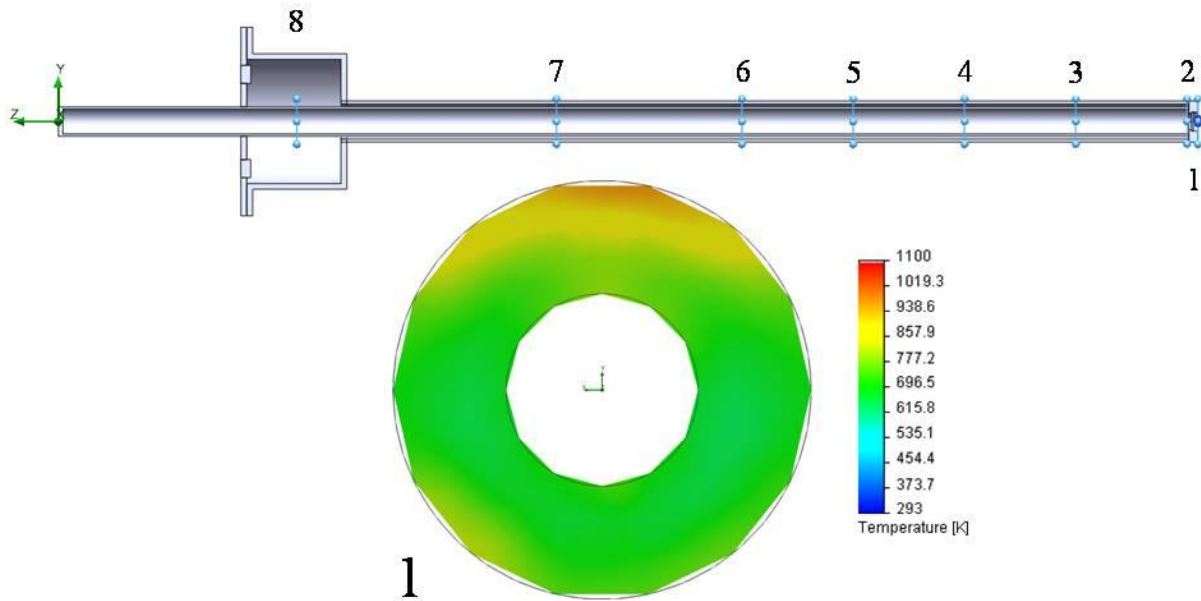


Figure 107. Plane locations along jacket length (top). Temperature distribution for probe insertion of 50% at Mach 0.5 with flat tip at Plane 1 (bottom).

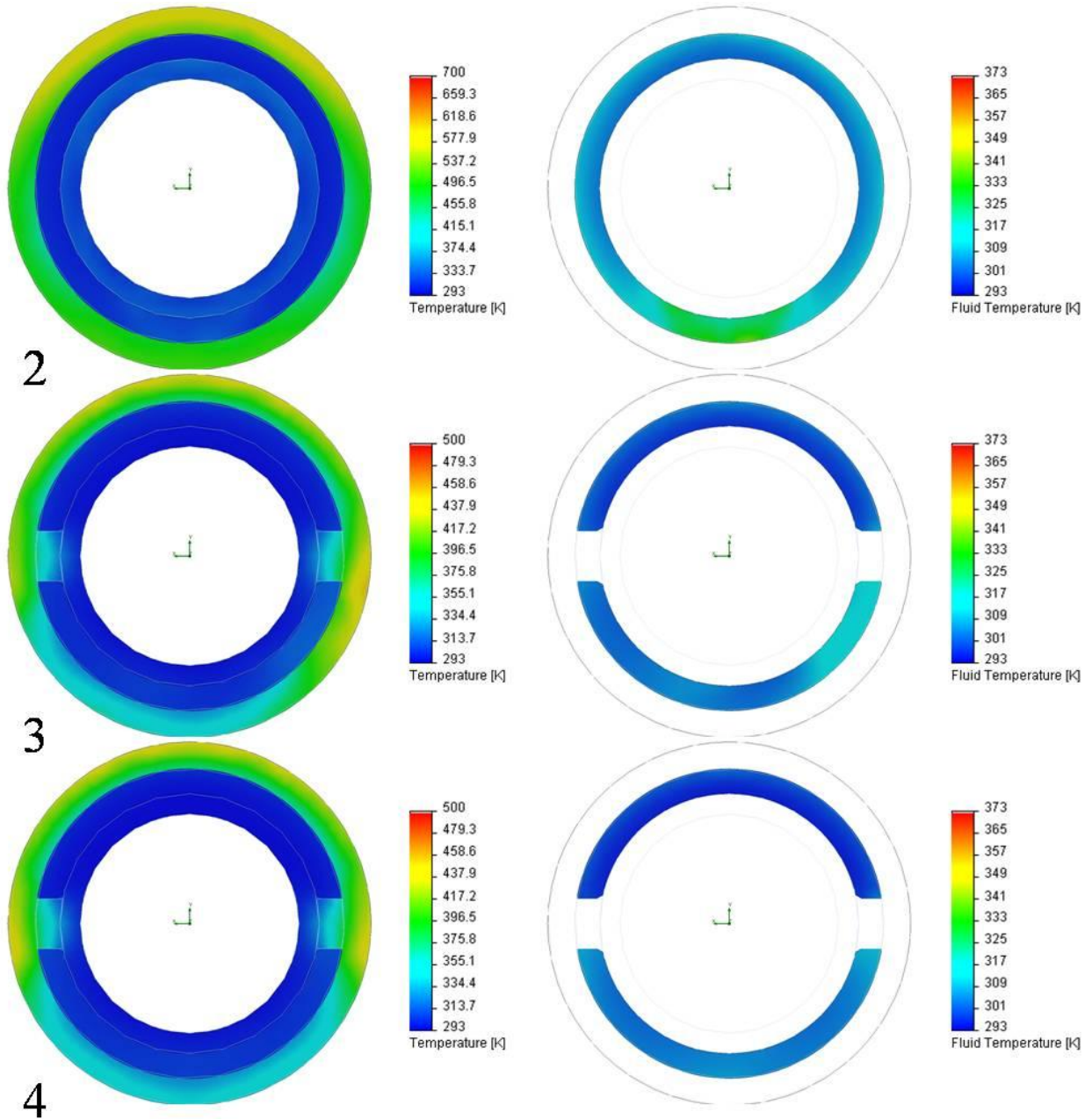


Figure 108. Temperature (left) and Fluid Temperature (right) distributions for probe insertion of 50% at Mach 0.5 with flat tip at Planes 2, 3, and 4.

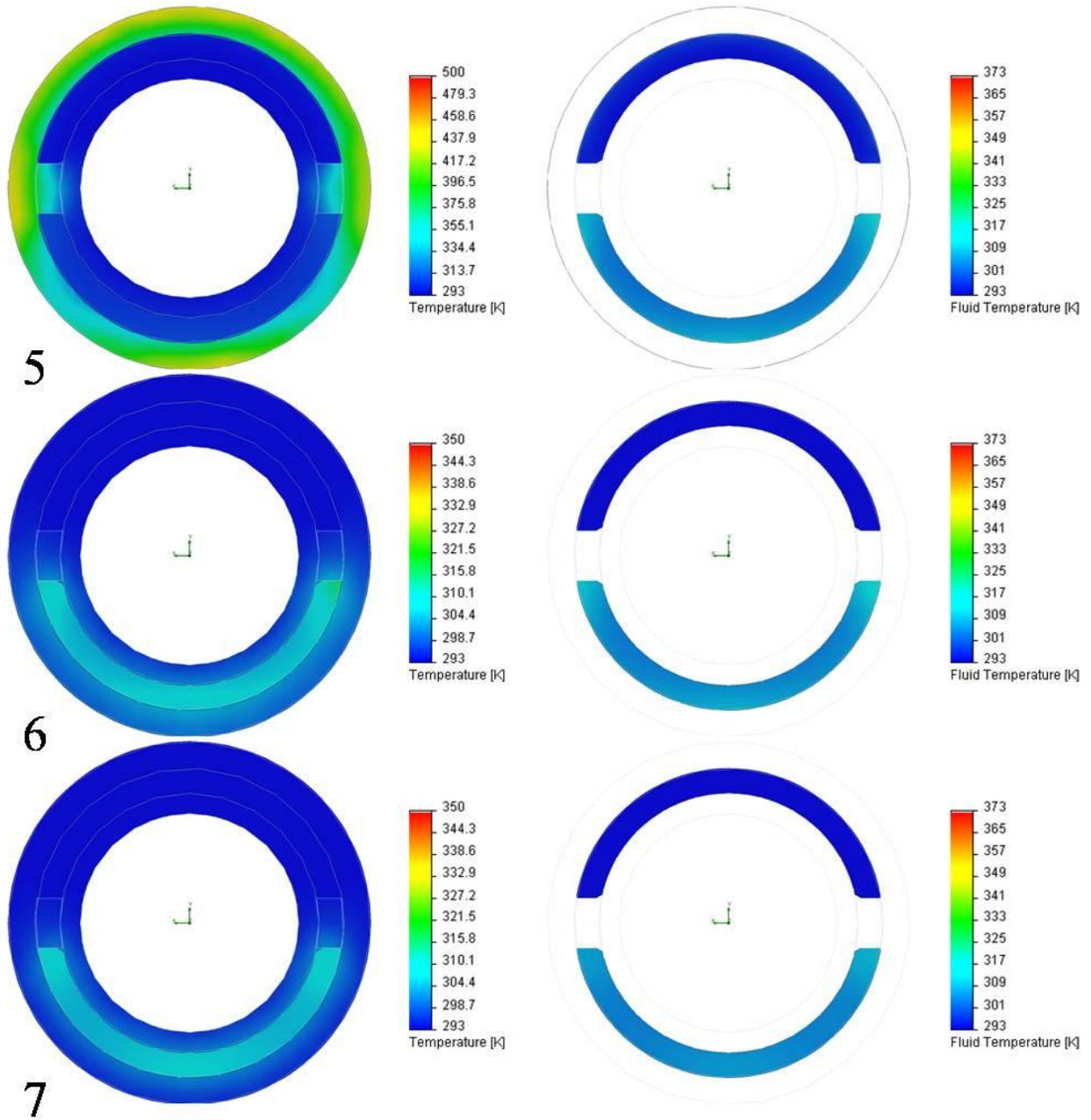


Figure 109. Temperature (left) and Fluid Temperature (right) distributions for probe insertion of 50% at Mach 0.5 with flat tip at Planes 5, 6, and 7.

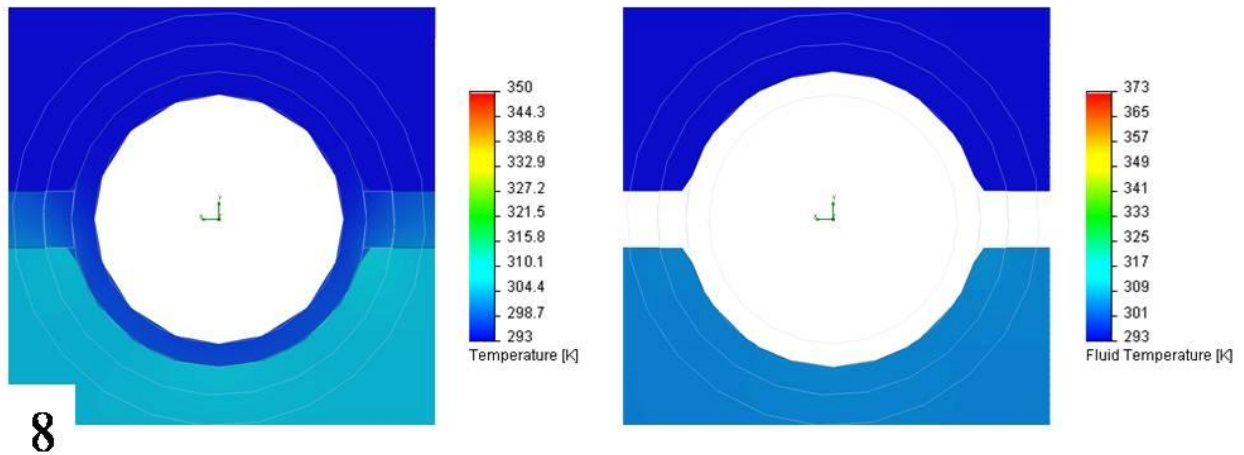


Figure 110. Temperature (left) and Fluid Temperature (right) distributions for probe insertion of 50% at Mach 0.5 with flat tip at Plane 8.

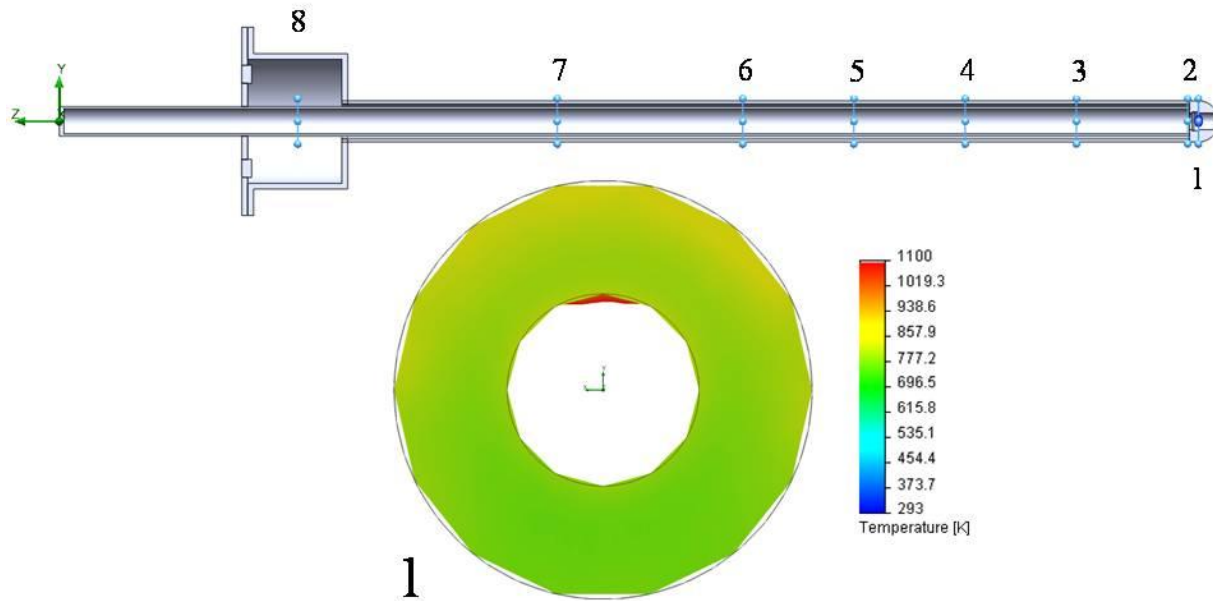


Figure 111. Plane locations along jacket length (top). Temperature distribution for probe insertion of 50% at Mach 0.5 with hemispherical tip at Plane 1 (bottom).

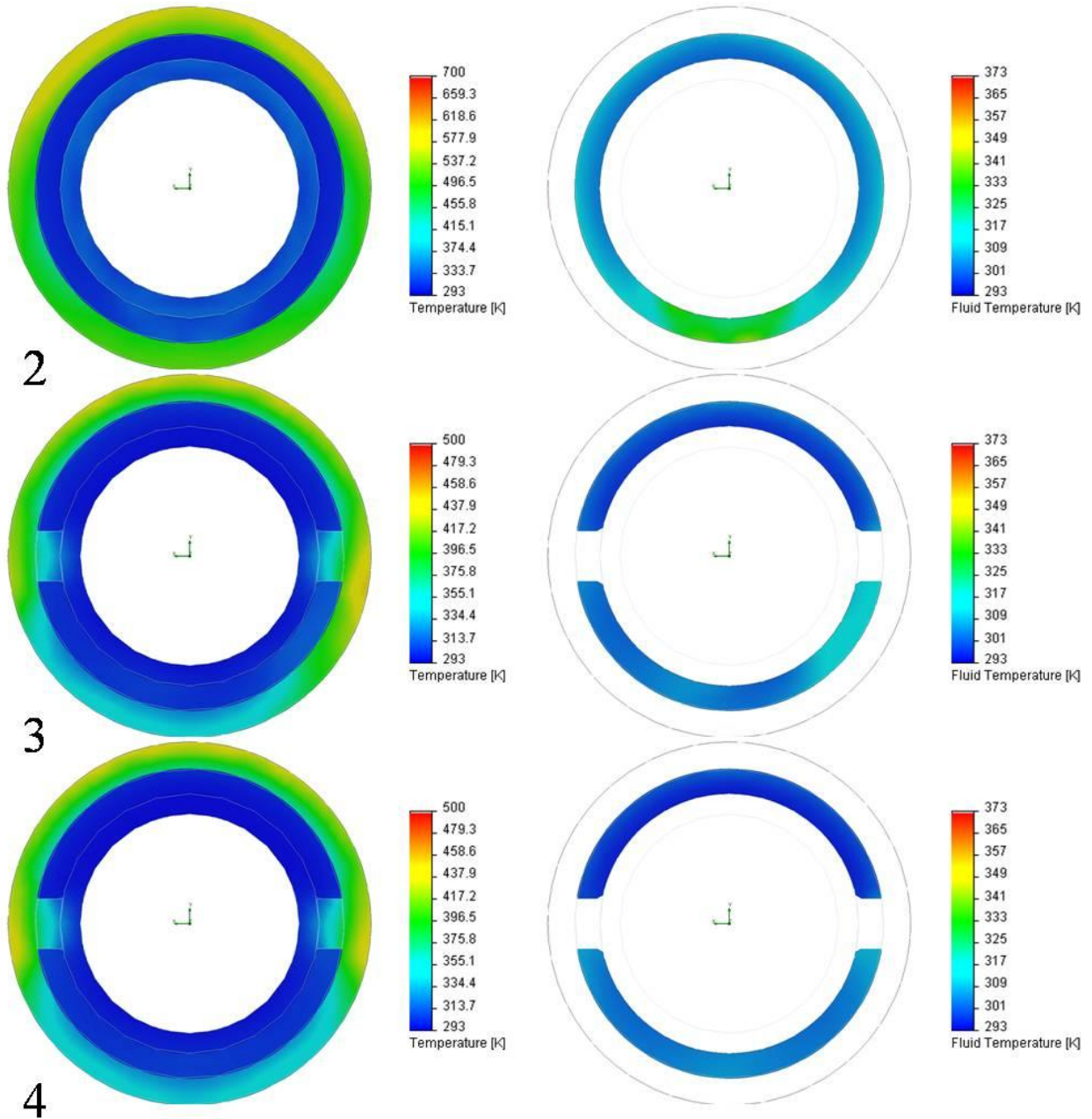


Figure 112. Temperature (left) and Fluid Temperature (right) distributions for probe insertion of 50% at Mach 0.5 with hemispherical tip at Planes 2, 3, and 4.

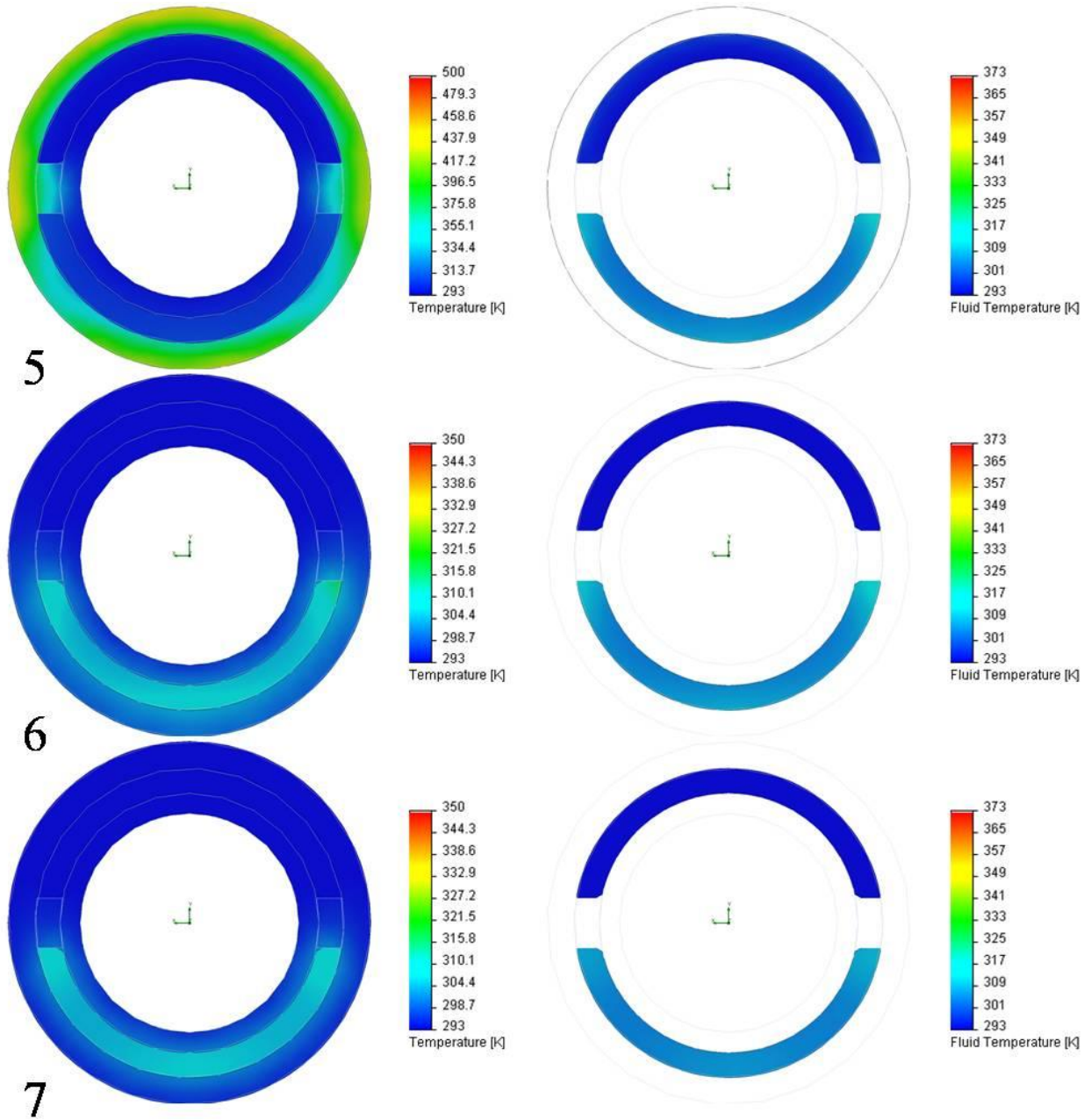


Figure 113. Temperature (left) and Fluid Temperature (right) distributions for probe insertion of 50% at Mach 0.5 with hemispherical tip at Planes 5, 6, and 7.

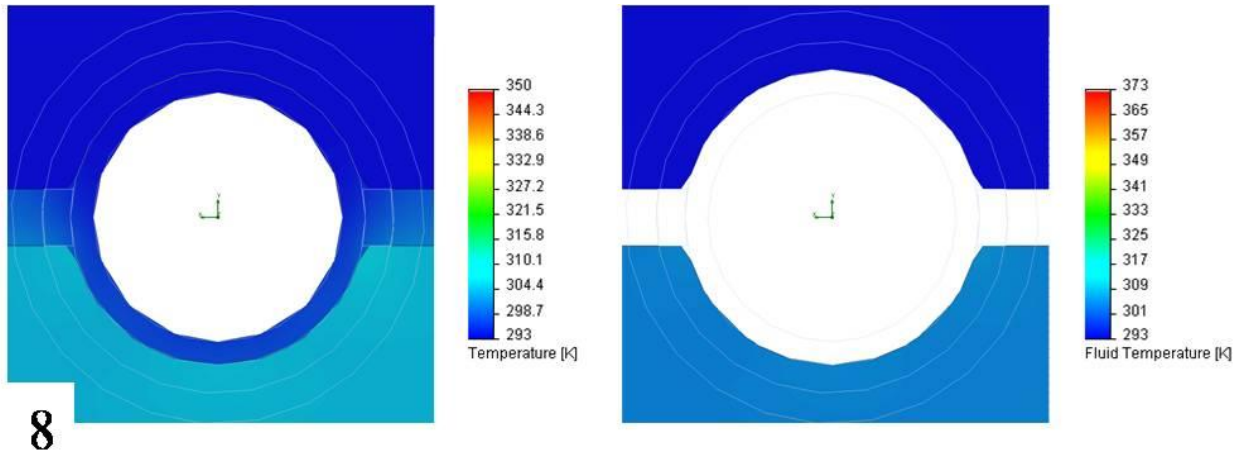


Figure 114. Temperature (left) and Fluid Temperature (right) distributions for probe insertion of 50% at Mach 0.5 with hemispherical tip at Plane 8.

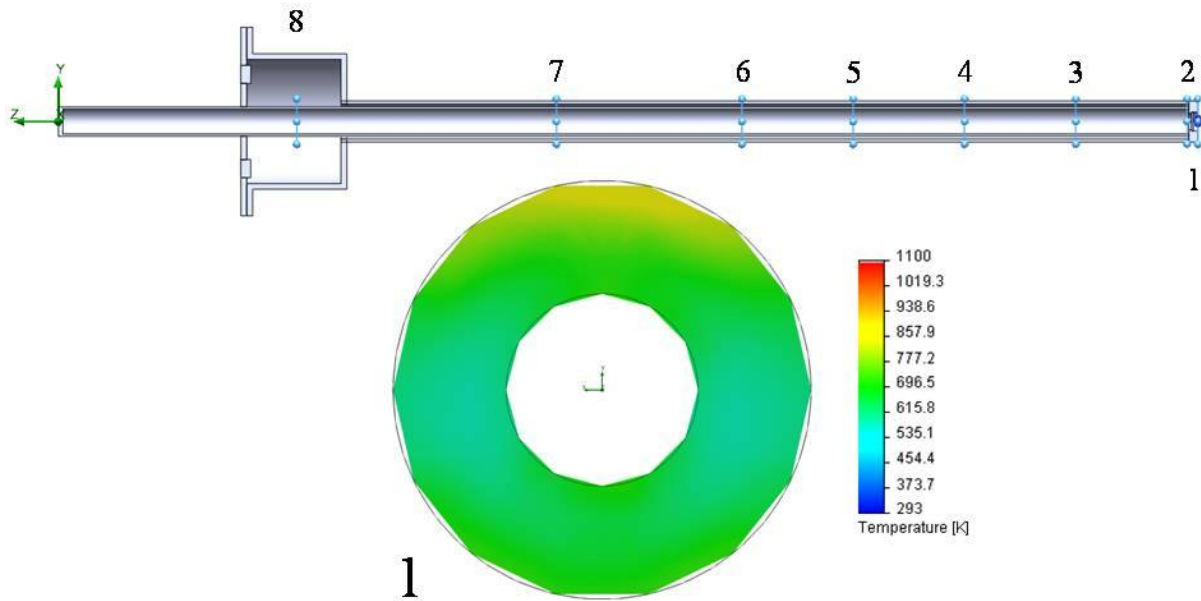


Figure 115. Plane locations along jacket length (top). Temperature distribution for probe insertion of 50% at Mach 0.3 with flat tip at Plane 1 (bottom).

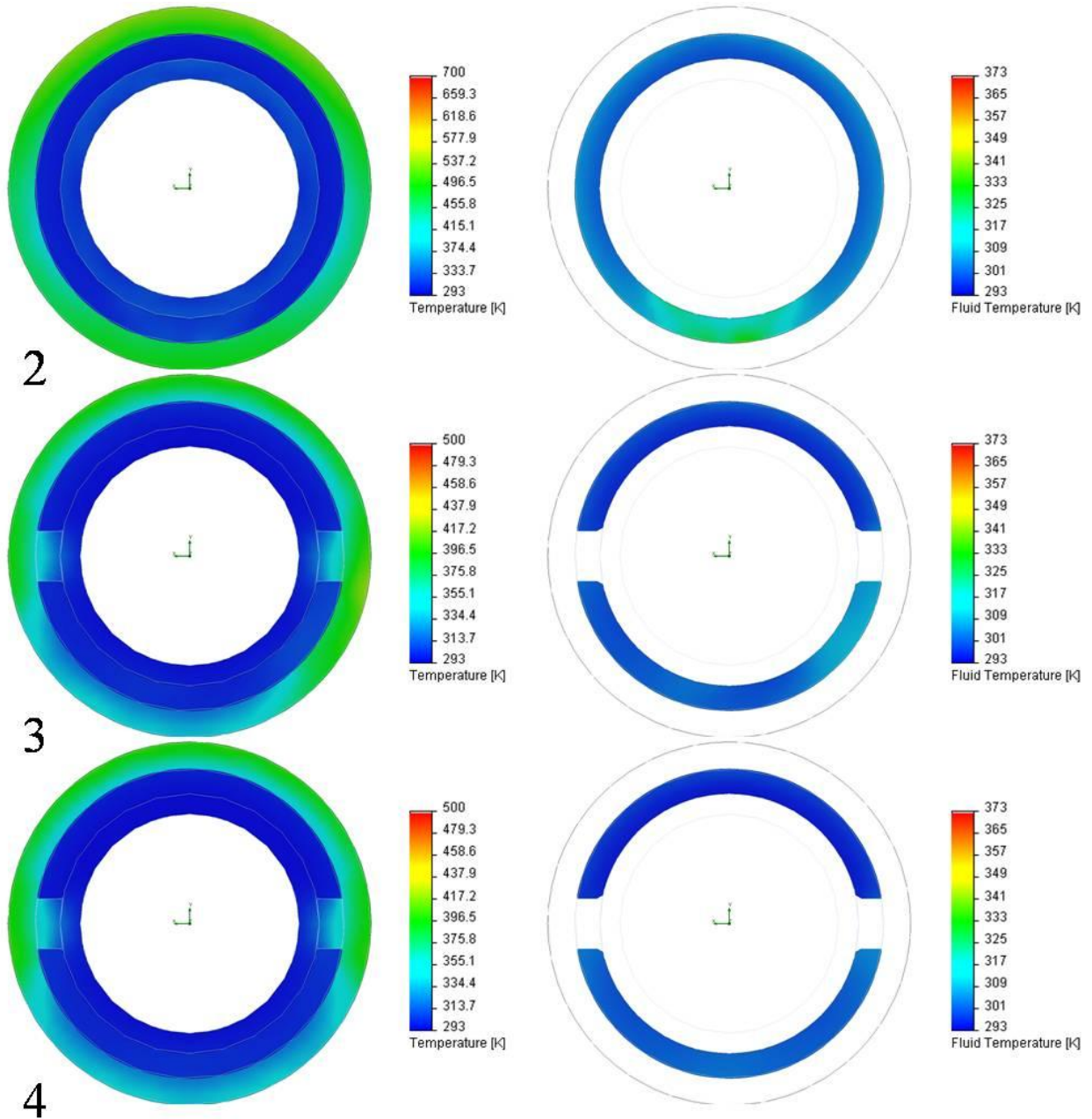


Figure 116. Temperature (left) and Fluid Temperature (right) distributions for probe insertion of 50% at Mach 0.3 with flat tip at Planes 2, 3, and 4.

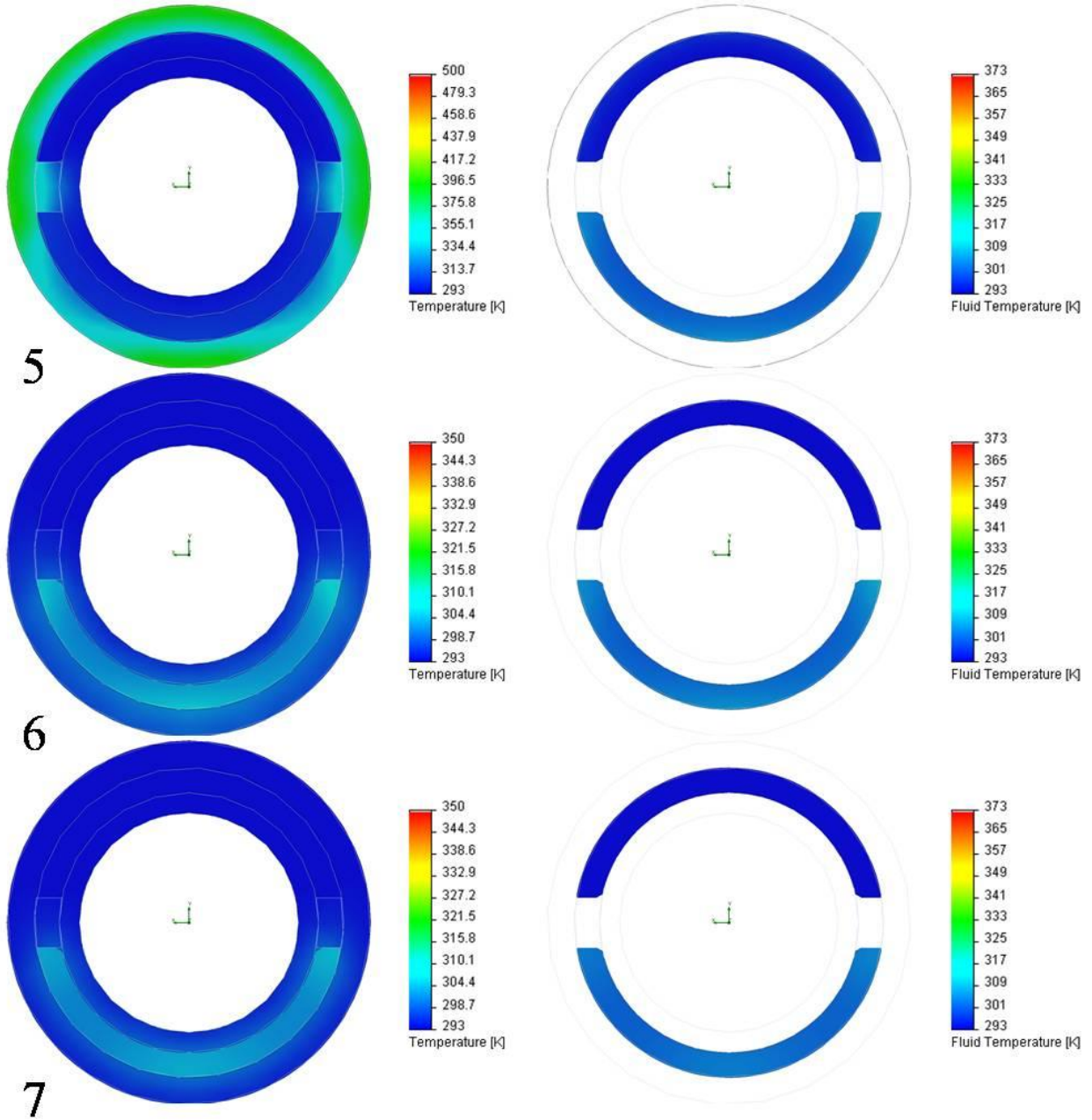


Figure 117. Temperature (left) and Fluid Temperature (right) distributions for probe insertion of 50% at Mach 0.3 with flat tip at Planes 5, 6, and 7.

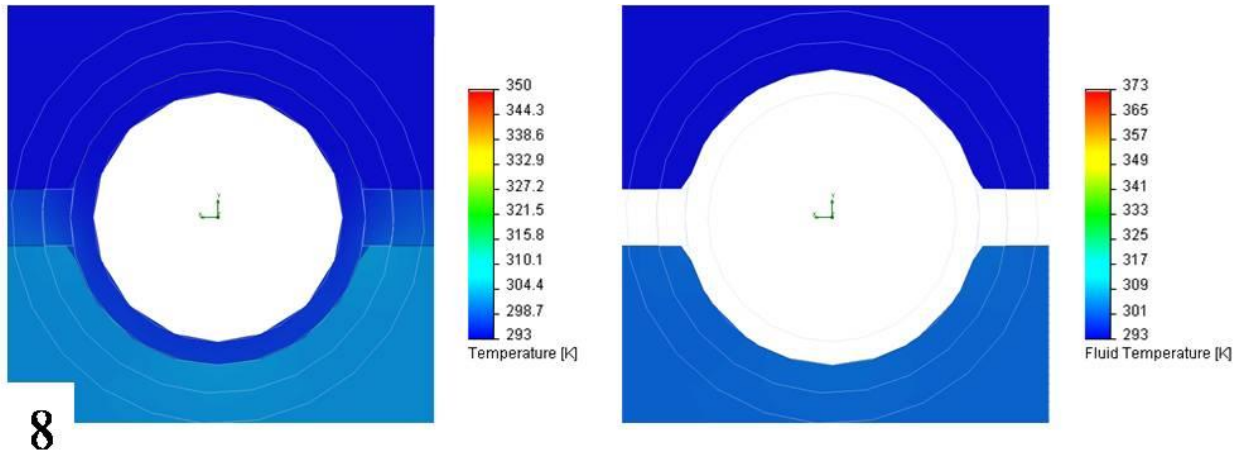


Figure 118. Temperature (left) and Fluid Temperature (right) distributions for probe insertion of 50% at Mach 0.3 with flat tip at Plane 8.

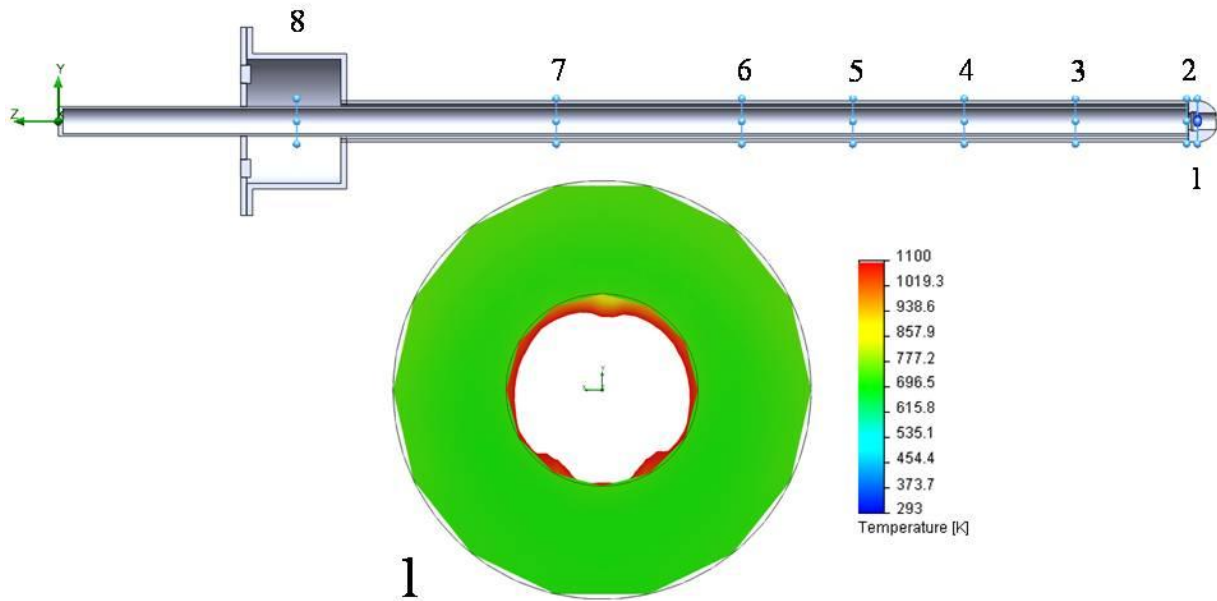


Figure 119. Plane locations along jacket length (top). Temperature distribution for probe insertion of 50% at Mach 0.3 with hemispherical tip at Plane 1 (bottom).

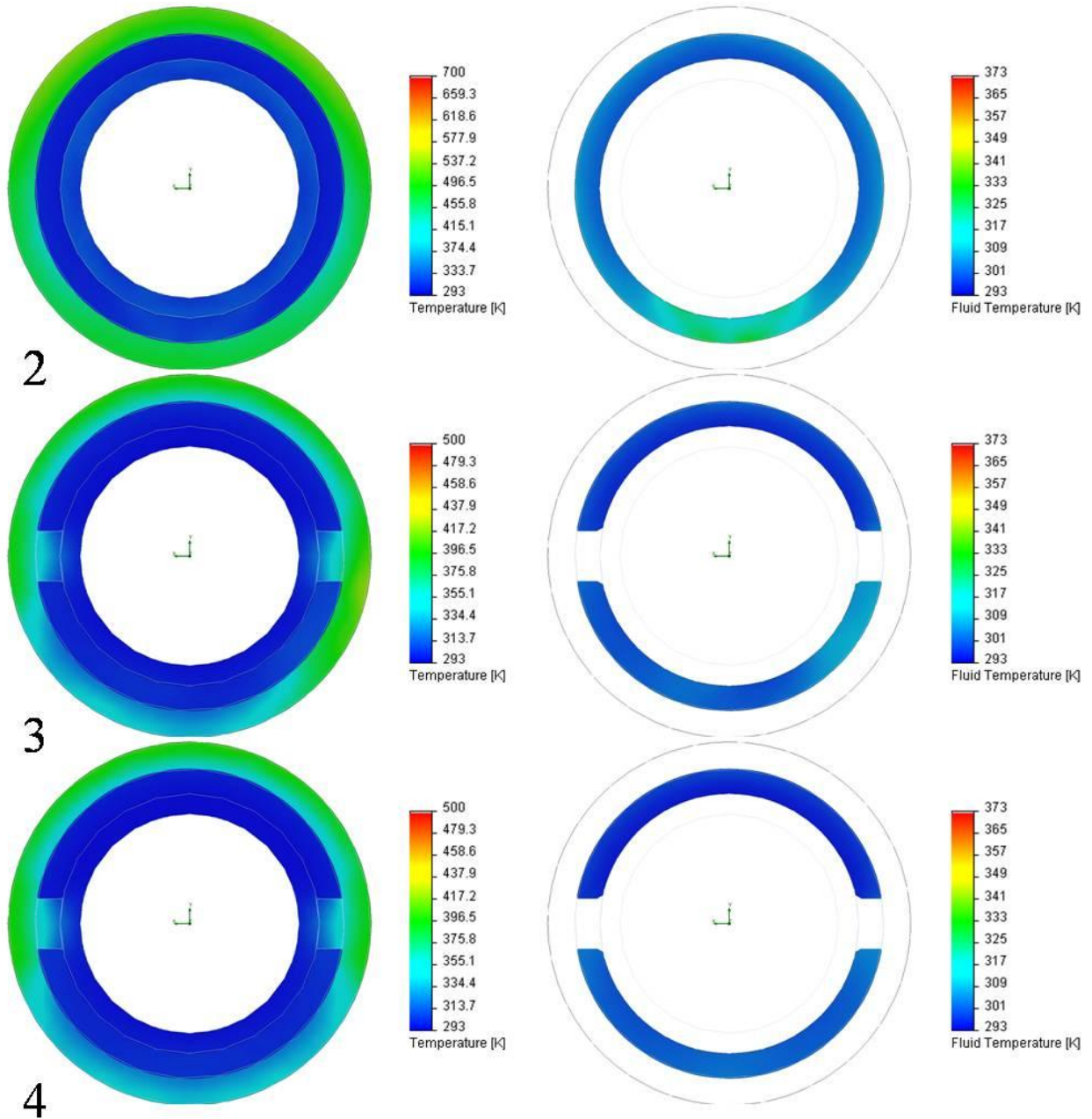


Figure 120. Temperature (left) and Fluid Temperature (right) distributions for probe insertion of 50% at Mach 0.3 with hemispherical tip at Planes 2, 3, and 4.

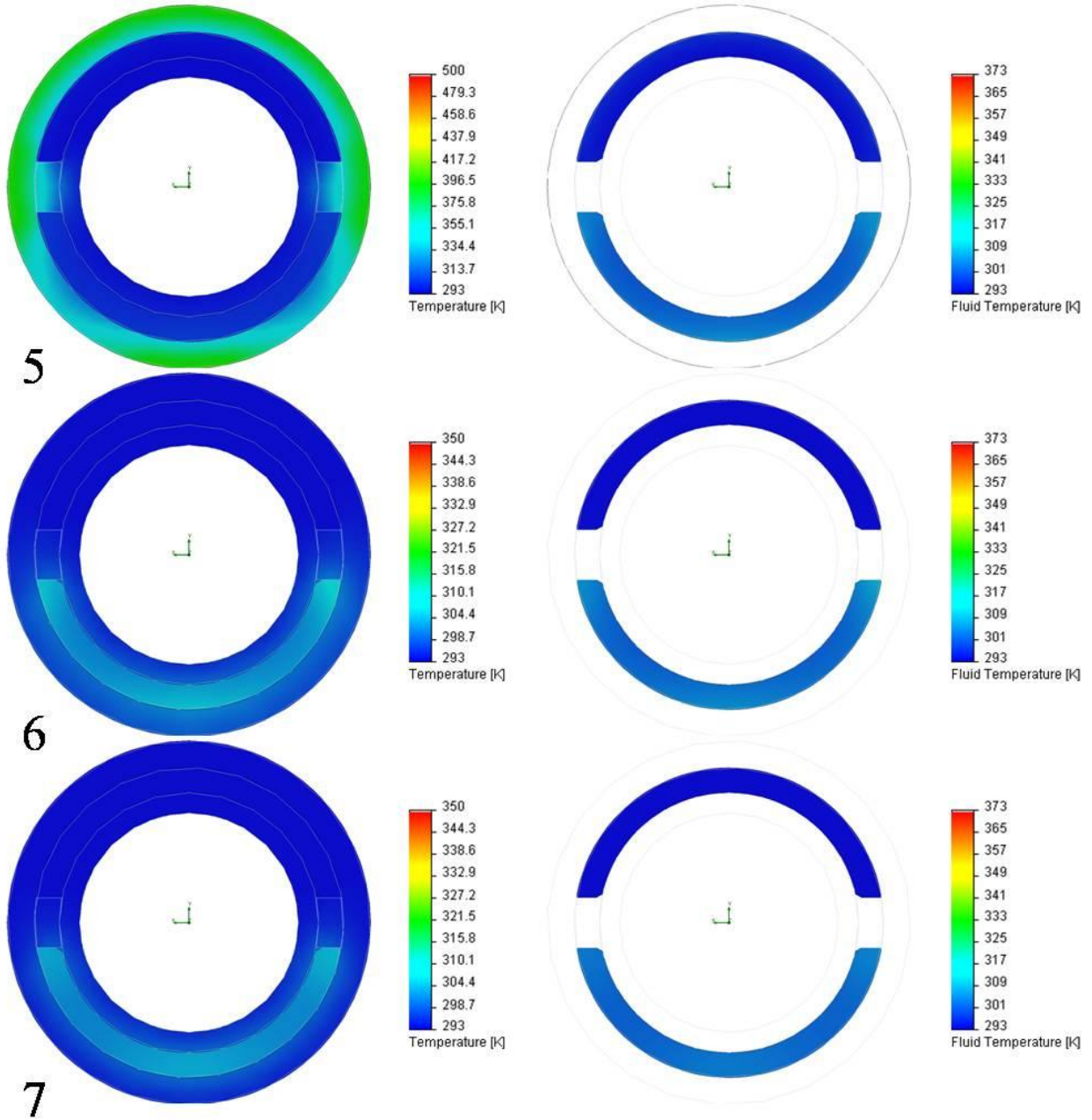


Figure 121. Temperature (left) and Fluid Temperature (right) distributions for probe insertion of 50% at Mach 0.3 with hemispherical tip at Planes 5, 6, and 7.

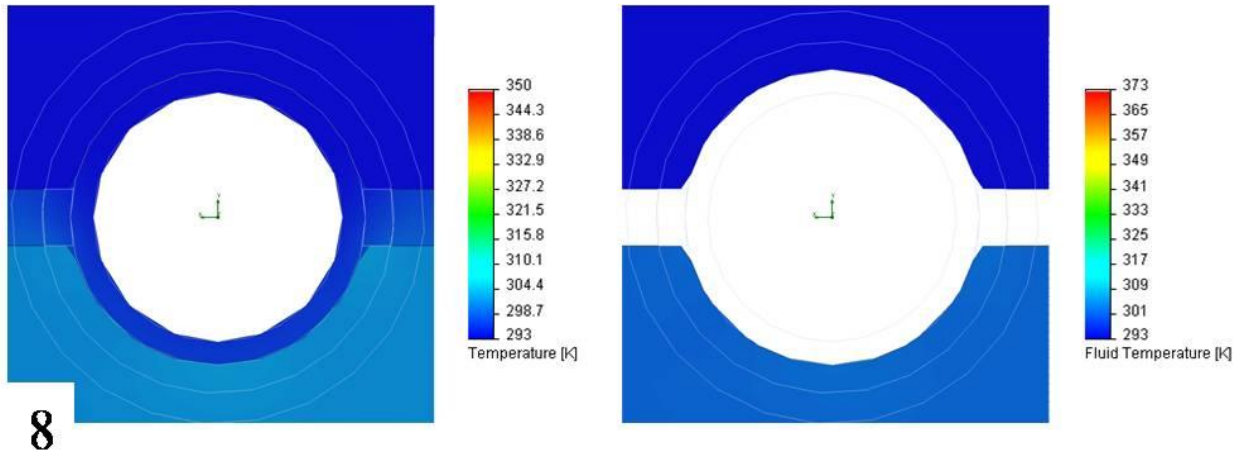


Figure 122. Temperature (left) and Fluid Temperature (right) distributions for probe insertion of 50% at Mach 0.3 with hemispherical tip at Plane 8.

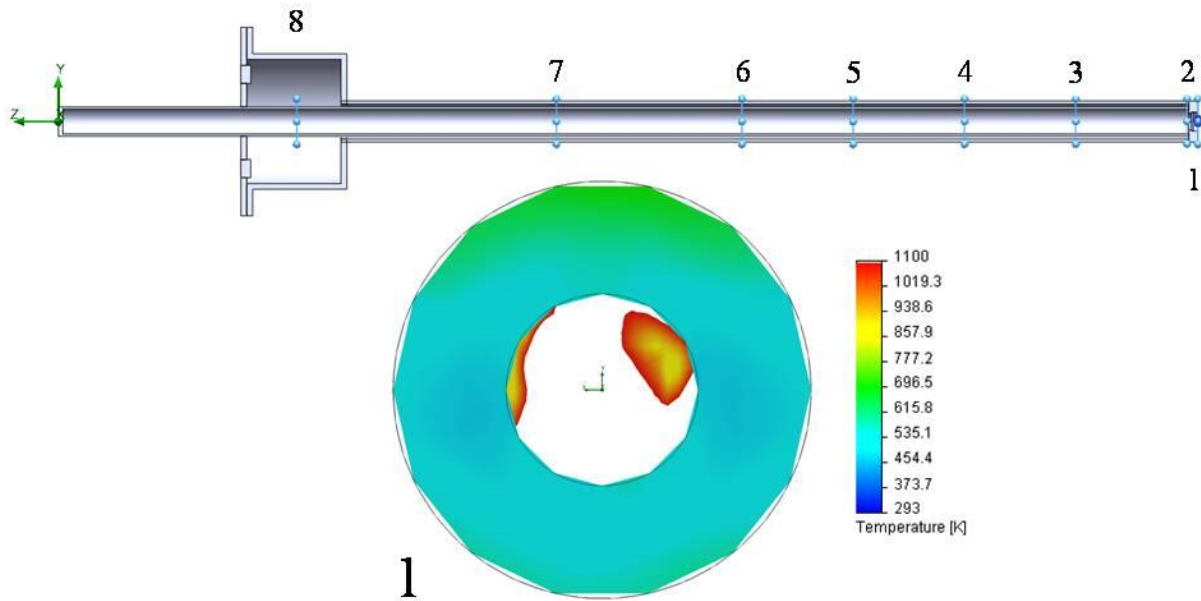


Figure 123. Plane locations along jacket length (top). Temperature distribution for probe insertion of 50% at Mach 0.1 with flat tip at Plane 1 (bottom).

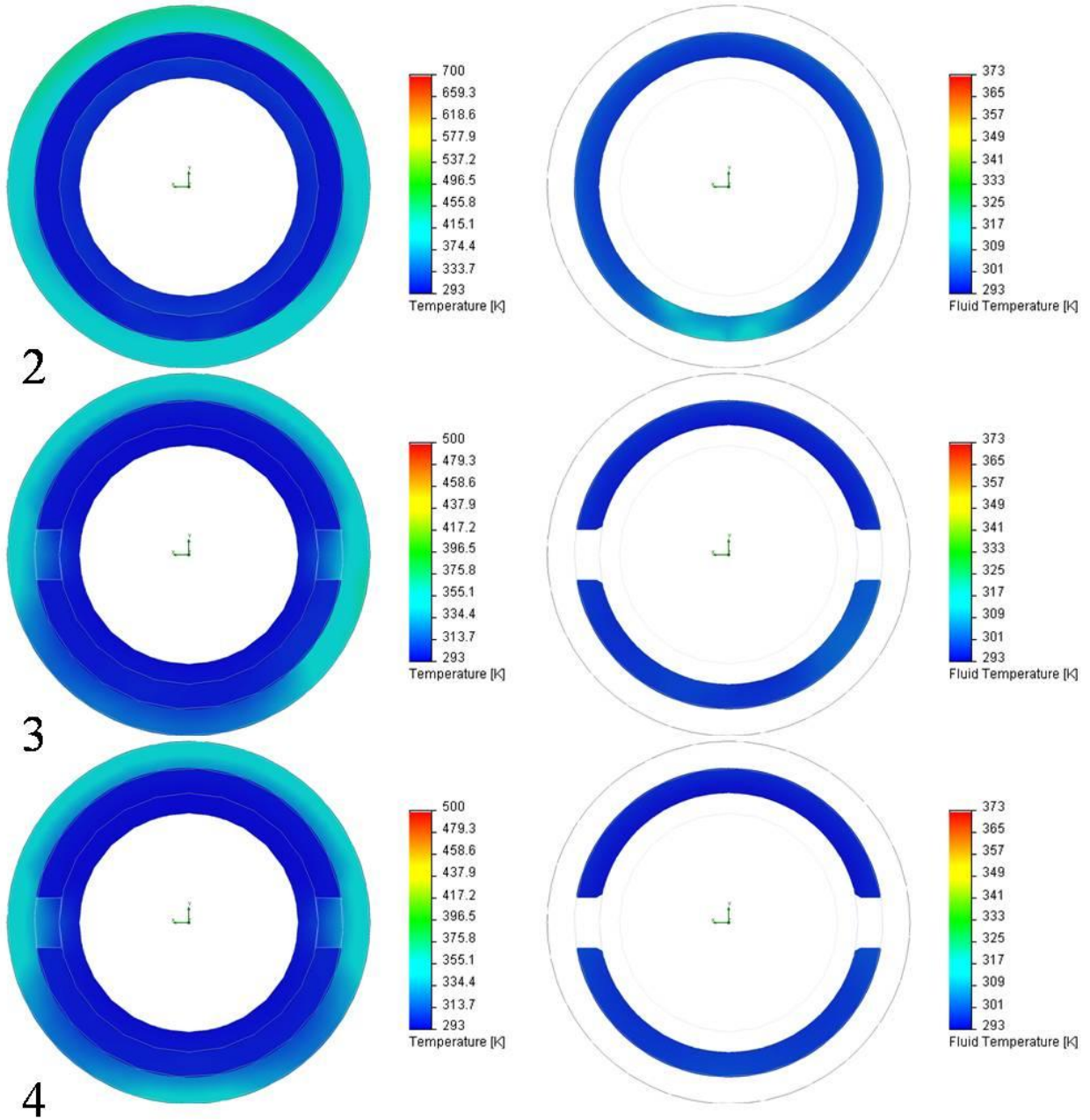


Figure 124. Temperature (left) and Fluid Temperature (right) distributions for probe insertion of 50% at Mach 0.1 with flat tip at Planes 2, 3, and 4.

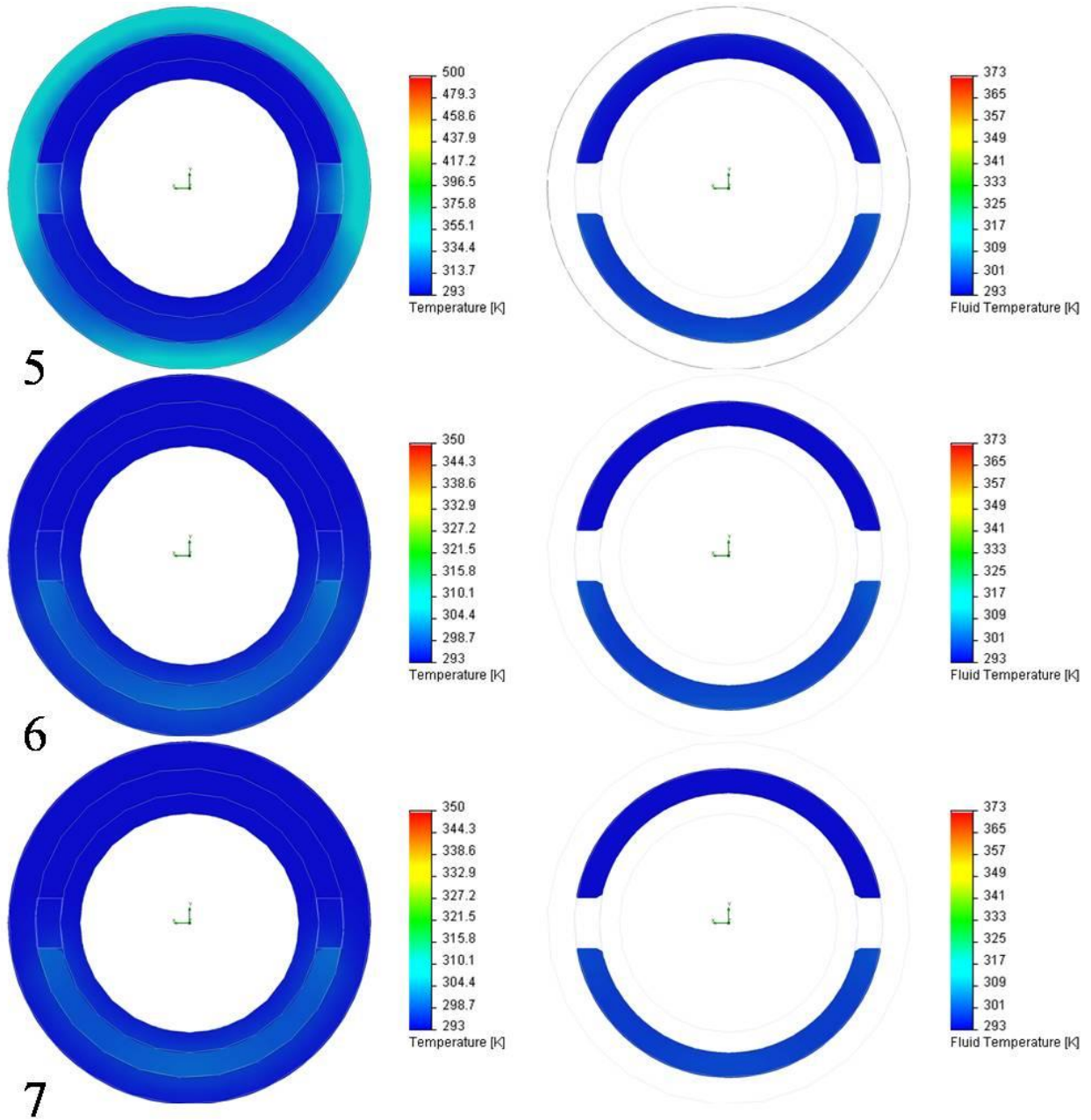


Figure 125. Temperature (left) and Fluid Temperature (right) distributions for probe insertion of 50% at Mach 0.1 with flat tip at Planes 5, 6, and 7.

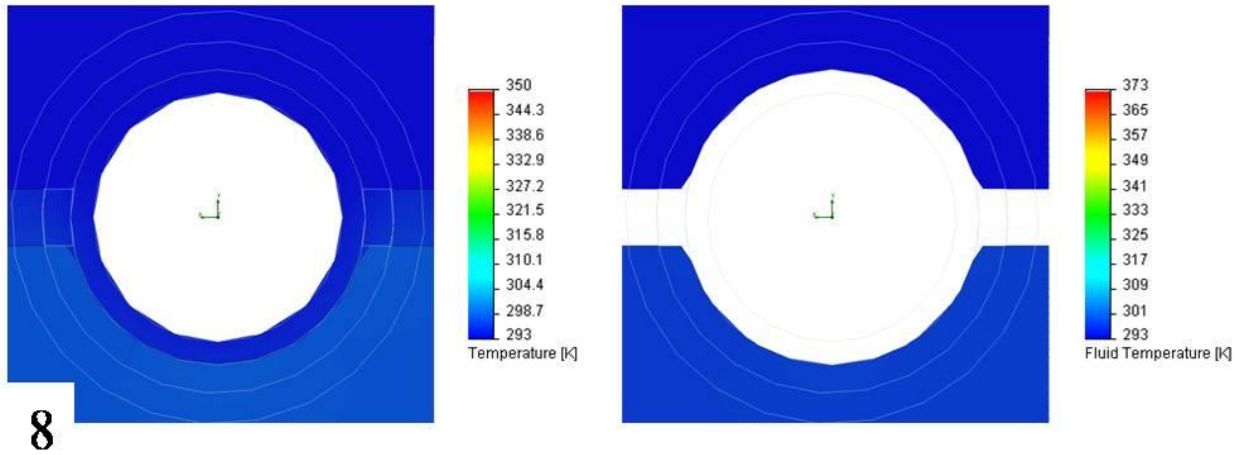


Figure 126. Temperature (left) and Fluid Temperature (right) distributions for probe insertion of 50% at Mach 0.1 with flat tip at Plane 8.

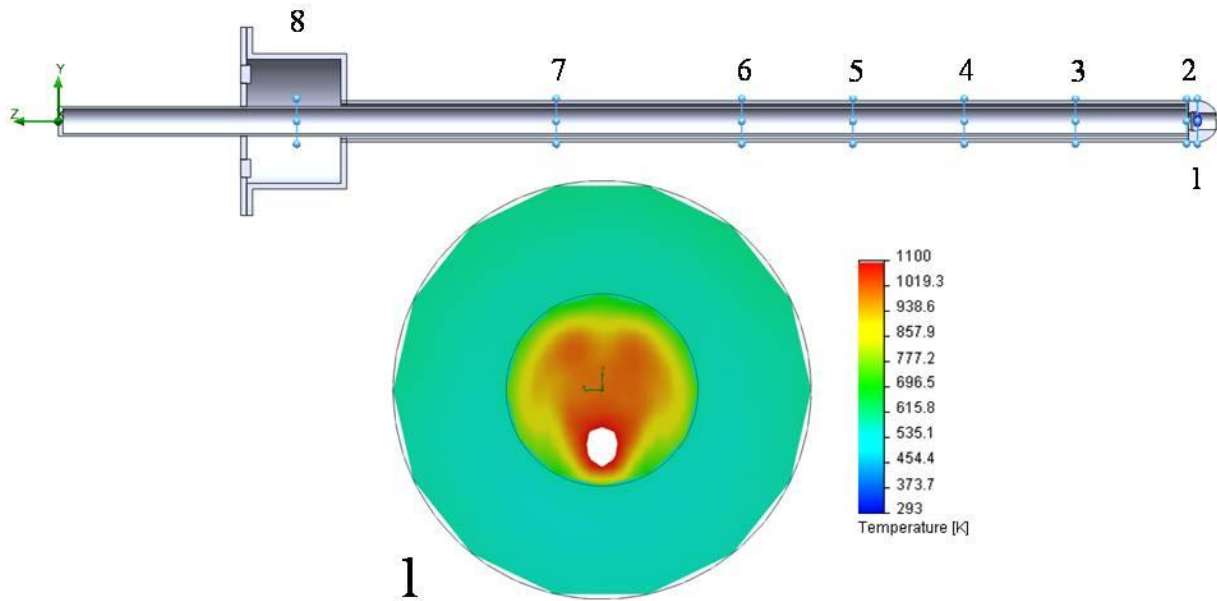


Figure 127. Plane locations along jacket length (top). Temperature distribution for probe insertion of 50% at Mach 0.1 with hemispherical tip at Plane 1 (bottom).

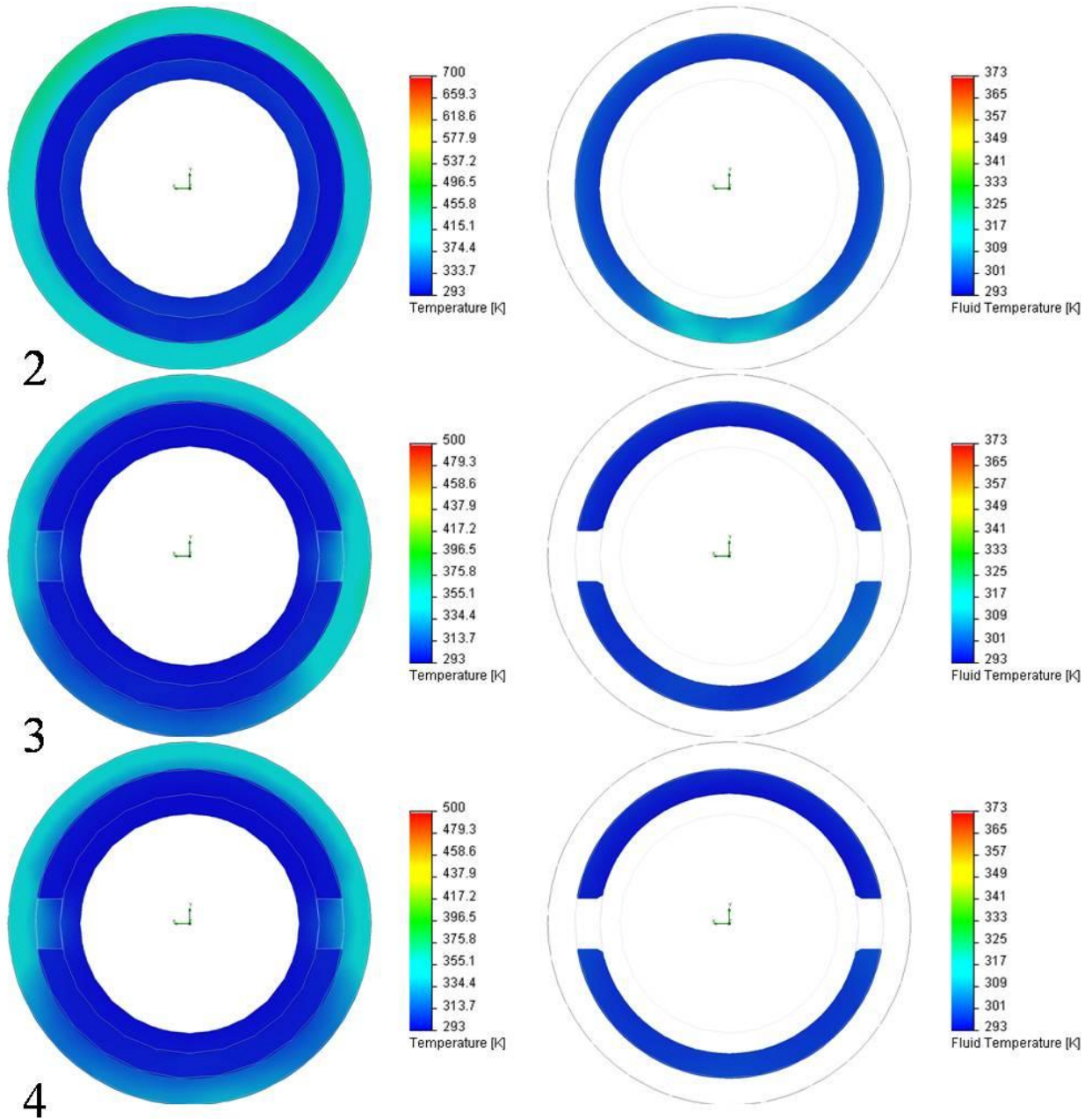


Figure 128. Temperature (left) and Fluid Temperature (right) distributions for probe insertion of 50% at Mach 0.1 with hemispherical tip at Planes 2, 3, and 4.

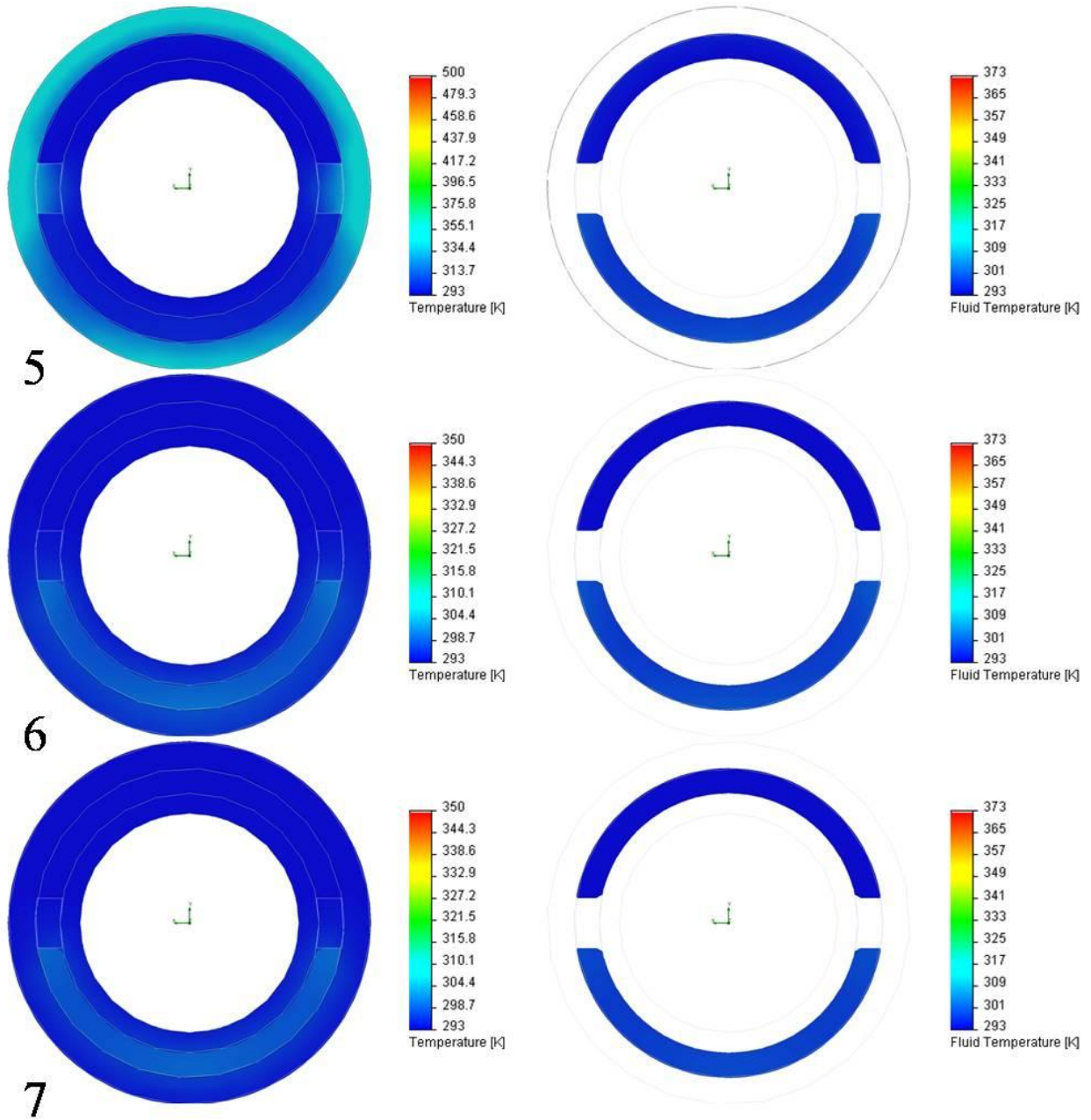


Figure 129. Temperature (left) and Fluid Temperature (right) distributions for probe insertion of 50% at Mach 0.1 with hemispherical tip at Planes 5, 6, and 7.

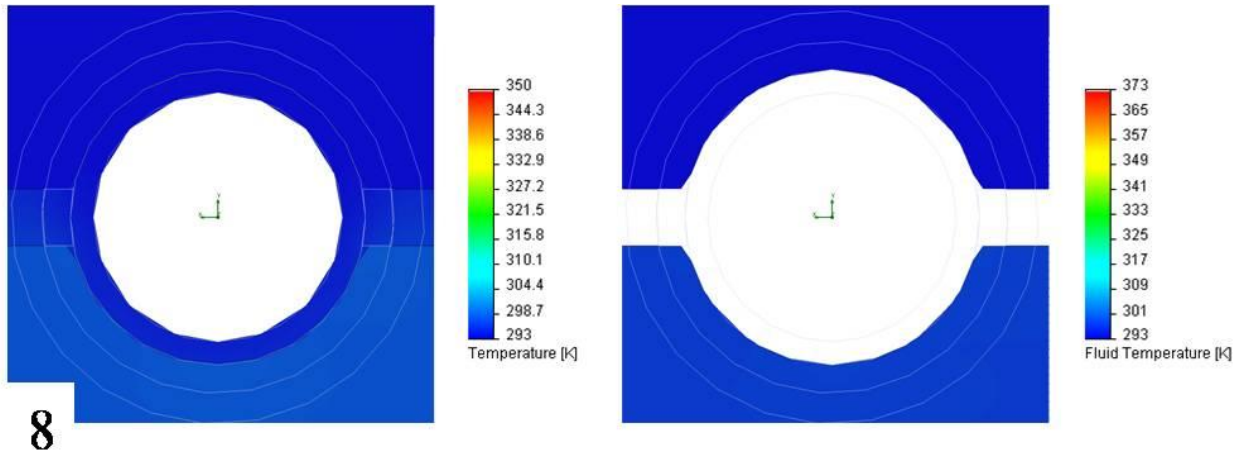


Figure 130. Temperature (left) and Fluid Temperature (right) distributions for probe insertion of 50% at Mach 0.1 with hemispherical tip at Plane 8.

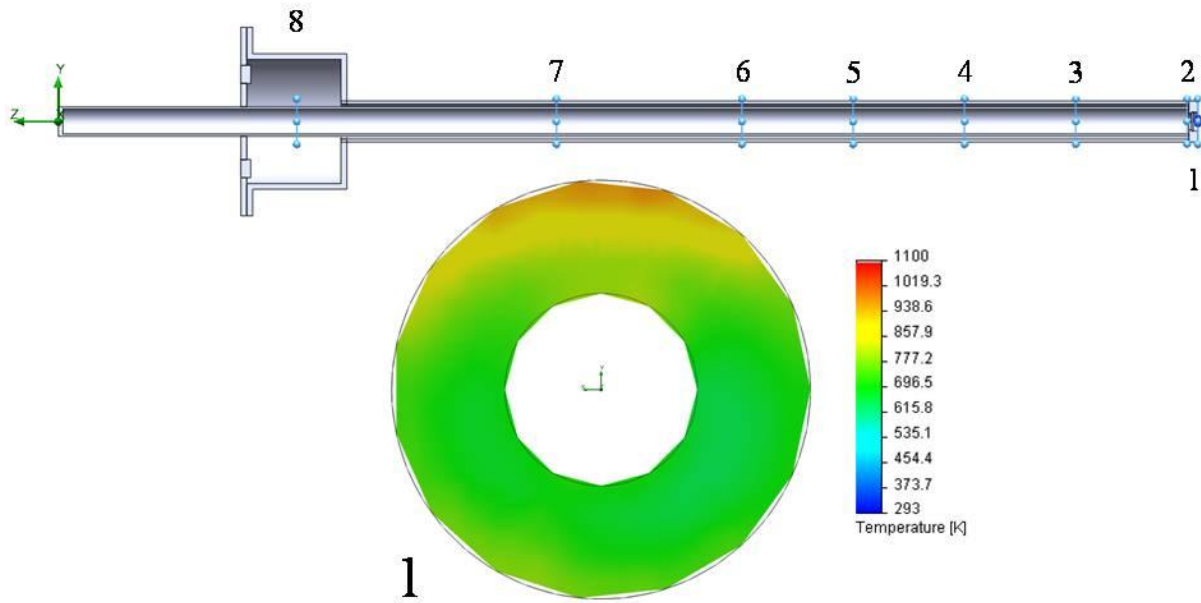


Figure 131. Plane locations along jacket length (top). Temperature distribution for probe insertion of 75% at Mach 0.7 with flat tip at Plane 1 (bottom).

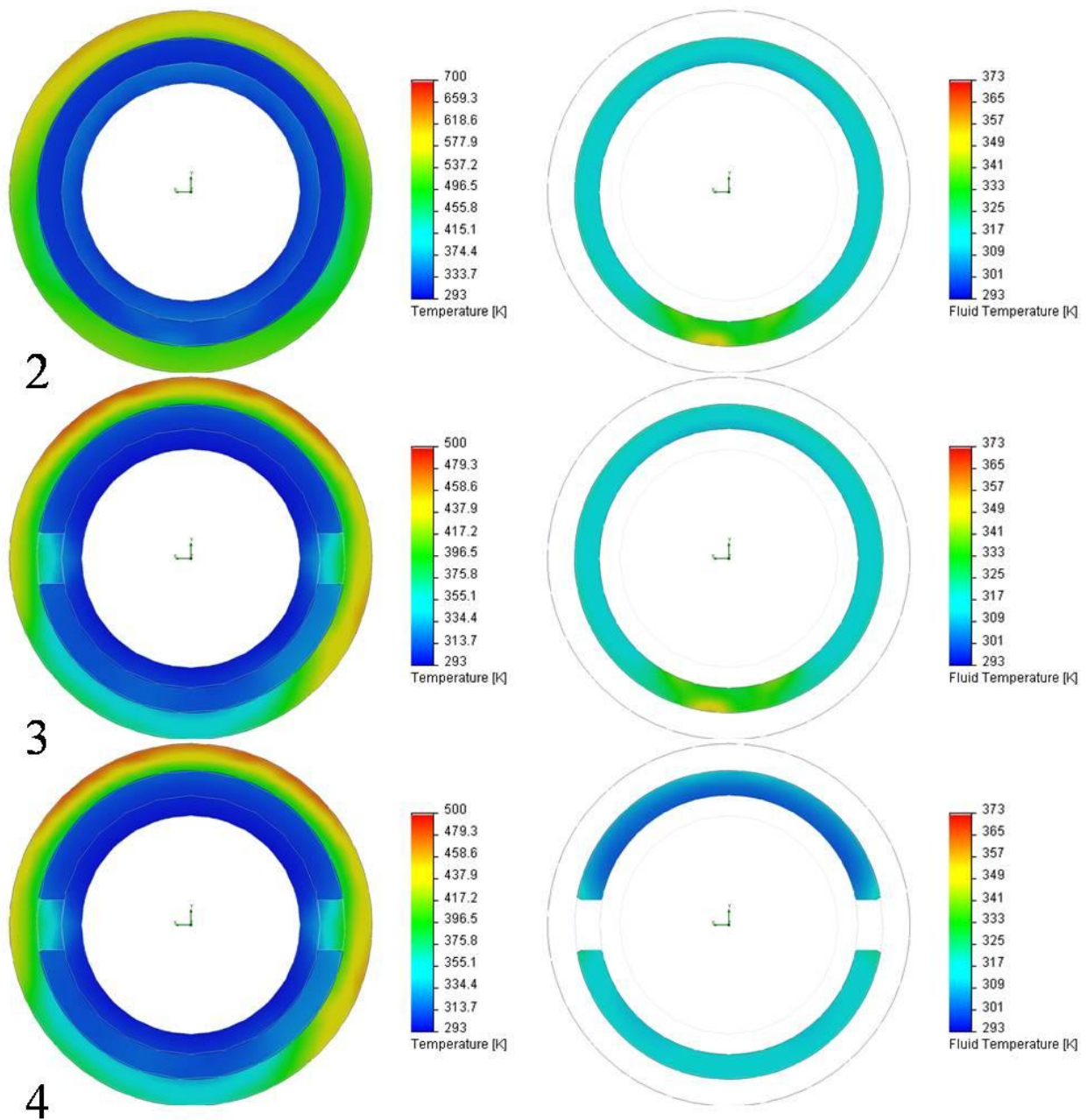


Figure 132. Temperature (left) and Fluid Temperature (right) distributions for probe insertion of 75% at Mach 0.7 with flat tip at Planes 2, 3, and 4.

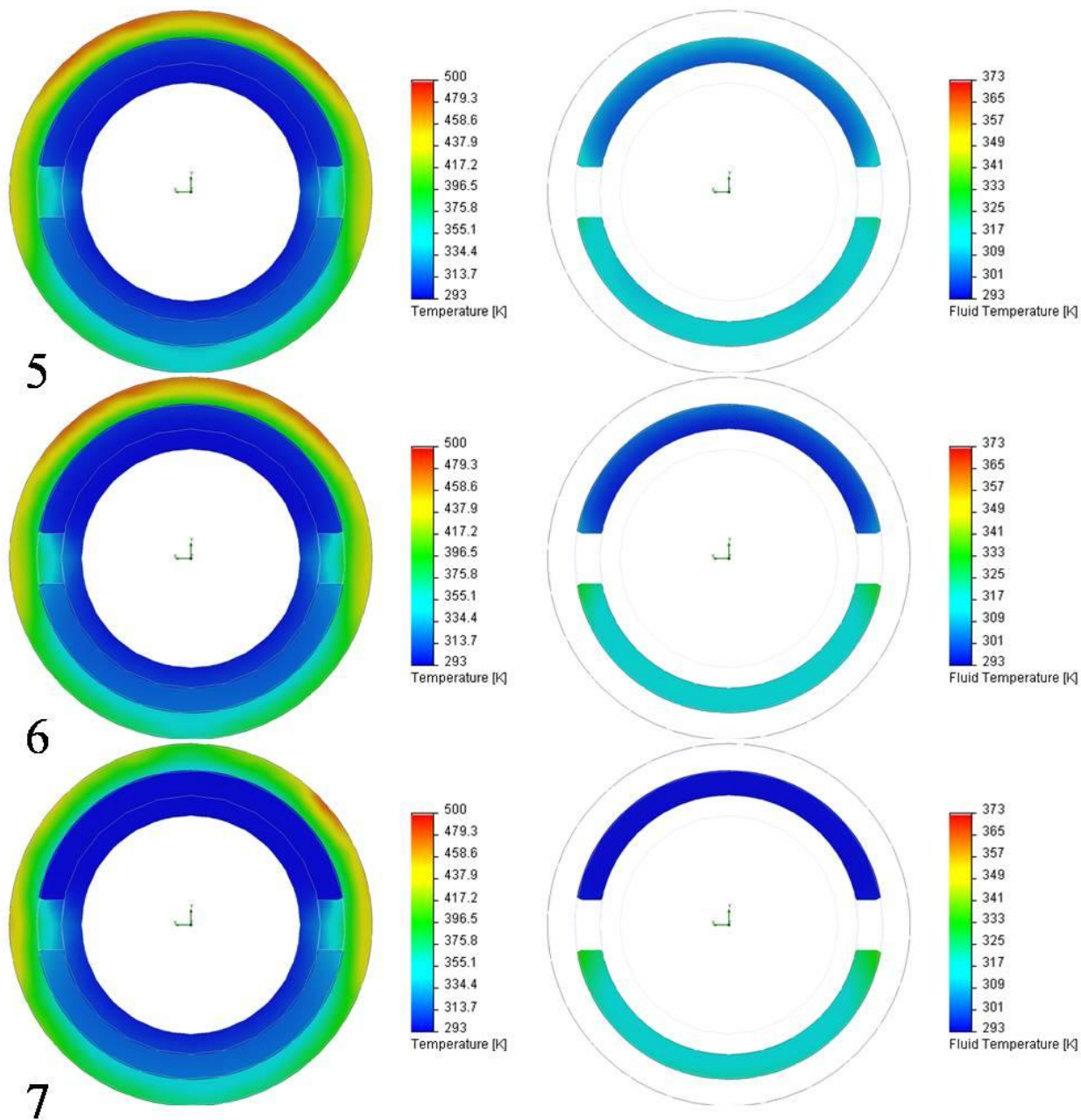


Figure 133. Temperature (left) and Fluid Temperature (right) distributions for probe insertion of 75% at Mach 0.7 with flat tip at Planes 5, 6, and 7.

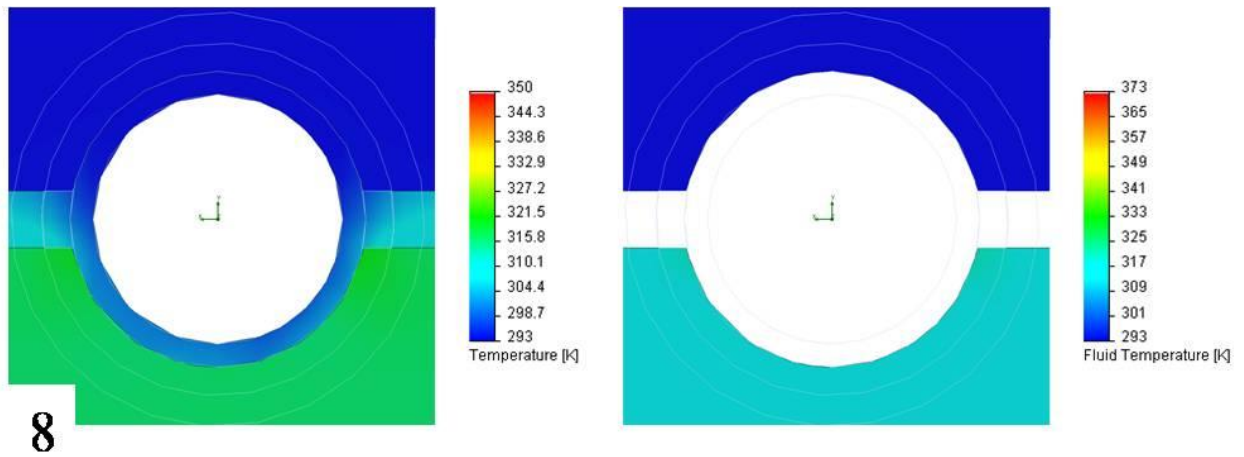


Figure 134. Temperature (left) and Fluid Temperature (right) distributions for probe insertion of 75% at Mach 0.7 with flat tip at Plane 8.

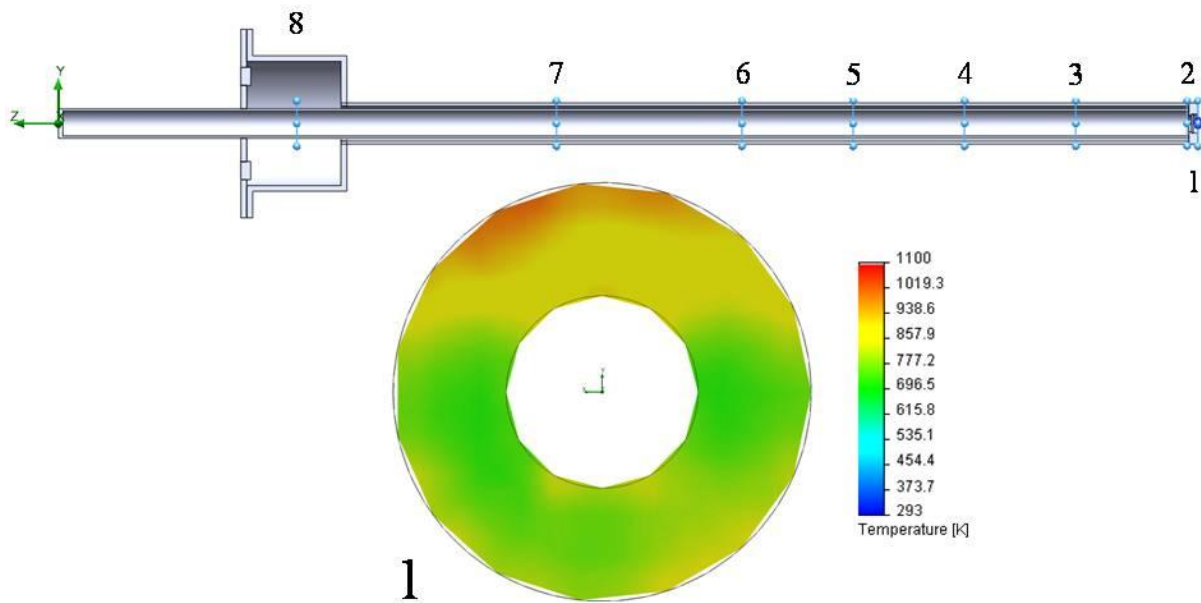


Figure 135. Plane locations along jacket length (top). Temperature distribution for probe insertion of 88.9% at Mach 0.7 with flat tip at Plane 1 (bottom).

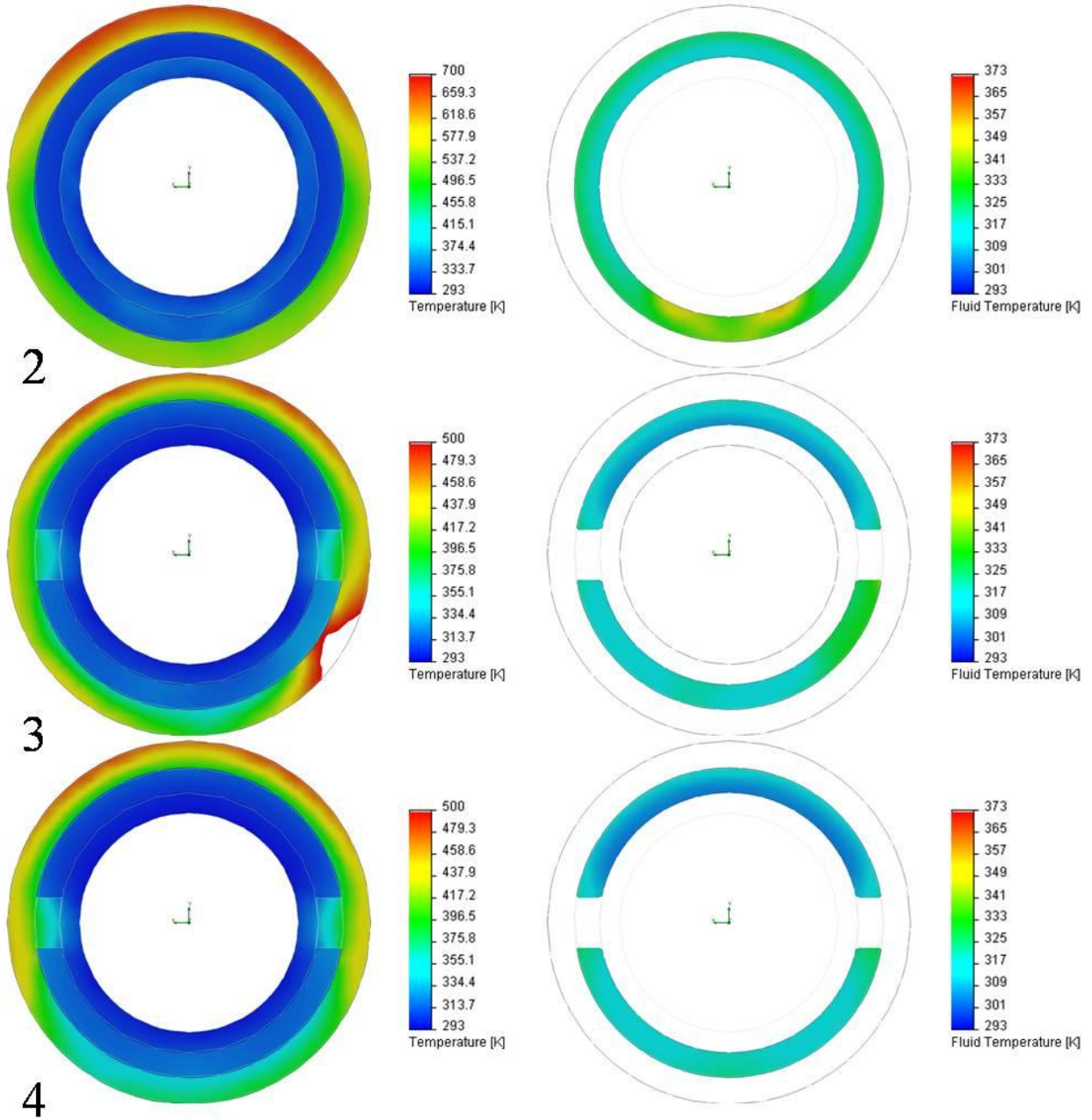
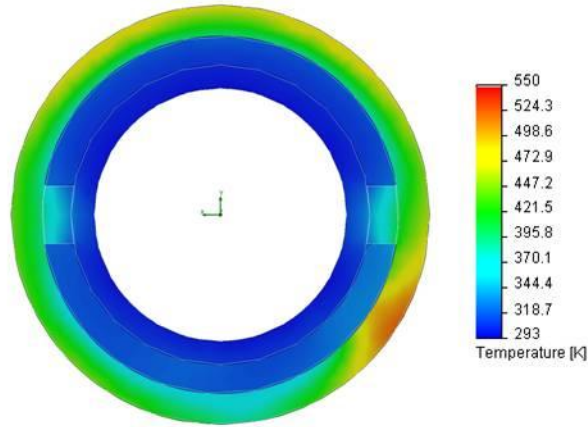


Figure 136. Temperature (left) and Fluid Temperature (right) distributions for probe insertion of 88.9% at Mach 0.7 with flat tip at Planes 2, 3, and 4.



3—Alternate Temperature Range

Figure 137. Temperature distribution for probe insertion of 88.9% at Mach 0.7 with flat tip at Planes 3 with alternate temperature scale range.

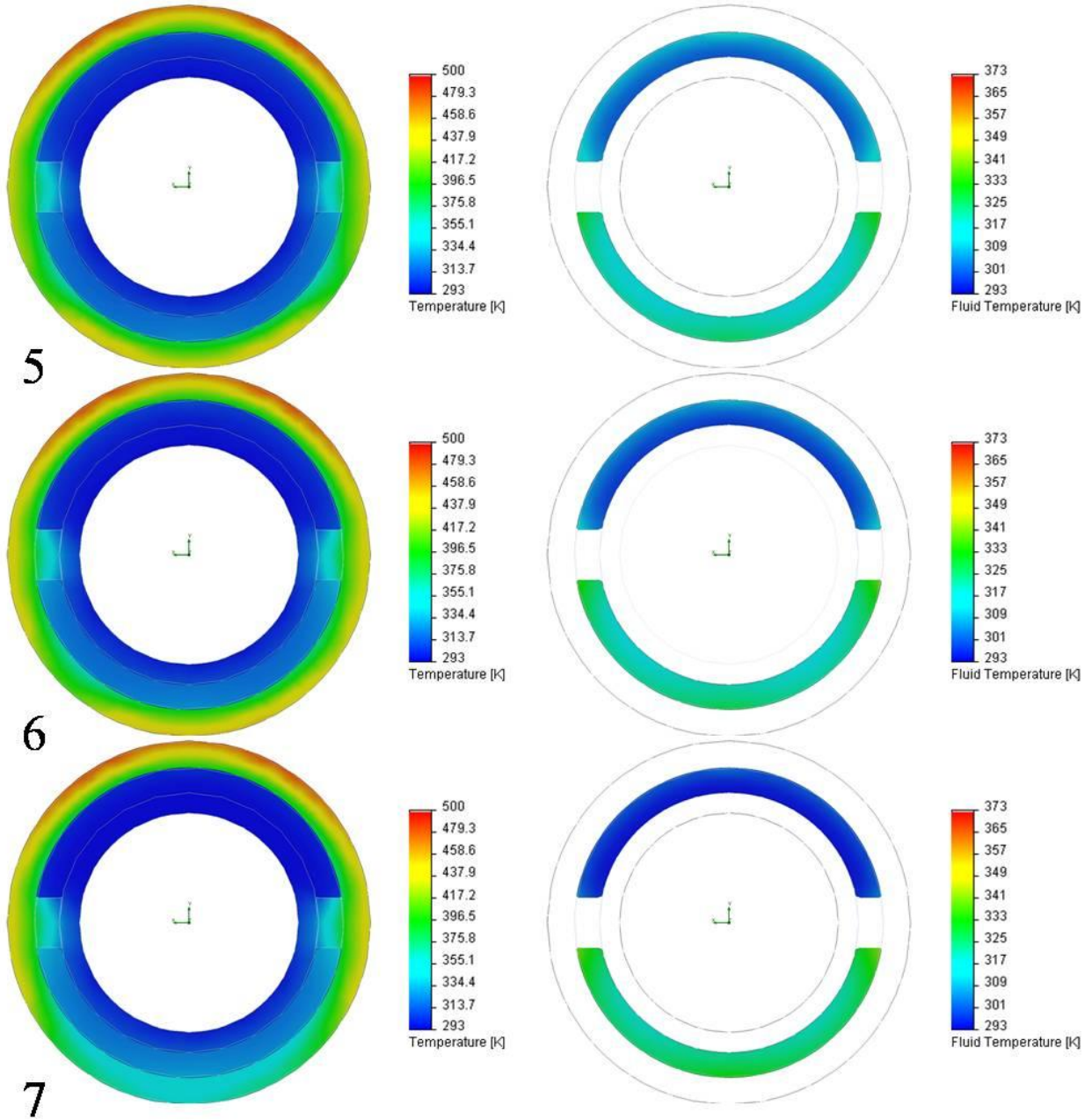


Figure 138. Temperature (left) and Fluid Temperature (right) distributions for probe insertion of 88.9% at Mach 0.7 with flat tip at Planes 5, 6, and 7.

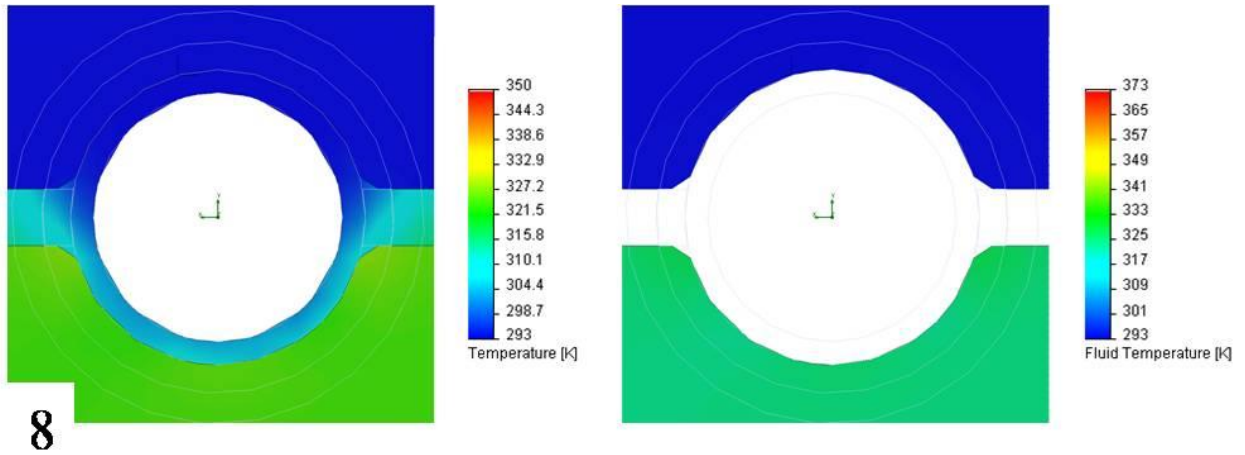


Figure 139. Temperature (left) and Fluid Temperature (right) distributions for probe insertion of 88.9% at Mach 0.7 with flat tip at Plane 8.